

**Titre:** Improvement of Barrier Properties of Poly(Ethylene  
Terephthalate)with Nanoclay

**Auteur:** Hesam Ghasemi

**Date:** 2010

**Type:** Mémoire ou thèse / Dissertation or Thesis

**Référence:** Ghasemi, H. (2010). Improvement of Barrier Properties of Poly(Ethylene  
Terephthalate)with Nanoclay [Thèse de doctorat, École Polytechnique de  
Montréal]. PolyPublie. <https://publications.polymtl.ca/451/>

 **Document en libre accès dans PolyPublie**  
Open Access document in PolyPublie

**URL de PolyPublie:** <https://publications.polymtl.ca/451/>

**Directeurs de  
recherche:** Pierre Carreau, & Musa R. Kamal

**Programme:** Génie chimique

UNIVERSITÉ DE MONTRÉAL

IMPROVEMENT OF BARRIER PROPERTIES OF  
POLY(ETHYLENE TEREPHTHALATE) WITH NANOCCLAY

HESAM GHASEMI  
DÉPARTMENT DE GÉNIE CHIMIQUE  
ÉCOLE POLYTECHNIQUE DE MONTRÉAL

THÈSE PRÉSENTÉE EN VUE DE L'OBTENTION  
DU DIPLÔME DE PHILOSOPHIAE DOCTOR (Ph.D.)  
(GÉNIE CHIMIQUE)  
DÉCEMBRE 2010

© Ghasemi Hesam, 2010.

UNIVERSITÉ DE MONTRÉAL

ÉCOLE POLYTECHNIQUE DE MONTRÉAL

Cette thèse intitulée:

IMPROVEMENT OF BARRIER PROPERTIES OF  
POLY(ETHYLENE TEREPHTHALATE) WITH NANOCCLAY

présentée par: GHA SEMI Hesam

en vue de l'obtention de diplôme de: Philosophiae Doctor

a été dûment acceptée par le jury d'examen constitué de:

Mme HEUZEY Marie-Claude, Ph.D., présidente

M. CARREAU Pierre, Ph.D., membre et directeur de recherche

M. KAMAL Musa, Ph.D., membre et codirecteur de recherche

M. AJJI Abdellah, Ph.D., membre

M. RODRIGUE Denis, Ph.D., membre

## **ACKNOWLEDGEMENTS**

I would like to offer my sincere and humble gratitude to my supervisors, Prof. Pierre Carreau and Prof. Musa Kamal. It was a great privilege to work with these wise and understanding gentlemen and I do not forget their support and the trust they placed in me in this project.

A special word of thanks is owed to Dr. Tabatabaei, Dr. Calderon, Ms. Leelapornpisit, Ms. Hamdine and last but not least, Dr. Chapleau, for their help during this study.

I also thank the technical and administrative staff of the chemical engineering department.

## RÉSUMÉ

Le polyéthylène téréphtalate (PET) comme polymère d'ingénierie semi-cristallin trouve énormément d'applications dans l'industrie des emballages. Cependant, pour certaines applications comme celles des boissons gazeuses et des bières, diminuer sa perméabilité au gaz, autrement dit augmenter ses propriétés barrières, demeure un défi considérable. L'introduction de feuillets de nano-argile de silicate en tant que phase imperméable dans la matrice polymère devient ainsi une alternative intéressante. Le mélange à l'état fondu et la polymérisation *in situ* sont des techniques généralement utilisées pour produire des nano-composites de PET. La première méthode reste cependant préférable car elle présente des avantages économiques et environnementaux, puisqu'elle ne nécessite pas la présence de solvants ni de monomères.

Dans la première phase de la présente étude, les nano-composites de PET (NCPs) ont été préparés en utilisant différentes argiles organiquement modifiées. La compatibilité avec la matrice, ainsi que la stabilité thermique de l'ensemble, jouent un rôle prépondérant dans l'évolution morphologique des NCPs.

Dans la deuxième phase, des films minces de NCP ont été produits avec succès par extrusion suivi d'un étirage. L'effet de l'incorporation des argiles sur les propriétés mécaniques, barrières, thermiques et optiques des produits finaux a été étudié. Aussi, l'importance de la cristallinité lors de la solidification en sortie d'extrusion et l'influence de la présence des argiles sur le degré de cristallinité en conditions isothermes comme non-isothermes ont été investiguées.

## ABSTRACT

Polyethylene terephthalate (PET), as a semi crystalline engineering polymer, is used extensively in packaging applications. However, gas permeability is a challenge in some applications such as soft drinks and beers. The introduction of layered silicate nanoclay, as an impermeable nanoparticle phase in a polymer matrix, is an attractive approach to enhance gas barrier properties. Melt compounding and in situ polymerization are the main techniques employed to produce PET nanocomposites. The former is the preferred method for preparation of polymer nanocomposites, which has environmental and cost advantages, due to the absence of solvents and monomers.

In the first phase of this work, PET clay nanocomposites (PCN) were prepared using different types of organo-modified clay, including ammonium, phosphonium and imidazolium surfactants. Both compatibility and thermal stability play an important role in morphological development of PCNs.

In the second and main part of this project, PCN thin films were prepared successfully, using cast film extrusion. The effect of incorporated clay on mechanical, barrier, thermal and optical properties of the products was studied. Incorporating 3 wt% Cloisite30B into PET matrix, led to 23% reduction in oxygen permeability and 20% improvement in tensile modulus. The effect of processing conditions, including screw profile, screw speed and feeding rate, on properties of PCN films were also studied. It was found that screw speed and, accordingly, applied shear has stronger effect on barrier and mechanical properties of the final products than feeding rate (residence time). At the highest screw speed, 27% and 30% improvement in barrier properties and tensile modulus were achieved, respectively.

The evolution of crystallinity during processing and the influence of clay on the

crystallization behavior have an important effect on the mechanical, optical and barrier properties of the nanocomposites. Thus, both non-isothermal and isothermal crystallization kinetics of PCN were investigated. It was found that, overall, isothermal crystallization of PET was faster in the PCNs than in the neat PET. However, the presence of clay leads to less perfect crystalline structures. The calculated effective crystallization activation energy for the PCNs was higher than for the PET, which suggests smaller crystalline structure for the PCNs during non-isothermal crystallization.

## CONDENSÉ EN FRANÇAIS

Des problèmes de stabilité thermique des nano-composites sont souvent rencontrés lorsqu'on procède à haute température au mélange du PET avec des nano-argiles organiques. Cette dégradation thermique touche autant le PET, les argiles organiquement modifiées que la compatibilité entre le PET et l'agent de modification chimique. En début de cette étude, différentes argiles modifiées par des agents de surface à base d'ammonium, de phosphonium et d'imidazolium ont été testées. Nous avons trouvé que l'argile commerciale à base d'ammonium, la Cloisite 30B (C30B) donnait le meilleur degré de séparation des feuillets d'argile et par conséquent la meilleure morphologie. En effet, la microscopie à balayage électronique (SEM) a révélé une bonne distribution des argiles et la microscopie électronique par transmission (TEM) a confirmé l'existence de tactoïdes ainsi que de feuillets individuels. Cependant, la C30B s'est avérée être la moins stable thermiquement des argiles modifiées testées. En effet, même si les deux groupements hydroxyles existant au sein de la C30B peuvent accroître la compatibilité entre les chaînes de PET et l'argile organique, ils sont néanmoins suspectés de causer la dégradation thermique de l'agent de surface à la température de mélange. Les amas de tactoïdes observés dans le cas de la C30B sont probablement le résultat d'un mélange insuffisant et/ou de l'affaissement brusque des feuillets de silicate dû à la dégradation thermique de l'agent de surface à la température de mélange. En revanche, la TGA a bien montré que la stabilité thermique dans le cas des argiles à base d'imidazolium et de pyridinium était meilleure que celle de la C30B; cependant leurs températures à 5 % de réduction massique ( $T_{5\%}$ ) sont proches de la température de procédé; les liens vinyles et C=C contribuent similairement à la dégradation de l'agent modifiant. Le manque de compatibilité entre les chaînes de PET et le surfactant à base d'imidazolium pourrait expliquer la présence des tactoïdes dans le système. Mise à part

l'amélioration de la stabilité thermique, le faible degré de dispersion des feuillets d'argile constitue une grande limite pour ce type d'argile en comparaison à la C30B.

Dans un souci d'amélioration de la stabilité thermique, quelques surfactants à base de phosphonium (P00408, P00308 and P00208) ont également été examinés. Ces composés ainsi que leurs argiles organiques correspondantes ont montré certes une amélioration de la résistance à la dégradation thermique à la température de mélange du PET, mais la compatibilité entre eux et le PET reste une limite critique. Ainsi, les nano-composites en résultant contenaient plus de tactoïdes et d'amas dans leurs structures. Plusieurs facteurs pourraient expliquer cela, entre autres la faible diffusivité du PET dans l'espace confiné entre les feuillets de silicate et possiblement le besoin d'utiliser un mélange plus intensif. Apparemment, le petit groupement alkyle et le groupement rigide phényle dans les P00308 et P00408 respectivement, produisent une compacité plus élevée de l'agent modifiant entre les feuillets de silicate. L'alignement, l'arrangement confiné et latéral de l'agent modifiant pourrait constituer un obstacle à la diffusion des chaînes polymères dans l'espace existant entre les feuillets de silicate. Les chaînes de PET ont du mal à pénétrer dans les galeries, dû à la saturation de l'espace par la présence des molécules du surfactant. En comparaison aux deux premiers surfactants à base de phosphonium, le P00208 a une longue queue aliphatique qui fournit plus de sites d'interaction avec le polymère, à la surface de l'argile. Les résultats statistiques montrent que le parcours libre  $D_{0,1}$ , des nano-composites avec le P00208 est 5.8%, ce qui représente 1% de moins que celui des nano-composites avec la C30B.

Pour produire des nano-composites par extrusion à l'état fondu, les agrégats d'argile et les tactoïdes doivent être réduits en dimension. Les chaînes de polymères doivent par la suite pénétrer dans l'espace des galeries. Un poids moléculaire élevé et de longues chaînes polymères contribuent à un cisaillement plus intense durant le mélange, tandis qu'un poids moléculaire bas

et de courtes chaînes polymériques facilitent leur pénétration dans les galeries de l'argile. La deuxième phase de cette étude a été donc consacrée à l'amélioration de la mise en œuvre des nano-composites. Pour ce faire, un grade expérimental de PET de haute viscosité et un autre de plus faible viscosité et d'usage général ont été mélangés selon le ratio 4:1 (faible : haute viscosité). Puisque parmi les autres argiles organiquement modifiées, la C30B a montré la meilleure morphologie, des films minces de PET contenant 3% massique de C30B ont été préparés par extrusion suivi d'un étirage-calandrage). Les études morphologiques incluant l'observation directe par TEM et la diffraction des rayons X à angle large en deux dimensions (2D-WAXD) ont révélé que les feuillets de silicate ont été orientés dans la direction de l'écoulement. L'augmentation du taux d'étirage ne semble pas avoir d'effet sur leur degré d'orientation.

Les résultats de DSC ont montré une basse température de cristallisation pour les films de nano-composites, indiquant ainsi que les argiles agissent comme des sites de nucléation durant la cristallisation. Ainsi la présence de plusieurs sites de nucléation conduit à une cristallisation plus rapide et à l'augmentation de la cristallinité induite durant l'extrusion d'un facteur de 2 en incorporant 3% massique de C30B par exemple. Le degré de cristallinité a également été augmenté d'un facteur de 4 lors du recuit des films à 150°C. La présence de l'argile et leur exfoliation incomplète réduisent, comme attendu, la clarté des films et augmentent leur opacité. Comme les valeurs mesurées de l'opacité et de la clarté pour les nano-composites étaient moins de 6% et plus de 85% respectivement, la transparence des films selon la norme ASTM D1003, peut être considérée comme acceptable.

Les valeurs de perméabilité à l'oxygène ont montré que le taux d'étirage n'a pas d'effet significatif sur les propriétés barrières des films produits. À la concentration de 3% massique de C30B, une réduction de perméabilité à l'oxygène de 23% a été obtenue. La perméabilité à

l'oxygène pour du PET pur et des films de nano-composites recuits décroît de 40 et 46% respectivement. Cela indique qu'en plus de la tortuosité, on devrait prendre en compte l'immobilité des segments de chaînes polymères due à un environnement confiné. Après recuit, les lamelles cristallines induisent plus de confinement et d'obstacles au sein de la matrice conduisant ainsi à une mobilité moindre des chaînes et à une perméabilité plus réduite. En d'autres termes, au même titre que l'effet des feuillets de silicate, la faible perméabilité de la phase cristalline comparée à la phase amorphe pourrait constituer une approche complémentaire pour réduire la perméabilité au gaz.

La C30B contient 30% de surfactant organique, ce qui veut dire que les nano-composites ayant une concentration massique nominale de 3% de C30B devraient contenir 2.1% massique en teneur en cendres. Hors la teneur en cendres réelle mesurée a été 1.8%; cette différence est probablement due à la perte d'une certaine quantité d'argile dans la trémie d'alimentation de l'extrudeuse. Cette teneur correspond à la fraction volumique de feuilles de silicate de  $\phi=0.009$  dans les nano-composites. En se basant sur la perméabilité seuil de percolation reportée et sur la valeur prédite par des modèles de normalisation, le rapport de forme ( $\alpha$ ) des feuilles de silicate est 150. Les prédictions des modèles de Nielson (analytique) et de Gusev (numérique) ont été proches de nos valeurs expérimentales. On doit mentionner ici que ces modèles assument que la structure est entièrement dispersée et orientée. Comme la morphologie des films nano-composites a bien montré une structure partiellement intercalée, la différence existant entre la prédiction de ces modèles et la perméabilité relative ( $K=0.77$ ) mesurée expérimentalement est acceptable. Concernant les valeurs prédites par ces modèles, on peut conclure que même dans le cas d'une exfoliation complète, la perméabilité devrait au mieux la moitié de la valeur du PET pur à ce niveau de charge d'argile ( $\phi=0.009$ ). Les micrographes de TEM ont été utilisés pour estimer le

rapport de forme moyen  $\alpha$ , qui n'est autre que le rapport entre la longueur ( $\ell$ ) et l'épaisseur ( $z$ ) des particules d'argile. L'histogramme d'analyse d'images basé sur ~200 ratios calculés a donné un rapport de forme moyen des particules de silicate de 47. En tenant compte de la perméabilité relative expérimentale ( $K=0.77$ ) dans le calcul par les modèles de Nielson (analytique) et de Gusev (numérique), on trouve que les rapports de forme sont 63 et 55 respectivement, ce qui est en cohérence avec la valeur donnée par l'analyse d'images.

En présence d'argile, la résistance à la déchirure décroît dans la direction de la machine (MD) et la direction transversale (TD). Quant à la propagation de la déchirure, elle est légèrement plus importante dans TD que dans MD, cela pourrait être dû à une orientation partielle des chaînes de PET dans la direction de l'écoulement. Par rapport aux films de PET pur, l'incorporation des argiles mène à une augmentation du module d'élasticité en traction et de leur fragilité. En effet, à 3% massique de C30B, le module d'élasticité de traction augmente d'environ 20%. Comme la morphologie des nano-composites indiquait la coexistence d'une structure intercalée et de tactoïdes dispersés, il s'avère qu'elle a un effet significatif sur le renforcement mécanique. Une pile de feuillets d'argile comprenant le surfactant organique ou les chaînes de polymère entre les couches d'argile peut être considérée comme une pseudo-particule ayant un plus faible rapport de forme effectif et une fraction volumique plus élevée.

Pour étudier l'effet des conditions de procédé sur les propriétés des produits finaux, deux géométries de vis avec des éléments de mélange différents tournant à différentes vitesses ( $N$ ) et différents taux d'alimentation ( $Q$ ) ont été utilisés pour préparer des films de nano-composites de PET/argile (PCN) contenant 3% massique de C30B. Les patrons de XRD ont indiqué que la distance intercalaire entre les feuillets d'argile était indépendante des conditions utilisées; par contre la caractérisation macroscopique incluant les propriétés barrières et mécaniques ont bien

montré que le niveau de délamination des feuillets a été affecté.

En se basant sur l'observation directe au TEM, on peut conclure qu'à haute vitesse de rotation de la vis (haute déformation) ou à faible taux d'alimentation (temps de séjour plus élevé), une morphologie partiellement exfoliée/intercalée peut être obtenue. Pour mettre en évidence l'effet de la géométrie de la vis sur le degré de dispersion des feuillets d'argile, la distance du parcours libre entre particules a été utilisée pour estimer le degré de dispersion dans des échantillons préparés à hautes vitesses de vis. Il semblerait que l'utilisation d'éléments de malaxage larges suivis d'éléments de mélange étroits donnerait une meilleure délamination. Il est bon de mentionner ici qu'à la plus haute vitesse de rotation de vis ( $N=250$  rpm) le couple mesuré pour la 2<sup>ème</sup> géométrie de vis était 10% plus important que pour la 1<sup>ère</sup>.

Les mesures de DSC ont montré qu'aux mêmes conditions de procédé, les films de PCN ont une température de cristallisation plus basse  $T_c$ , ( $\sim 9$  °C) que les films de PET pur. Quelque soit la géométrie de vis la  $T_c$  des échantillons préparés à la plus basse vitesse ( $N=150$  rpm) était un peu plus élevée que celle des échantillons préparés à plus haute vitesse ( $N=250$  rpm). La différence était cependant plus nette en utilisant une vitesse de vis constante et un taux d'alimentation le plus élevé; les échantillons ont en effet montré une réduction de  $T_c$  de 2-3 °C. On peut conclure, dans ce cas, que ces échantillons ont plus de sites de nucléation que les autres. Il est aussi probable que la dégradation du PET en présence de la C30B soit plus importante et la réduction du poids moléculaire contribue à la réduction de  $T_c$ . Ceci dit, une faible valeur de  $T_c$  pourrait être reliée à une meilleure délamination des feuillets d'argile ou à la dégradation de la matrice et, par conséquent, la présence de courtes chaînes de polymère due au temps de séjour long à faible taux d'alimentation. Ceci était également en concordance avec les propriétés mécaniques.

Les valeurs mesurées de la perméabilité à l'oxygène ont montré qu'elle était indépendante de

la géométrie de vis utilisée. À une certaine vitesse de rotation de vis et un certain taux d'alimentation de l'extrudeuse, les valeurs de  $K$  étaient assez proches. Cependant pour un même échantillon la vitesse de vis semble avoir un effet plus important que le taux d'alimentation de l'extrudeuse.

Par rapport aux films de PET pur, l'incorporation de l'argile mène à une augmentation du module d'élasticité en traction. Pour toutes les conditions de procédé, les films de PCN préparés avec le 2<sup>ème</sup> géométrie de vis ont montré une légère augmentation (3-4%) du module d'élasticité en traction, ceci pourrait être attribué à une meilleure distribution de l'argile dans la matrice comme discuté plus haut par l'observation directe par TEM et en se basant sur les valeurs de  $D_{0,1}$ . Pour une géométrie de vis, une augmentation plus importante du module a été obtenue à la vitesse maximale de vis : 26 et 30% pour les échantillons M4 et W4 respectivement. Malgré cette augmentation, il semblerait qu'au taux d'alimentation le plus faible (un temps de séjour plus long) provoquerait une dégradation plus importante de la matrice. Et pour un taux d'alimentation constant, le module d'élasticité en traction semble augmenter graduellement avec la vitesse de vis.

En se basant sur l'effet du traitement thermique (recuit) sur les propriétés barrières des films de PCN et l'effet de l'argile sur la cristallinité du polymère, la cinétique de cristallisation isotherme et non isotherme a été également étudiée. Afin d'évaluer les paramètres de cristallisation, nous nous sommes concentrés uniquement sur les échantillons contenant 1% massique se C30B. La théorie de Avrami montre que la cristallisation isotherme des nanocomposites prend place plus rapidement. Une analyse plus poussée utilisant le traitement de Lauritzen-Hoffman a révélé que la présence de l'argile mène à une structure cristalline moins parfaite. En d'autres termes, par rapport au PET pur, le point de fusion à l'équilibre des PCN apparaît à plus haute température et le travail nécessaire au repli des chaînes polymères en

présence de l'argile est légèrement plus élevée. La DSC modulée (MDSC) a été utilisée pour mettre plus de lumière sur les multiples endothermes de fusion observées lors du chauffage des échantillons cristallisés isothermiquement. Il apparaît que le troisième pic endotherme observé soit attribué à la recristallisation et à la fusion des cristaux organisés durant le chauffage, tandis que les premier et deuxième pics sont associés à la fusion des cristaux primaires et secondaires respectivement. L'équation modifiée d'Avrami et la méthode combinée de Avrami-Ozawa ont également été appliquées pour décrire le processus de cristallisation non isotherme. L'énergie barrière effective calculée pour les nano-composites était plus importante que le PET pur, ce qui indique une structure cristalline moins parfaite pour les nano-composites lors de la cristallisation non isotherme.

## TABLE OF CONTENT

ACKNOWLEDGEMENTS .....	iii
RÉSUMÉ.....	iv
ABSTRACT .....	v
CONDENSÉ EN FRANÇAIS .....	vii
TABLE OF CONTENT .....	xv
LIST OF TABLES .....	xix
LIST OF FIGURES.....	xxi
CHAPTER 1.....	1
INTRODUCTION.....	1
CHAPTER 2.....	3
LITERATURE REVIEW .....	3
2.1 Reduction of permeability in PET.....	3
2.2 Preparation of PET nanocomposites .....	9
2.3 Characterization of PCN as a final product.....	12
2.4 Effect of nanoclay on crystallization behavior of PCN.....	13
2.5 Objectives.....	15
CHAPTER 3.....	16
METHODOLOGY .....	16
3.1 Materials.....	16
3.1.1 PET.....	16
3.2.2. Organomodified Clays .....	17
3.2 Process.....	18

3.3. Characterization .....	21
3.3.1 Morphology .....	21
3.3.2 Thermal Properties .....	22
3.3.3 Optical Properties .....	24
3.3.4 Barrier Properties .....	25
3.3.5 Mechanical Properties .....	25
CHAPTER 4.....	27
ORGANIZATION OF ARTICLES .....	27
CHAPTER 5.....	30
Preparation and characterization of PET/Clay nanocomposites by melt compounding .....	30
5.1 Introduction .....	31
5.2 Experimental .....	33
5.2.1 Materials.....	33
5.2.2 Melt Compounding .....	34
5.2.3 Characterization .....	36
5.3 Results and discussion.....	37
5.3.1 Ammonium surfactant.....	37
5.3.2 Imidazolium surfactants .....	41
5.3.3 Phosponium surfactants.....	43
5.4 Conclusion.....	49
5.5 Acknowledgments.....	50
5.6 References .....	50
CHAPTER 6.....	53
Properties of PET nanocomposite films.....	53

6.1 Introduction .....	54
6.2 Experimental .....	55
6.2.1 Materials .....	55
6.2.2 Melt Compounding .....	56
6.2.3 Characterization .....	57
6.3 Results and discussion.....	59
6.3.1 Morphology .....	59
6.3.2 Crystallization Behavior.....	62
6.3.3 Optical Properties .....	65
6.3.4 Oxygen Permeability.....	66
6.3.5 Mechanical Properties .....	72
6.4 Conclusion.....	75
6.5 Acknowledgments .....	75
6.6 References .....	76
CHAPTER 7.....	79
Effect of processing conditions on properties of PET/clay nanocomposite films .....	79
7.1 Introduction .....	80
7.2 Experimental .....	82
7.2.1 Materials .....	82
7.2.2 Melt Compounding .....	82
7.2.3 Characterization .....	86
7.3 Results and discussion.....	87
7.3.1 Morphology .....	87
7.3.2 Crystallization Behavior.....	94

7.3.3 Oxygen Permeability .....	96
7.3.4 Mechanical Properties .....	98
7.4 Conclusion.....	100
7.5 Acknowledgments .....	101
7.6 References .....	102
CHAPTER 8.....	107
GENERAL DISCUSSION.....	107
CHAPTER 9.....	112
CONCLUSIONS AND RECOMMENDATIONS.....	112
9.1 Conclusions .....	112
9.2 Originality of the work.....	115
9.3 Recommendations .....	116
REFERENCES.....	118
Appendix A .....	130
Isothermal and Non-Isothermal crystallization behavior of PET nanocomposite .....	130

## LIST OF TABLES

### Chapter 3

Table 3.1: The characteristics of the organically-modified clays .....	17
--	----

### Chapter 5

Table 5.1: Characteristics of the neat polymer and organically-modified clays .....	34
---	----

Table 5.2: TGA and XRD results of PCNs .....	38
--	----

Table 5.3: Form factors of phosphonium-modified clays .....	44
---	----

Table 5.4: DSC results of PCNs with C30B and P00208 .....	49
---	----

### Chapter 6

Table 6.1: Predicted relative permeability values for different models. ( $\phi=0.009$ & $\alpha=150$ ).....	71
--	----

Table 6.2: Halpin-Tsai and Pseudoinclusion models .....	74
---	----

### Chapter 7

Table 7.1: Processing conditions and sample identifications.....	85
--	----

### Appendix A

Table A.1: Triple melting points of the PET and PCNs versus isothermal crystallization, $T$ , obtained by DSC. ....	137
--	-----

Table A.2: Total released heat and results of the Avrami analysis for isothermal crystallization of the PET and PCNs. All tests were done twice and the average values of $\Delta H$ are reported, here. ....	140
---	-----

Table A.3: The results of Malkin analysis for isothermal crystallization of the PET and PCNs.....	145
--	-----

Table A.4: Results of Lauritzen-Hoffman analysis for isothermal crystallization of PET and PCNs.....	146
---	-----

Table A.5: Characteristic data of non-isothermal crystallization of the PET and PCNs. All tests were done twice and the average values of $\Delta H$ are reported, here. ....	149
Table A.6: Results of the Avrami analysis for non-isothermal crystallization of the PET and PCNs.....	153
Table A.7: Results of the combined Avrami and Ozawa kinetic models for non-isothermal crystallization of the PET and PCNs.....	154
Table A.8: Crystallization rate coefficient, crystallization rate parameter and crystallization rate index for the PET and PCNs .....	156

## LIST OF FIGURES

### Chapter 2

- Figure 2.1: Schematic of barrier mechanism of PET/PEN blends: *a*) before and *b*) after biaxial deformation [11]..... 5
- Figure 2.2: Pictorial effect of silicate layers on permeation of small molecules ..... 9
- Figure 2.3: Common procedure for preparing PET nanocomposites by in situ polymerization: *a*) modification of clay and *b*) intercalation by polymerization..... 10

### Chapter 3

- Figure 3.1: Experimental strategy ..... 16
- Figure 3.2: Screw configuration: *a*) 1<sup>st</sup> mixing zone with 30, 60 and 90° elliptical elements; *b*) 2<sup>nd</sup> mixing zone with 30° elliptical elements; *c*) 3<sup>rd</sup> mixing zone with 60° elliptical elements..... 18
- Figure 3.3: Screw configuration: *a*) 1<sup>st</sup> mixing zone composed of both 45° right and left hand kneading blocks; *b*) 2<sup>nd</sup> mixing zone with 45° right hand kneading blocks; and *c*) 3<sup>rd</sup> mixing zone including 45° and 90° kneading blocks. KB and LH denote kneading block and left hand, respectively. The first two numbers indicate the staggering angle and number of blocks, respectively and the third one represents the length in mm..... 19
- Figure 3.4: First screw profile: *a*) 1<sup>st</sup> mixing zone composed of 10 kneading elements with both positive (right hand) and negative (left hand) 60° staggering angle; *b*) 2<sup>nd</sup> mixing zone with two left and right hand ZME elements; and *c*) 3<sup>rd</sup> mixing zone including kneading elements with positive 60° staggering angle. .... 20
- Figure 3.5: Second screw profile: *a*) 1<sup>st</sup> mixing zone composed of three wide kneading

elements with  $90^\circ$  staggering angle followed by two narrow kneading blocks with  $30^\circ$  and  $60^\circ$  staggering angle; b) 2<sup>nd</sup> mixing zone with three kneading elements ( $0^\circ$ ) followed by 8 kneading elements with both positive (right hand) and negative (left hand)  $60^\circ$  staggering angle; and c) 3<sup>rd</sup> mixing zone including three wide kneading elements with  $90^\circ$  followed by 10 kneading elements with  $30^\circ$  and  $60^\circ$  staggering angle..... 21

## Chapter 5

Figure 5.1: Chemical structure of the surfactants. The negatively charged counter-ions are chlorine or bromine .....	35
Figure 5.2: Screw configuration: a) 1 <sup>st</sup> mixing zone with $30^\circ$ , $60^\circ$ and $90^\circ$ elliptical elements; b) 2 <sup>nd</sup> mixing zone with $30^\circ$ elliptical elements; c) 3 <sup>rd</sup> mixing zone with $60^\circ$ elliptical elements.....	36
Figure 5.3: SEM images of the PCN with 2 wt% C30B.....	38
Figure 5.4: TEM images of the PCN with 2 wt% C30B (All scale bars represent 50 nm).....	39
Figure 5.5: Various intercalation mechanisms for the PNC containing 2 wt% C30B. The main micrograph shows the break-up and inset depicts peeling.....	40
Figure 5.6: Layer spacing histogram of: a) the PCN with 2 wt% C30B; and b) the PCN with 2 wt% P00208 .....	41
Figure 5.7: Morphology of the PCN containing 1.25 wt% 2C16-Im a) SEM; and b) TEM (All scale bars in TEM micrographs represent 50 nm).....	42
Figure 5.8: SEM images of the PCN containing 2 wt% P00408 .....	43
Figure 5.9: SEM images of the PCN containing 2 wt% P00308 .....	44
Figure 5.11: SEM images of the PCN containing 2 wt% P00208 .....	45
Figure 5.11: TEM images of the PCN with 2 wt% P00208.....	46

Figure 5.12: DSC results of the PCNs with C30B prepared by TSE, at 10°C/min *a*) Cooling cycle (2nd cycle); and *b*) Relative crystallinity vs. time ..... 48

## Chapter 6

Figure 6.1: Complex viscosity of the neat polymers measured with a CSM rheometer at a stress amplitude of 200 Pa and 280 °C..... 56

Figure 6.2: Screw configuration: a) 1<sup>st</sup> mixing zone composed of both 45° right and left hand kneading blocks; b) 2<sup>nd</sup> mixing zone with 45° right hand kneading blocks; and c) 3<sup>rd</sup> mixing zone including 45° and 90° kneading blocks. KB and LH denote kneading block and left hand, respectively. The first two numbers indicate the staggering angle and number of blocks, respectively and the third one represents the length in mm..... 57

Figure 6.3: TEM micrographs of PCN films containing 3% C30B at the largest draw ratio (65) MD and ND denote machine and normal direction, respectively. The scale bars represent a) 0.2 μm; b) 100 nm; and c) 20 nm. .... 60

Figure 6.4: 2-D WAXD patterns of PCN films containing 1% C30B at the largest draw ratio (65) in: a) MN; and b) MT plane The insert depicts the observed planes. .... 60

Figure 6.5: a) Azimuthal intensity profile; and b) Diffraction spectrum of PCN films with 1% C30B at the largest draw ratio (65) in MN plane..... 61

Figure 6.6: Azimuthal intensity profiles of PCN films containing 1% C30B at a) the smallest (25); and b) largest (65) draw ratios in MN plane ..... 62

Figure 6.7: DSC results of PCN films with C30B. a) DSC traces during cold crystallization; b) DSC of annealed films; c) melting points of annealed samples vs. clay content; d) crystallinity before and after annealing..... 63

Figure 6.8: 2-D WAXD patterns of PCN films with 3% C30B at the largest draw ratio (65).

a) before; and b) after annealing.....	64
Figure 6.9: Diffraction spectrum of PCN films after annealing: a) neat PET; and b) PCN with 3% C30B .....	65
Figure 6.10: Haze and clarity of PCN films with C30B at the largest draw ratio (65).....	66
Figure 6.11: a) Oxygen permeability of PCN films vs. draw ratio; and b) Effect of crystallization on barrier properties of PCN films with C30B at the largest draw ratio (65).....	68
Figure 6.12: Measuring the aspect ratio of the silicate layers by image analysis. Silicate layers are laid in MD.....	70
Figure 6.13: Histogram of calculated aspect ratio for PCN films with 3% C30B .....	72
Figure 6.14: Tear resistance of PCN films in the machine (MD) and transverse (TD) directions at the largest draw ratio (65).....	73
Figure 6.15: Tensile modulus in MD and puncture resistance of PCN films at the largest draw ratio (65).....	73

## Chapter 7

Figure 7.1: Complex viscosity of the neat polymers measured with a CSM rheometer at a stress amplitude of 200 Pa and 280 °C.....	82
Figure 7.2: First screw profile: a) 1 <sup>st</sup> mixing zone composed of 10 kneading elements with both positive (right hand) and negative (left hand) 60° staggering angle; b) 2 <sup>nd</sup> mixing zone with two left and right hand ZME elements; and c) 3 <sup>rd</sup> mixing zone including kneading elements with positive 60° staggering angle. ....	83
Figure 7.3: Second screw profile: a) 1 <sup>st</sup> mixing zone composed of three wide kneading elements with 90° staggering angle followed by two narrow kneading blocks with 30° and 60° staggering angle; b) 2 <sup>nd</sup> mixing zone with three kneading	

elements ( $0^\circ$ ) followed by 8 kneading elements with both positive (right hand) and negative (left hand)  $60^\circ$  staggering angle; and c) 3<sup>rd</sup> mixing zone including three wide kneading elements with  $90^\circ$  followed by 10 kneading elements with  $30^\circ$  and  $60^\circ$  staggering angle..... 84

Figure 7.4: WAXD spectra of: a) PCN films prepared using the first screw profile (M series); b) PCN films prepared using the second screw configuration (W series); c): samples M2 and M4 (constant feeding rate, first screw profile); d) samples W2 and W4 (constant feeding rate, second screw profile); e) samples M5 and M6 (constant screw speed, first screw profile); and f) samples W5 and W6 (constant screw speed, second screw profile) ..... 88

Figure 7.5: Top) Typical 2-D WAXD patterns of PCN films in a) MN; and b) MT plane; Bottom) Diffraction spectrum of PCN films prepared using the first screw profile at c) constant feeding rate; and d) constant screw speed. MD, TD and ND in the insert, represent machine, transverse and normal directions, respectively. Accordingly, the MT plane is defined by the MD and TD axes and the MN plane is specified by the MD and ND axes. .... 89

Figure 7.6: TEM micrographs of sample W4 (second screw profile, the highest screw speed) for two magnifications (top and bottom) and two different positions (left and right). .... 90

Figure 7.7: TEM micrographs of sample W5 (second screw profile, the lowest feeding rate) for two magnifications (top and bottom) and two different positions (left and right). .... 91

Figure 7.8: TEM micrographs of sample W6 (second screw profile, the highest feeding rate) for two magnifications (top and bottom) and two different positions (left

and right). .....	92
Figure 7.9: TEM micrographs of sample M4 (first screw profile, the highest screw speed) for two magnifications (top and bottom) and two different positions (left and right). .....	93
Figure 7.10: DSC results of PCN films produced using the first screw profile: a) Neat resin and PCN films prepared at $N=200$ rpm and $Q = 3$ kg/g; b) PCN films prepared at constant feeding rate ( $Q = 3$ kg/h). M2 and M4 are the samples prepared at 150 and 250 rpm, respectively. c) PCN films prepared at constant screw speed ( $N=200$ rpm). M5 and M6 are the samples prepared at 1.5 and 4 kg/h, respectively. The reported temperatures are the average of two experiments with the error range of $\pm 0.2$ °C. ....	95
Figure 7.11: Oxygen permeability of PCN films prepared by: a) first screw profile; and b) second screw configuration. The $K$ values ( $K=P/P_0$ ) represent the relative permeability of the samples. ( $P$ and $P_0$ are the permeabilities of the sample with and without clay, respectively.).....	97
Figure 7.12: Tensile modulus of PCN films in machine direction, prepared using: a) the first screw profile; and b) the second screw configuration. ....	99
Figure 7.13: a) W1 after elongation at 200 %; b) W4 after elongation at break; and c) load vs. tensile strain for both W1 and W4. Both samples were 68 $\mu\text{m}$ thick. ....	100
<b>Appendix A</b>	
Figure A.1: DSC melting endotherms of isothermally crystallized PET and PCNs at two given temperatures (190 and 210 °C). Samples were heated immediately after isothermal crystallization for duration of 15 min. Open and close symbols are related to the PET and PCNs, respectively. ....	135

Figure A.2: MDSC melting thermograph of the PET after isothermal crystallization at 200°C.....	136
Figure A.3: Application of the Hoffman-Weeks approach to the PET and PCNs. Open and close symbols are related to the PET and PCNs, respectively. ....	138
Figure A.4: DSC exotherms of isothermal crystallization at various temperatures of (a) PET; and (b) PCNs and relative crystallinity vs. time during isothermal crystallization at various temperatures of (c) PET; and (d) PCNs .....	139
Figure A.5: POM micrographs for isothermal crystallization at 210 °C. Time evolution of crystal growth in left) PET and right) PCN.....	141
Figure A.6: Comparison between the Avrami and Malkin model predictions with the experimental data at 200 °C. Open and close symbols are related to the PET and PCNs, respectively. ....	145
Figure A.7: a & b) DSC exotherms of non-isothermal crystallization of the PET and PCNs at various cooling rates. c & d) Relative crystallinity of the PET and PCNs versus temperatures, at various cooling rates. e & f) Relative crystallinity of the PET and PCNs a fun function of time, at various cooling rates.....	150
Figure A.8: POM micrographs for non-isothermal crystallization. Time evolution of crystal growth: top) PET at cooling rate 30 °C/min middle) PCNs at cooling rate 30 °C/min bottom) PET at cooling rate 5 °C/min .....	151
Figure A.9: Ozawa analysis for non-isothermal crystallization of the a) PET; and b) PCNs.....	154
Figure A.10: Dependence of the effective energy barrier on the degree of crystallinity for the PET and PCNs. Open and close symbols are related to the PET and PCNs, respectively.....	156

# CHAPTER 1

## INTRODUCTION

Poly(ethylene terephthalate) (PET), a semi crystalline engineering polymer, exhibits many properties that are desirable for barrier applications. These properties include polarity, high chain stiffness, and close chain packing via symmetry, intermolecular bonding, high glass transition temperature and crystallinity. However, gas permeability to CO<sub>2</sub> and oxygen has been a challenge in some applications, such as soft drink and beer packaging. Dispersing layered silicate clay as an impermeable nanoparticle phase in a polymer matrix is an attractive approach to enhance gas barrier properties. The impermeable silicate layers create a tortuous path within the polymer matrix. As a result, gas molecules diffuse through the material with more difficulty. Moreover, because gas barrier properties are improved at low concentrations of layered silicate this approach should be inexpensive and efficient.

Two techniques are widely used for preparation of PET/clay nanocomposites (PCN): melt compounding and in situ polymerization. Melt compounding is the preferred method for preparation of polymer nanocomposites, which have environmental and cost advantages, due to the absence of solvents and monomers. Furthermore, the high deformation rates employed in melt extrusion compounding are useful for dispersion of nanoparticles in the molten polymer matrix.

The main objective of this project is to produce polymer/clay nanocomposites by melt compounding to improve the barrier properties of extruded PET films. To achieve this goal, different type of surfactants were incorporated into the PET matrix. Morphological studies show

that PCNs incorporating Cloisite30B (C30B) exhibit better dispersion and intercalation than phosphonium and imidazolium modified clays. On the other hand, the thermal stability of phosphonium modified clays is significantly higher than of C30B systems. After selecting the proper modified clay, PCN films were prepared via cast extrusion at the Industrial Materials Institute (IMI), and the mechanical, optical and barrier properties of the products were studied.

Chapter 2 provides a literature review covering the following subjects: the methods used to improve barrier properties of PET, the studies on preparation of PET nanocomposites, reports regarding characterization of nanocomposites as final products and the effect of clay particles on the crystallization behavior of PET. The materials used and the methodology chosen to achieve the objectives are presented in Chapter 3. Chapter 4 briefly explains the organization of the papers reported in the thesis. In Chapter 5, the effect of compatibility and thermal stability of surfactants on the morphology of PCNs was investigated using X-ray diffraction (XRD), scanning electron microscopy (SEM), transmission electron microscopy (TEM) and thermogravimetric analysis (TGA). The morphological, mechanical, thermal, optical and barrier properties of PCN films prepared by cast extrusion are discussed in Chapter 6. The study reported in Chapter 7 deals with the effects of processing conditions, including screw speed, feeding rate and screw configuration on properties of PCN films. Chapter 8, general discussion, includes a full review regarding the most important factors affecting the preparation and properties of PCNs. Finally, Chapter 9 summarizes the most important conclusions of this thesis and outlines some recommendations for future work in this area. In view of the important effect of crystallinity on the final properties of PCNs, Appendix A summarizes the results of a study carried out to evaluate the isothermal and non-isothermal crystallization kinetics of PCN.

## CHAPTER 2

### LITERATURE REVIEW

#### 2.1 Reduction of permeability in PET

Several techniques were suggested to improve barrier properties of PET, including surface modification, crystallization and orientation, blending and incorporation of nanoparticles as an impermeable phase.

Various coating techniques, such as plasma enhanced chemical vapor deposition (PECVD) and reactive evaporation can be used for surface modification of polymer substances. Employing plasma source ion implantation, amorphous carbon layers were deposited on PET films and oxygen transmission rate (OTR) decreased dramatically [1]. Surface modification of PET with an organic solution of silane and dip coating of the modified PET film in a lithium metasilicate solution led to more than 90% reduction in OTR [2]. While OTR of the coated PET decreases substantially, gas barrier loss of coated PET under uniaxial stretching was also reported [3], which is due to the brittle nature of the coated films. However, higher microwave power input and oxygen flow rate during the PECVD coating technique led to better barrier properties, but barrier properties only remained nearly unchanged, up to a critical strain of 1% [4]. Cracks appeared on the surface of a strained coated film, perpendicular to the strain direction, resulting in increase gas permeability. In fact, surface modification methods are expensive and not appropriate for food packaging. Furthermore, crack formation at the surface during stretching of the coated products causes barrier properties to deteriorate.

A commonly used alternative approach involves increasing the tortuosity of the diffusion

path by geometrical hindrance. Crystallization per se, is considered a practical method to affect the permeability of PET matrix. Around 35% reduction of oxygen permeability was reported when annealing temperature varied in the range of 100-240°C [5]. In the annealing process, crystal thickness increases, crystal defects are removed, and the boundary between the amorphous and crystalline regions sharpens. As a consequence, permeability decreases. It was discussed that crystallization improves the barrier properties due to two factors [6-7]. On the one hand, crystallites act as impermeable phase and lower the portion of amorphous phase, through which the permeant diffuses. This factor affects the solubility of gas or liquid molecules in the matrix. On the other hand, crystallites increase the tortuosity of the diffusion path and act as geometrical hindrance. This factor affects the diffusion coefficient of the permeant. While crystallinity improves the barrier properties of PET, talc at similar volume content decreases permeability twice as much as crystallinity and yields better mechanical properties [6]. Although annealing raises crystal thickness and removes crystal defects, which consequently lower the gas permeation, it has some disadvantages. For instance, it reduces the transparency and causes brittleness of the product.

Orientation of polymeric chains may also affect the gas permeability of PET by causing reduction in both diffusion and solubility coefficients [7]. Comparison between barrier properties of amorphous and biaxially oriented PET showed that in oriented samples, solubility coefficient in a mixture composed of oxygen, nitrogen and carbon dioxide decreased around 50% [8].

Other methods employ reduction of solubility and diffusion coefficients of the permeant by blending and/or orientation to reduce oxygen permeability. Thus, a PET/thermotropic liquid crystalline blend shows more than 50% gas permeability reduction [9]. While alignment of liquid crystalline molecules led to low permeability, the binary blend showed poor mechanical properties due to lack of adhesion and compatibility. Upon biaxial orientation of PET/aromatic

polyamide or polyester blends, the dispersed domains are altered to form parallel and extended layers (Figure 2.1), thus causing improvement in barrier properties [10-11]. Notwithstanding the positive effects of biaxial orientation on barrier properties, the need for compatibilization and the possibility of transesterification present critical issues.

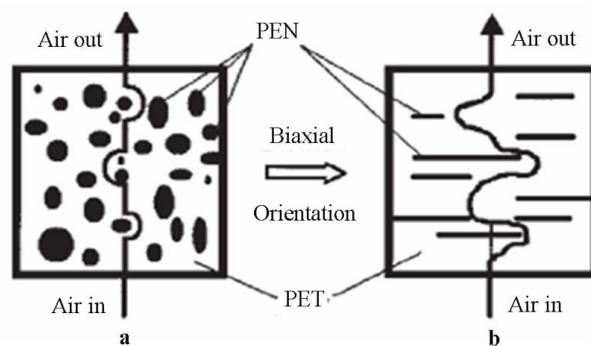


Figure 2.1: Schematic of barrier mechanism of PET/PEN blends: *a*) before and *b*) after biaxial deformation [11]

Inclusion of nanoparticles is a practical method to improve barrier properties of polymeric materials [12-28]. Adding a smectite organoclay in an olefinic system, including paraffinic wax and polyethylene, showed a 30% reduction in oxygen transmission rate (OTR) when organoclay content increased up to 10 wt%. However, high loading of clay led to embrittlement of the film. An increment in molecular weight of the wax, led to a decrease in barrier performance of the nanocomposites, because it is accompanied by an increase in the recrystallization temperature and as a result, phase separation of organoclay took place during cooling of the polymer melt. This indicated that the melting points of the organoclay and polymer phase must be close to each other, to avoid phase separation of the organoclay and polymer [12]. Gas barrier properties of a blend of PP/EPDM (50/50) nanocomposite were improved about two-fold, by adding 1.5 vol% organoclay. The PP/EPDM blend without organoclay showed a two-phase morphology, with EPDM as a dispersed phase in irregularly-shaped domains. The EPDM domains became smaller

in the presence of nanoclay [13]. In a study on the effect of compatibilizer on gas barrier properties of metallocene polyethylene nanocomposites a low density oxidized wax used as compatibilizer, yielding to a better dispersion level of the organomodified clay, in comparison with PE-g-MA. Accordingly, oxygen permeability of the former nanocomposite, containing 20 wt% low density oxidized wax and 5 wt% organomodified clay, was 10% lower than the latter nanocomposite, at the same level of PE-g-MA and clay [14]. Using PP-g-MA as a compatibilizer resulted in a better distribution and smaller cluster size of fumed silica in isotactic polypropylene. A 25% improvement on oxygen permeability was obtained by adding 5 wt% nanoparticles [15].

A study on barrier properties of acrylonitrile-butadiene copolymer nanocomposites, prepared by a Banbury internal mixer, showed that adding natural montmorillonite (MMT) was less effective in reducing gas permeation than organomodified clay, due to the absence of interaction between the rubber and natural clay. A 20 and 40% reduction in air permeability was obtained for MMT and organomodified nanocomposites, respectively (at 1.5 vol%) [16]. Since the compatibility between a matrix and nanoclay dictates the morphology and properties of the nanocomposite, using natural clay does not necessarily lead to a lower performance of the nanocomposite. Based on a study on biodegradable thermoplastic starch (TPS)/clay nanocomposites, the dispersion of the clay in the TPS matrix depended on the hydrophilicity of the clay and especially on the polar interaction between the silicate layers and TPS. Thus, MMT showed a better dispersion in the TPS matrix and lower water vapor permeability than organomodified clay [17].

An investigation on polyesteramide nanocomposites prepared via melt compounding displayed that, due to the high shear rates applied in the injection molding process, barrier properties of injection molded materials were better than extruded and extruded/compression molded materials [18]. Improvement of barrier properties in extruded and extruded/compression

molded samples was modest. Because of void content, paths for diffusion through the film and clay layers were not uniformly distributed in the samples. Barrier properties of injection molded samples were better, because of higher crystallinity, lower void content and greater degree of clay layer orientation [19].

A solution blending method used to prepare acrylonitrile butadiene rubber (NBR) nanocomposites. The mechanical and thermal properties of NBR were enhanced by incorporating less than ten parts per hundred (phr) of organosilicates. In addition, the relative vapor permeabilities of the NBR nanocomposites for water and methanol vapors were 85% and 42% lower, respectively, than that of pure NBR [20]. Melt intercalation of NBR nanocomposite with organoclay and silane, as a coupling agent, in an internal mixer led to a 70% reduction in vapor permeability by loading 10 phr of organo-MMT. The coupling agent enhanced the clay dispersion and the inter-chain attraction, leading to lower permeability for water vapor [21].

Not only the content of clay, but also the state of dispersion of the inorganic platelets in the polymer phase is important for improving the barrier properties of the PCNs. Gorrasi et al. [22] prepared different composites of polycaprolactone (PCL) and MMT, including microcomposites of PCL with Na-MMT by melt blending, exfoliated nanocomposites by in situ ring opening polymerization of  $\epsilon$ -caprolactone with organoclay, intercalated nanocomposites by melt blending of PCL and organoclay, and intercalated nanocomposites by in situ polymerization of  $\epsilon$ -caprolactone with Na-MMT. Barrier properties of these composites were measured for water vapor and dichloromethane as an organic solvent. The microcomposites and intercalated nanocomposites had diffusion parameters close to that of PCL. However, exfoliated nanocomposites showed much lower values. In another study, PCL/MMT nanocomposite at 3 wt% clay content were prepared in three ways: melt blending of MMT or organoclay with PCL, in situ polymerization of  $\epsilon$ -caprolactone with organoclay, and initiation of  $\epsilon$ -caprolactone

polymerization from the silicate layer with organoclay and activator. In the last method, polymer chains were grafted to the silicate layers. The gas permeability and the diffusion coefficient decreased for the intercalated nanocomposite compared to the microcomposite. The highest barrier properties were obtained with an exfoliated structure and the highest grafting density [23]. Using organoclay to prepare biodegradable PCL nanocomposites led to more than 30% improvement in the barrier performance of PCL nanocomposites (at 10 wt% clay content) [24].

A decrease in oxygen permeability for organoclay content below 8 wt% was reported for polyvinyl alcohol copolymer (EVOH) and kaolinite nanocomposites prepared by melt compounding in an internal mixer. The authors claimed that the oxygen permeability of the prepared nanocomposites were below experimental error of the instrument [25]. By loading 3-5 wt % organomodified clay, the moisture permeability coefficient of styrene-acrylate copolymer nanocomposites decreased 1.6 times [26-27]. PET nanocomposites prepared by in situ polymerization showed more than 30% reduction in oxygen permeability at 3 wt% clay content [28].

Apparently, exfoliation of nanoclay in molten polymers is somehow idealistic. Even though PA6 nanocomposite is a well-known commercial exfoliated product, a recent study reports only a 30% reduction of gas permeability at 8 wt% clay loading [29].

Obviously, dispersion of layered silicate clay as an impermeable phase in a polymer matrix leads to an enhancement in gas barrier properties. The impermeable silicate layers create a tortuous path in the polymer matrix, and, as a consequence, gas molecules diffuse with more difficulty (Figure 2.2). In general, it has been shown that a low content of nanoclay can improve barrier properties. The magnitude of basal spacing of the clay layers in the nanocomposite is influenced by processing conditions, and in the majority of studies, mixed intercalated/exfoliated morphology has been obtained via melt compounding. However, a maximum barrier performance

is expected for aligned exfoliated structures of nanocomposites.

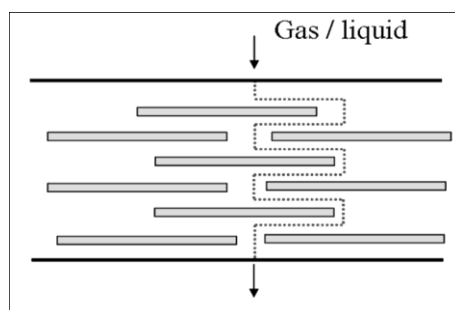


Figure 2.2: Pictorial effect of silicate layers on permeation of small molecules

As mentioned, among the methods applied to improve barrier properties of PET, incorporation of clay particles represents a pragmatic approach to lower gas permeation through the matrix. However, sometimes the effect of clay on barrier properties is exaggerated and unrealistic values have been reported. For example, it was claimed that adding only 1 wt% clay into PET led to more than 90% reduction in gas permeation [30-31], whereas based on the simplest model in the literature [32], the maximum reduction corresponding to this clay content is ca. 25%.

## 2.2 Preparation of PET nanocomposites

In situ polymerization and melt compounding are used widely to prepare PET clay nanocomposites (PCN). Despite reported works on using solution techniques to prepare PCN [33-35], this method is not as common as the above two processes. PET nanocomposites prepared by mixing PET and organomodified clay in a 3:1 (wt/wt) phenol/chloroform solvent showed a high level of dispersion without agglomeration at low organoclay content (below 5 wt%). [33-34]. Mixing PET and MMT in a 50/50 phenol/tetrachloroethane solvent with the assistance of ultrasonic power led to an intercalated/exfoliated morphology at 1 wt% MMT [35].

The conventional method for synthesis of PET comprises pre-polymerization, polycondensation, and solid state polymerization [36]. Pre-polymerization can take place with direct esterification between monomers, ethylene glycol and terephthalic acid, at 240-260°C or transesterification of dimethyl terephthalate at 170-210°C. In the polycondensation step, pre-polymerized BHET, Bis(2-hydroxyethyl) terephthalate, undergoes further transesterification at 280°C. Finally, the PET chips can be held at temperatures below the melting points. Owing to increasing segmental motions in solid state polymerization, functional groups at the end of the chains can react with each other, and molecular weight and chain length increase. The common procedures to modify clay and prepare PET nanocomposites by the direct polymerization method are shown in Figure 2.3.

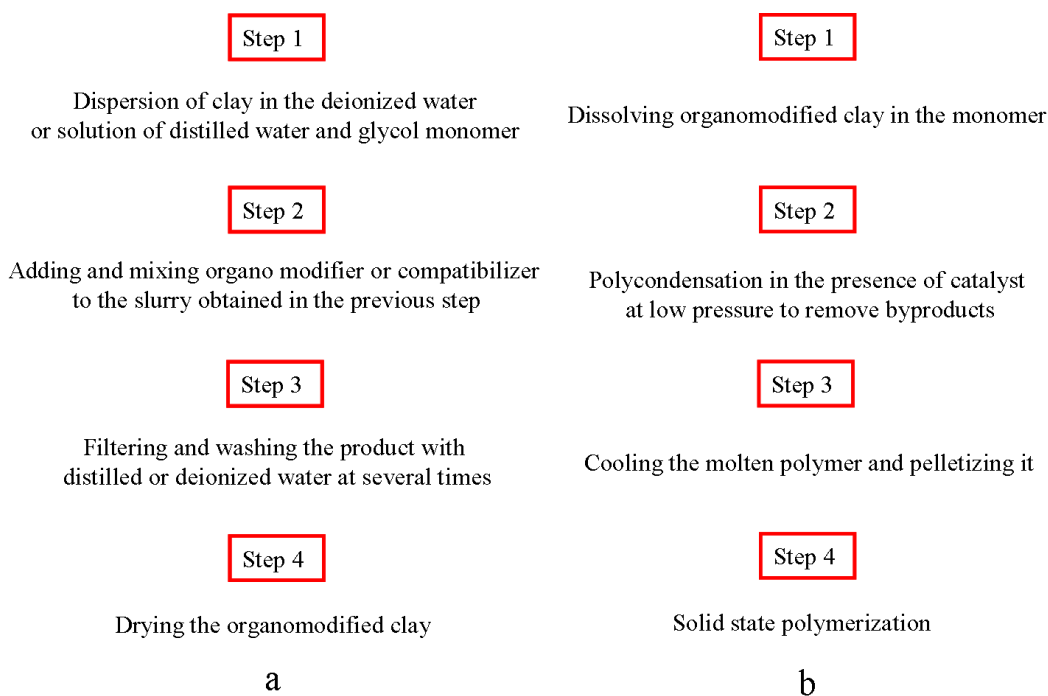


Figure 2.3: Common procedure for preparing PET nanocomposites by in situ polymerization: *a*) modification of clay and *b*) intercalation by polymerization

In situ polymerization leads to partially intercalated/exfoliated morphology, whether the

dispersing phase is a nanoparticle as  $\text{SiO}_2/\text{TiO}_2$  [37-44], expandable fluorine mica [45-47], nanoclay as montmorillonite [48-51] or natural fibrous silicate clay [52-53]. To improve the quality of dispersion and achieve more delamination of clay layers, different methods including ring opening polymerization [54], using anchor monomers [55] and intercalation of catalyst between the gallery spacing [30] were also studied.

Using solvents, remnant monomers and removal of by-product are the typical disadvantages of in situ polymerization, from an industrial point of view. Therefore, melt compounding is the preferred method for preparation of PCNs. Despite the attempts on using twin-roller [56] or solid state shear milling [57], torque Haake rheometer [58-61] and twin-screw extruder [62-67] are used vastly to prepare PCNs. The high deformation rates employed in melt extrusion compounding brings about dispersion of nanoparticles in the molten polymer matrix. However, various issues arise in the processing of PET at high temperature to produce PCNs. These include the compatibility between PET and the organic modifier, thermal stability of the organically modified clay and the thermal stability of PET.

Maleic anhydride and pentaerythritol have been used as coupling agents to improve the dispersion of clay particles in PET [68-70]. However, while Young's modulus increased with the incorporation of the nanoclay, the effect of coupling agent on the mechanical properties was negligible [70]. An alternative approach consists of PET chain modification to enhance interactions between the matrix and clay. The random incorporation of sulfonate functionalities along the polymer backbone led to electrostatic interactions between the sulfonate groups and platelets of clay and facilitated chain segment penetration of the clay galleries [71]. Few attempts considered the effect of clay structure on the dispersion level by substitution of layered double hydroxide (LDH) called anionic clay for conventional cationic clays [68, 72]. Further investigation showed that both interlamellar population density and interlayer packing density are

important to obtain nanocomposites. While the organophilicity of the clay increased with interlayer density of surfactant, it was not adequate to assure the formation of nanocomposites. A very high organic content could make the galleries so packed that the polymer chains would not be able to enter between them. In other words, the surface of the clays with lower organic content could leave more sites exposed to interact with the polymer chains entering into the galleries [73]. On the other hand, if the entropic gain due to exudation of organic modifier under processing condition exceeds the interaction energy between modifier and clay layers, organic modifiers would exit from the clay interlayer and gallery distance would decrease [61].

At the high processing temperatures required for melt compounding of PCN, the degradation of conventional organic modifiers presents a major problem. Modification of the clay surface with imidazolium [62], quinolinium [74], zirconium phosphorous [75] and phosphonium [76] surfactants yielded higher degradation temperature for partially intercalated nanocomposites. Thermal stability of organic modifier plays an important role in PCN preparation. To exclude the organic component, PET and organoclay were dissolved in an organic solvent followed by elimination of the extra modifier in a non-solvent [77]. This method led to better optical and thermal properties and less mechanical degradation of PCNs. The dependence of degradation level on the clay structure and surfactant chemistry revealed that hydroxyl groups on the edge of clay platelets acted as Brønsted acidic sites to accelerate polymer degradation [78]. Moreover, volatile degradation compounds were detected before the onset of thermal decomposition measured by TGA [79], emphasizing the effect of thermal stability on preparation of PCNs.

### **2.3 Characterization of PCN as a final product**

Few reports are available in the literature regarding the characterization of PET clay

nanocomposites (PCNs) as final products.

The ultimate tensile strength of PCN fibers with incorporated phosphonium modified clay increased with clay content [80]. The modulus of the prepared fibers by a capillary rheometer increased by about ca. 2 folds that of neat PET fibers. Another study on the effects of nanoclay on modulus and tenacity of PET fibers showed that the addition of nanoclay led to an increase of drawability in hot air [81]. Both Young's modulus and tenacity improved at 1 wt% loading of clay, but at higher concentration, the presence of large aggregates prohibited the efficient orientation along the fiber axis.

The effect of biaxial stretching on the dispersion level and tactoid concentration of PCN sheets was studied recently [82]. A type of synthetic clay (Somasif MAE) was incorporated into PET matrix (2 wt%) using a twin-screw extruder. The PCN sheets were biaxially stretched at a ratio of 3. TEM images displayed that the platelets slid along the tactoids, leading to ca. 20% reduction of oxygen permeability [82]. Another study showed that food-contact-complying modified clay, Nanoter<sup>TM</sup> 2000, was incorporated with PET in an internal batch mixer and oxygen permeability reduction ca. 30% was reported at 5 wt% clay [83]. Compounding a bottle grade PET with ammonium modified clay (Cloisite 15A) led to an increase of the tensile modulus by 20% for partially intercalated PCNs [84]. However ca. 20% oxygen permeability reduction was reported, but the permeability specimens were prepared by compression molding.

## **2.4 Effect of nanoclay on crystallization behavior of PCN**

The intensive study carried out on crystallization behavior of PET, has shown that isothermal crystallization of PET proceeds in two steps [85-87]. The primary stage includes the heterogeneous nucleation and three-dimensional spherical growth and the secondary step occurs

when one-dimensional growth between the primary lamellae takes place, whereas the former has stronger temperature dependence than the latter. It was also found that transesterification between lamellar crystals promote the formation of extended chain crystals [87] and long-chain hyperbranched structure also increases the crystallization rate [88]. Both shear and extension rate in melt and solid state influence the crystallization behavior of PET [89-90]. A constant shear rate applied to the molten PET brings about the orientation of molecular chains. As a result, homogenous molten PET changes to a suspension of dispersed crystallites in the amorphous matrix which leads to an increase in both storage modulus and shear viscosity with the time. [89]. Applying tensile strain on injected molded PET specimens (above  $T_g$ ) shows that amorphous regions subjected to strain extension act as oriented nuclei and consequently crystallization growth takes place under constant strain [90].

Generally speaking, the half time of crystallization,  $t_{1/2}$ , which is a characteristic of the reciprocal overall rate of crystallization, decreases by adding nanoparticles into PET matrix [91-96] and it is usually attributed to the role of nanoparticles as nucleating agents. Recently, the investigation on the effect of surfactant on crystallization of PET revealed that regardless of crystallization rate increment, the surface shielding effect of organic surfactant can also affect the crystallization rate [97-98].

In summary, thermal stability of organomodified clay and its compatibility with PET matrix are major challenges in preparation of PET nanocomposites (PCNs) by melt compounding and most of the efforts have been dedicated to the preparation and morphological studies of PCNs. Therefore, only a few reports are available on the characterization of PCNs as final products. Furthermore, the effect of processing conditions on macro-scale characterization of PCNs products yet remains unexplored. In view of the reported effects of clay on crystallization behavior of PCNs, there is still a relative lack of research into isothermal and non-isothermal

crystallization kinetic parameters of PCNs.

## **2.5 Objectives**

The main objective of this work was to improve barrier properties of PET by using melt compounding to prepare PET clay nanocomposites. To meet this goal, different types of organomodified clay were used and their level of dispersion was examined. Then, PET nanocomposite films were prepared via cast extrusion. Optical, thermal, barrier and mechanical properties of the final product were studied. The effect of processing conditions on barrier and mechanical properties of PET nanocomposite films were studied, as well. A secondary objective was to shed more light on the effect of incorporated clay on the crystallization kinetics of PCNs.

## CHAPTER 3

### METHODOLOGY

To meet the objective of this thesis, the experiments were divided in two steps. The first phase of the project involves initial material preparation, including production and characterization of PET nanocomposites and the second part includes final processing, comprising film extrusion and characterization (Figure 3.1).

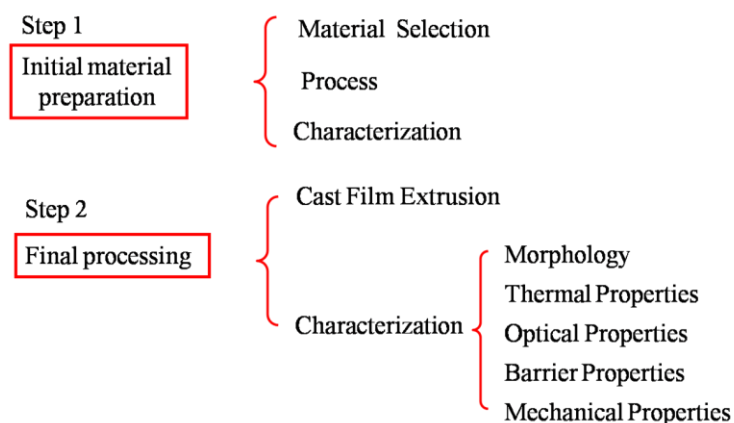


Figure 3.1: Experimental strategy

## 3.1 Materials

### 3.1.1 PET

In this study, two grades of PET including an experimental high viscosity grade and a low viscosity general purpose grade have been used. The former PET under the trade name Selar PTX295 was generously supplied by DuPont Canada and the latter PET referred to by the trade name, PET9921 was purchased from Eastman Chemical Co. The melting point of high viscosity, PTX, and low viscosity, PET9921, PET were 248 and 242°C, respectively.

### 3.2.2. Organomodified Clays

In the first phase of the project, three different types of organomodified clay were used: commercial ammonium-modified silicate clay, specially prepared thermally stable phosphonium and imidazolium-modified montmorillonite (MMT). The ammonium-modified clay under the trade name Cloisite30B was purchased from Southern Clay Co. The other clays were prepared by modification of MMT with phosphonium [99], imidazolium pyridinium surfactants [100] in laboratory. Chemical structures, 5 wt% mass reduction related temperature,  $T_{5\%}$ , and basal spacing,  $d_{001}$ , of the surfactants are summarized in Table 3.1.

Table 3.1: The characteristics of the organically-modified clays

Code	Modifier	$T_{5\%}$ (°C)	$d$ -spacing (Å)
C30B	quaternary <i>ammonium</i>	233	18.4
P00208	tributyl tetradecyl <i>phosphonium</i>	320	21.3
P00308	tetrabutyl <i>phosphonium</i>	365	16.2
P00408	4-carboxybutyl triphenyl <i>phosphonium</i>	313	18.5
C16-Im	1-vinyl hexadecyl <i>imidazolium</i>	287	17.8
2C16-Im	dihexadecyl <i>imidazolium</i>	271	22.0
C16-Py	hexadecyl <i>pyridinium</i>	288	17.6

As seen, phosphonium, imidazolium and pyridinium-modified clays exhibit higher thermal stability, as indicated  $T_{5\%}$  in TGA experiments, than Cloisite30B (C30B).

After characterizing the prepared PCNs in the first step, C30B and P00208 were selected for the second part of the experiments to produce PCN films.

### 3.2 Process

In the first step, preliminary tests were done in a batch internal mixer Brabender at 50rpm, temperature range 260-290 °C and residence time 5-10 min. After finding the processing parameters, melt compounding was carried out in a co-rotating twin screw extruder (TSE) (Leistritz ZSE 18 HP) available in the chemical engineering department of Ecole Polytechnique (Figure 3.2). The TSE screw diameter was 18 mm and the length/diameter ( $L/D$ ) ratio was 40. A circular die of 2 mm diameter was mounted on the barrel exit, and a water-ice bath was employed to cool the extrudate.

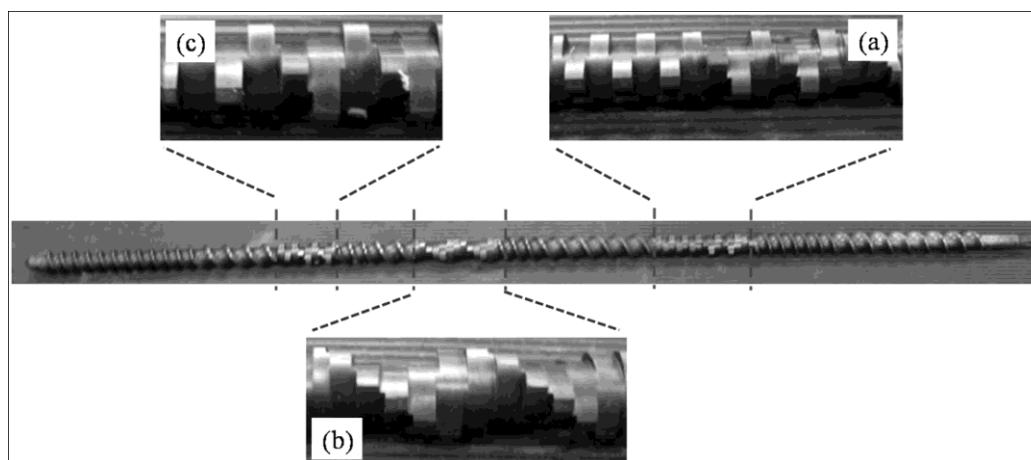


Figure 3.2: Screw configuration: a) 1<sup>st</sup> mixing zone with 30, 60 and 90° elliptical elements; b) 2<sup>nd</sup> mixing zone with 30° elliptical elements; c) 3<sup>rd</sup> mixing zone with 60° elliptical elements

In order to obtain a uniform feeding mixture, PET pellets were ground into a powder and dry-mixed with clay before feeding into the TSE hopper. PCNs were prepared at 175 rpm and temperature profile of 240, 275, 270, 265, 265, 265, 265 and 260 °C. Organoclay content was 2 wt% (nominal value) for the cases of C30B and phosphonium-modified MMT. In the imidazolium and pyridinium-modified MMT cases, the organoclay content was 1.25 wt% (nominal value). The nanocomposites extrudates were granulated and compression molded at

270°C for 9 min, under a purge of nitrogen, to obtain 25 mm disks. The obtained samples were used for X-Ray and morphological analysis. Since PET is sensitive to moisture, which has strong influence on its processing and performance properties, PET pellets and PET pelletized extrudates were dried in a vacuum oven at 110°C for 24 h before mixing and molding. C30B and the other modified clays were also dried at 50 and 110°C under vacuum, respectively.

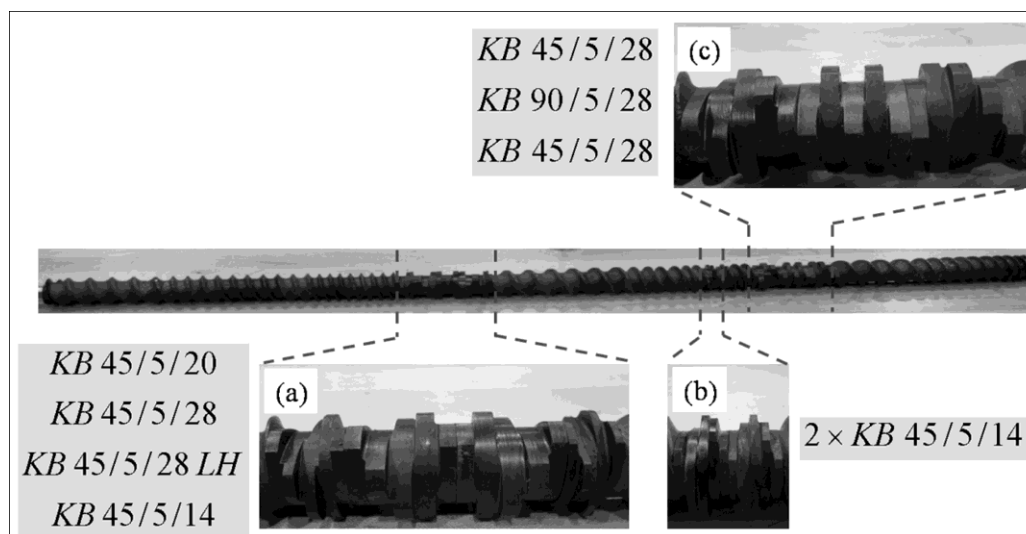


Figure 3.3: Screw configuration: a) 1<sup>st</sup> mixing zone composed of both 45° right and left hand kneading blocks; b) 2<sup>nd</sup> mixing zone with 45° right hand kneading blocks; and c) 3<sup>rd</sup> mixing zone including 45° and 90° kneading blocks. KB and LH denote kneading block and left hand, respectively. The first two numbers indicate the staggering angle and number of blocks, respectively and the third one represents the length in mm.

In the second part of project which involves producing PCN films, melt compounding was carried out in a co-rotating twin screw extruder (TSE) (Werner & Pfleiderer ZSK-30) available at IMI (Industrial Material Institute, Boucherville-QC) (Figure 3.3). The TSE had 30 mm screw diameter and  $L/D$  of 40. A slit die 1.9 mm thick and 20 cm wide was used to prepare films and an air knife was mounted on both sides of the die to supply air on the surface of the film, at a rate of

6.3 m/s, right at the exit of the die. The chill rolls were employed to stretch the extrudate. Draw ratios of 25, 40, 50 and 65 were applied. The extrusion was conducted at 265 °C and 175 rpm.

To study the effect of processing conditions on barrier and mechanical properties of PCN films, melt compounding was carried out in an intermeshing co-rotating twin screw extruder (TSE) (Leistritz, Germany), available at IMI. The clay was premixed with the grounded PET and then fed to the extruder hopper. The TSE has a 34 mm screw diameter and  $L/D$  of 42. Two different screw profiles were used to prepare PCN films (Figures 3.4 and 3.5).

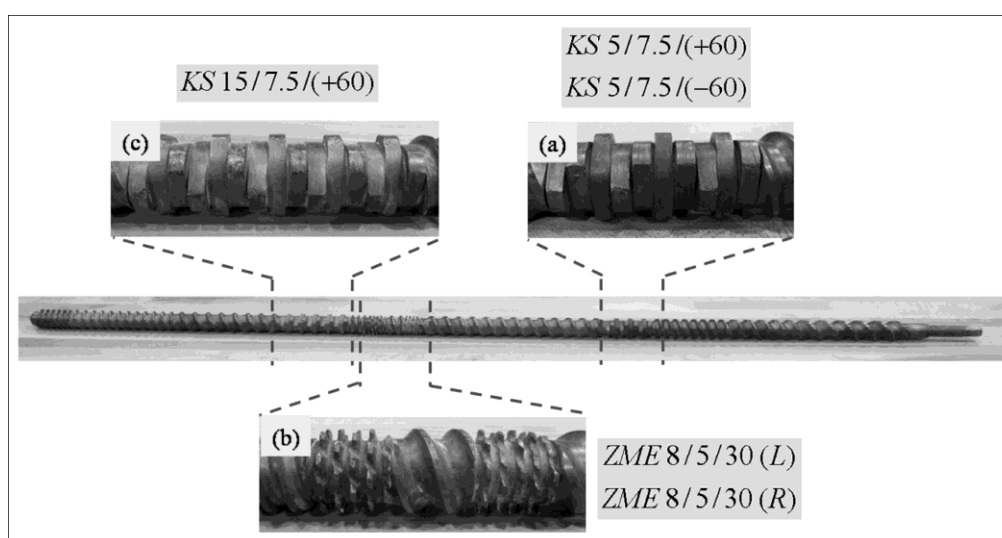


Figure 3.4: First screw profile: a) 1<sup>st</sup> mixing zone composed of 10 kneading elements with both positive (right hand) and negative (left hand) 60° staggering angle; b) 2<sup>nd</sup> mixing zone with two left and right hand ZME elements; and c) 3<sup>rd</sup> mixing zone including kneading elements with positive 60° staggering angle.

A 20 cm wide slit die with the die gap of 300  $\mu\text{m}$  was used to prepare films, and an air knife was mounted on both sides of the die to supply air on the surface of the film. A medium air flow rate (40% of maximum flow rate), corresponding to an air velocity of 5.2 m/s was chosen. The chill rolls (20 °C) were employed to stretch the extrudate and the distance between the die and chill

roles was ca. 10 cm. Under these conditions, the average necking was ca. 21%, which means the width of films was 16 cm and the thickness of the films was in the range of 60-80  $\mu\text{m}$ . The extrusion was conducted at different screw speeds ( $N$ ) and feeding rates ( $Q$ ) in the range of 150-250 rpm and 1.5-4 kg/h, respectively.

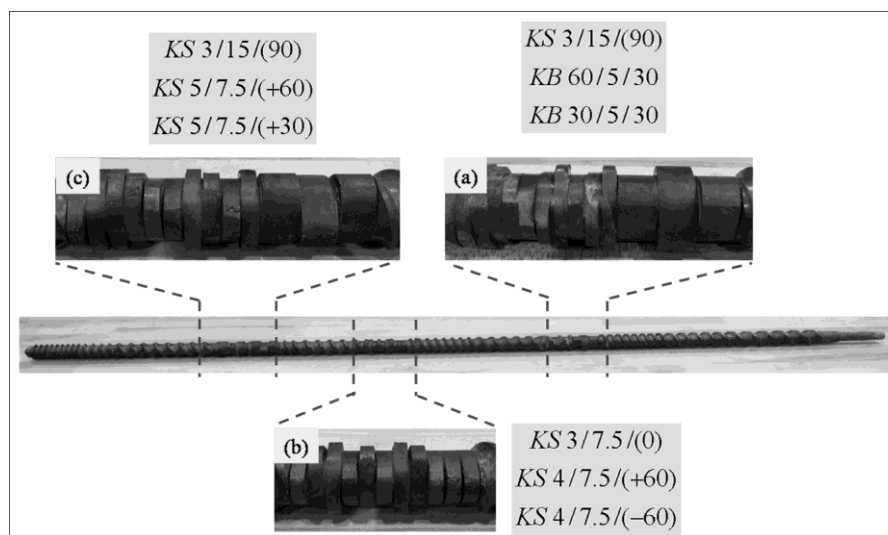


Figure 3.5: Second screw profile: a) 1<sup>st</sup> mixing zone composed of three wide kneading elements with 90° staggering angle followed by two narrow kneading blocks with 30° and 60° staggering angle; b) 2<sup>nd</sup> mixing zone with three kneading elements (0°) followed by 8 kneading elements with both positive (right hand) and negative (left hand) 60° staggering angle; and c) 3<sup>rd</sup> mixing zone including three wide kneading elements with 90° followed by 10 kneading elements with 30° and 60° staggering angle.

### 3.3. Characterization

#### 3.3.1 Morphology

**X-ray diffraction:** To estimate basal spacing,  $d_{001}$ , between silicate layers of PCNs prepared in the first experimental step, wide angle X-ray diffraction (WAXD) (Philips X'pert) with  $\text{CuK}\alpha$  radiation ( $\lambda=1.54056 \text{ \AA}$ ), available at Ecole Polytechnique, was used. The generator was operated at 50 kV and 40 mA. The samples were scanned from 1-10° at 0.01°/s.

To analyze the PCN films and obtain some information about the orientation of clay layers in final product, XRD measurements were carried out using a Bruker AXS X-ray goniometer equipped with a Hi-STAR two-dimensional area detector, available at IMI. The generator was set up at 40 kV and 40 mA and the copper Cu K $\alpha$  radiation ( $\lambda=1.542 \text{ \AA}$ ) was selected using a graphite crystal monochromator. The sample to detector distance was fixed at 12 cm for wide angle X-ray diffraction. To get the maximum diffraction intensity, several film layers were stacked together to obtain a total thickness of about 2 mm.

**Scanning electron microscopy (SEM):** To investigate the distribution level of clay in the prepared PCN at the first experimental step, SEM (Hitachi S4700 with a cold field emission gun, FEG-SEM), available at IMI, was used. The specimens were prepared using an Ultracut FC microtome (Leica) with a diamond knife and then coated with Pt vapor.

**Transmission electron microscopy (TEM):** The quality of clay dispersion was evaluated using TEM (JEOL JEM-2100F, operating at 200 kV), available at Ecole Polytechnique. The samples were microtomed into approximately 50-80 nm thick slices, using the above microtome system at room temperature.

**Image analysis:** TEM micrographs were used to measure the free-path spacing distance between clay layers (the 1<sup>st</sup> experimental step) and the average aspect ratio of dispersed clays (the 2<sup>nd</sup> experimental step). The micrographs were manually digitized using a digitizing table from Wacom and SigmaScan v.5 software, available at Ecole Polytechnique.

### 3.3.2 Thermal Properties

**Thermogravimetric analysis (TGA):** To evaluate the thermal stability of the organoclays and PCNs, TGA (TGAQ500 TA instruments), available at Ecole Polytechnique, was conducted under nitrogen by scanning at 10 °C/min up to 600 °C.

**Differential thermal analysis (DTA):** The thermal behavior of PET and the PCNs in the first phase of the project, was studied at Ecole Polytechnique, using DTA (DSCQ1000 TA instruments), under helium atmosphere, by scanning at 10 °C/min, following successive heating/cooling/heating cycles.

In the second experimental part, the crystallization and melting behavior of the PCN films was studied by scanning at 10 °C/min from 50 to 280 °C. The samples were also annealed at 150 °C for 15-20 min, and the same procedure was applied to the annealed specimens.

Non-isothermal crystallization behavior of PCN films was also investigated under helium atmosphere. The instrument was calibrated by sapphire. The specimens encapsulated in aluminum pans were heated by scanning at 50 °C/min to above melting point and held for 5 min to erase the thermal history. Then, the samples were cooled at cooling rates ranging from 2.5-30 °C/min.

**Differential scanning calorimetry (DSC):** The isothermal crystallization behavior of the PCN films was studied in the chemical engineering department of McGill university, using DSC (Pyris1, Perkin Elmer) equipped with Intracooler 1P, under nitrogen atmosphere. Indium was used as a high purity material to calibrate the instrument. Isothermal crystallization was studied in the temperature range of 195-215°C. The samples enclosed in aluminum pans were heated from 50 to 300°C by scanning at 50°C/min and kept for 5 min above the melting point to erase the thermal history. Then, the specimens were quenched at 150°C/min for isothermal crystallization, which was performed for 15 min. After isothermal crystallization, the samples were heated to above melting point by scanning at 10 °C/min.

**Temperature modulated DSC (MDSC):** Both DSC and DTA have some well-known limitations. Since temperature ranges for transitions in the different materials often overlap, they only measure the sum or average heat flow rate values of overlapping processes. In a

conventional DSC/DTA, a linear heat flow rate is applied and the heat flow is measured. In MDSC, the material is subjected to a linear heat flow rate superimposed by a small amplitude sinusoidal temperature profile:

$$T = bt + A_T \sin(\omega t) \quad (1)$$

where  $b$  is the linear or underlying heat flow rate equal to the chosen ramp in DSC/DTA,  $A_T$  is the temperature modulation amplitude and  $T=2\pi/\omega$  is the temperature modulation period. The basic governing heat transfer equation in thermoanalytical techniques can be expressed as:

$$\frac{dH}{dt} = C_p \frac{dT}{dt} + f(T, t) \quad (2)$$

After Fourier transform and deconvolution of the results, the MDSC signals can be obtained. The left side of this equation represents the total heat flow measured by the instrument and pertains to the linear or average heating rate. The first term on the right hand side is related to the reversing heat flow or heat capacity signal and the second term which is calculated based on the discrepancy of the other signals pertains to kinetic signal and called non-reversing heat flow. Reversing and non-reversing are not related to the thermodynamic concept of reversibility. The reversing signal measures the thermal transition related to the heat capacity changes of the sample like glass transition temperature and melting. While the non-reversing signal represents the kinetic process including crystallization, decomposition and chemical reaction.

To understand the melting endotherms appeared after isothermal crystallization, MDSC (DSCQ1000 TA instruments) was employed and calibrated with sapphire. A linear heating rate 4 °C/min, modulation period 40 sec and temperature amplitude  $\pm 0.42$  °C was selected.

### 3.3.3 Optical Properties

**Appearance:** According to ASTM D1003, haze and clarity of the PCN films, as appearance

criteria, were measured by Haze-gard plus apparatus available at IMI.

**Polarized optical microscope (POM):** For visual observation of isothermal and non-isothermal crystallization behavior of PCN, POM (Olympus BX50) and Linkam hot-stage (Scientific instruments, CSS450), available at McGill university, were used. The same thermal sequence and protocol to DSC and DTA experiments were applied in this technique.

### 3.3.4 Barrier Properties

**Oxygen transmission:** Oxygen transmission rates (OTRs) were determined using an Ox-Tran Model 2/21 oxygen permeability MD Module from Mocon (USA) at 23 °C. 100% dry oxygen was used and all the tests were done under a pressure of 93.3 kPa (700 mmHg). To obtain the permeability coefficient, all measured OTR values have been normalized (multiplied) by the films thickness. For each sample, the measurement was repeated three times. Basically, when the oxygen sensor cell (Coulox), which is a fuel cell, is exposed to oxygen, it generates an electrical current that is proportional to the amount of oxygen entering the sensor. The Coulox sensor has a graphite cathode and a cadmium anode, where the cathodic and anodic reactions are:



The electrical current created by electrons is used to calculate the amount of oxygen entering the sensor.

### 3.3.5 Mechanical Properties

**Tensile Modulus:** Instron 5548 micro tester, available at IMI, was used to measure tensile properties. The rectangular samples, 13 mm wide and 35 mm long were stretched at 25 mm/min using a 2 kN load cell, at ambient temperature.

**Tear resistance:** Resistance to tear propagation of the PCN films was measured in both MD and TD, according to ASTM D1922. A rectangular sample, 3 in. in length by 2.5 in. in width, were cut and plainly marked to denote the intended direction of tear. The required work for tearing is measured based on the angular position of the pendulum during the tearing operation.

**Puncture resistance:** Puncture tests were performed using a 100 N load cell of an Instron 5500R. The samples were pierced by a needle with 0.5 mm radius and 25 mm/min speed. The displacement of the film was recorded against the force (N) and the maximum force was reported as the puncture strength.

## CHAPTER 4

### ORGANIZATION OF ARTICLES

The results of the first experimental step of this study are presented in chapter 5. The effect of compatibility and thermal stability of surfactants on the morphology of PCN was investigated using X-ray diffraction (XRD), scanning electron microscopy (SEM), transmission electron microscopy (TEM) and thermogravimetric analysis (TGA). To obtain quantitative evaluation of the dispersion level in nanocomposite, statistical analysis of TEM micrographs was carried out. It yielded the dispersion parameter,  $D_{0.1}$ , based on free-path spacing measurements. The results showed that the ammonium surfactant yielded the best intercalation results in nanocomposites. However, PCN with phosphonium surfactant exhibits better thermal stability.

In the second part of the project, PCN films were prepared by cast extrusion. The morphology, optical, thermal, barrier and mechanical properties of the products are discussed in details, in chapter 6. Transmission electron microscopy (TEM) and wide angle X-ray diffraction (WAXD) showed that the clay layers were aligned in the machine direction (MD) in the PET/clay nanocomposite (PCN) films. Differential scanning calorimetry (DSC) showed that PCN films have higher crystallinity than the neat PET films, possibly due to the nucleating role of the silicate layers. The PCN films became hazier as the clay content increased, but the film transparency remained in the acceptable range. Oxygen permeability of the PCN films decreased by 23% compared to the neat PET film. This is comparable to predictions of models proposed in the literature. Silicate incorporation brought about 20% increase in the tensile modulus, while the puncture and tear propagation resistance were reduced, due to brittleness of the PCN films. The measured modulus (1.7 GPa) was somewhat smaller than the values predicted using the

Pseudoinclusion model (2.1 GPa).

In chapter 7, the effect of processing conditions on properties of PCN films are presented. Polyethylene terephthalate (PET) nanocomposite films (with 3 wt% Cloisite30B) were prepared by cast extrusion followed by uniaxial stretching, using chill rolls. Two screw profiles with different mixing elements under different screw speed ( $N$ ) and feeding rate ( $Q$ ) were used to prepare PET/clay nanocomposite (PCN) films. Transmission electron microscopy (TEM) and wide angle X-ray diffraction (WAXD) showed that the clay layers were aligned in the machine direction (MD). XRD patterns depicted that the interlayer distance of clay platelets in the state of intercalation is somehow independent of the processing conditions, but the macro-scale characterization, including barrier and mechanical properties showed that the level of clay layer delamination was affected by processing conditions. The results reveal that the applied shear has stronger effect than residence time on the barrier and mechanical properties. At the highest screw speed ( $N=250$  rpm), 27% reduction in oxygen permeability and 30% improvement in tensile modulus were obtained for the more severe screw profile.

According to the effect of clay on crystallinity of polymer, isothermal and non-isothermal crystallization kinetics of PCN was also studied in Appendix A. To evaluate the kinetic parameters of crystallization, our efforts in this part is focused on the PCN incorporated with only 1 wt.% C30B. However, Avrami theory shows that overall, isothermal crystallization of PCN takes place faster, but further analysis using Lauritzen-Hoffman treatment revealed that the presence of clay leads to less perfect crystalline structure. In other words, the equilibrium melting point of PCN appears at higher temperature and the required work for chain folding in the presence of clay is a bit higher than neat PET. Temperature modulated DSC (MDSC) was employed to shed more light on the multiple melting endotherms phenomenon observed during the heating of isothermally crystallized samples. It revealed that the third endotherm attributes to

the recrystallization and melting of the crystals reorganized during heating, whereas the first and second one are associated with melting of secondary and primary crystals, respectively. The modified Avrami equation and the combined Avrami-Ozawa method were also applied to describe the non-isothermal crystallization process. The calculated effective barrier energy for PCN was higher than PET, which indicates less perfect crystalline structure for PCN during non-isothermal crystallization. Polarized optical microscope (POM) was also used for qualitative direct observation of PCN crystallization.

## CHAPTER 5

# Preparation and characterization of PET/Clay nanocomposites by melt compounding<sup>1</sup>

Ghasemi Hesam<sup>1</sup>, Carreau Pierre J.<sup>1</sup>, Kamal Musa R.<sup>2</sup>, Calderon Jorge U.<sup>2</sup>

1) CREPEC, Chemical Engineering Department, Ecole Polytechnique  
2500 Chemin Polytechnique, H3T 1J4, Montreal, Quebec, Canada

2) CREPEC, Department of Chemical Engineering, McGill University  
3610 University Street, H3A 2B2, Montreal, Quebec, Canada

### Abstract

Poly(ethylene terephthalate) (PET) nanocomposites were prepared via melt compounding using a twin-screw extruder at 265 °C. Three different types of organomodified clay were melt-compounded with PET: a commercial ammonium-modified silicate clay (Cloisite 30B) and specially prepared thermally stable phosphonium and imidazolium-modified montmorillonites. X-ray diffraction, scanning electron microscopy (SEM), transmission electron microscopy (TEM) and thermogravimetric analysis (TGA) were used to characterize and evaluate the quality of the nanocomposites. To obtain quantitative evaluation of the dispersion level in nanocomposites, statistical analysis of TEM micrographs was carried out, using a dispersion parameter,  $D_{0.1}$ , based on free-path spacing measurements. The results showed that the ammonium surfactant yielded the best intercalation results in nanocomposites.

---

1. Accepted in *Polymer Engineering and Science*

## 5.1 Introduction

Poly(ethylene terephthalate) (PET), a semi-crystalline engineering polymer, exhibits many properties that are desirable for barrier applications. These properties include polarity, high chain stiffness, close chain packing via symmetry, intermolecular bonding, high glass transition temperature and crystallinity. However, gas permeability to CO<sub>2</sub> and oxygen has been a challenge in some applications, such as soft drink and beer packaging. Despite the significant improvement of barrier properties by surface modification via various coating techniques, including plasma enhanced chemical vapor deposition and reactive evaporation, the brittleness and high cost of the coated films have limited the commercial use of coating techniques [1-3]. A commonly used alternative approach involves increasing the tortuosity of the diffusion path by geometrical hindrance. Typical methods involve increasing crystal thickness, removal of crystal defects and sharpening the boundary between the amorphous and crystalline regions by annealing [4]. Other methods employ reduction of solubility and diffusion coefficients of the permeant by blending and/or orientation [5]. Thus, a PET/thermotropic liquid crystalline blend shows more than 50% gas permeability reduction. However, the binary blend has poor mechanical properties due to lack of adhesion and compatibility [6]. Upon biaxial orientation of PET/aromatic polyamide or polyester blends, the dispersed domains are altered to form parallel and extended layers, thus causing improvement in barrier properties [7-8]. Notwithstanding the positive effects of biaxial orientation on barrier properties, the need for compatibilization and the possibility of transesterification present critical issues.

The introduction of layered silicate nanoclays, as an impermeable nanoparticle phase in a polymer matrix, is an attractive approach to enhance gas barrier properties [9]. The impermeable silicate layers create a tortuous path within the polymer matrix. As a result, gas molecules

penetrate the material with more difficulty. The planar shape and high aspect ratio of clay particles should lead to improved gas barrier properties at low concentration of clay. This approach is less expensive and more efficient than other methods. Melt compounding and in situ polymerization are the main techniques employed to produce PET nanocomposites. Melt compounding is the preferred method for preparation of polymer nanocomposites, which has environmental and cost advantages, due to the absence of solvents and monomers. Furthermore, the high deformation rates employed in melt extrusion compounding are useful for dispersion of nanoparticles in the molten polymer matrix.

Various issues arise in the processing of PET at high temperature to produce polymer/clay nanocomposites (PCNs). These include thermal stability of the organically modified clay, thermal stability of PET and compatibility between PET and the organic modifier. Maleic anhydride and pentaerythritol have been used as coupling agents to improve the dispersion of clay particles in PET [10-11]. However, while the Young modulus increased with the incorporation of the nanoclay, the effect of the coupling agent on the mechanical properties was negligible [11]. An alternative approach consists of PET chain modification to enhance interactions between the matrix and clay. The random incorporation of sulfonate functionalities along the polymer backbone led to electrostatic interactions between the sulfonate groups and platelets of clay and facilitated chain segment penetration into the clay galleries [12]. At the high processing temperatures required for melt compounding of PET nanocomposites, the degradation of conventional organic modifiers presents a major problem. Modification of the clay surface with hexadecyl imidazolium [13] and hexadecyl-quinolinium bromide [14] improved clay dispersion. Moreover, TGA results showed a higher degradation temperature for the mostly delaminated nanocomposites. Organic-inorganic hybrid layered zirconium phenylphosphonate yielded an intercalated structure, and corresponding nanocomposites exhibited improved thermal

stability, according to TGA results [15]. The exclusion of organic modifiers based on solvent-nonsolvent systems led to better optical and thermal properties and less mechanical degradation of PET PCNs. In the above, PET and organoclay were dissolved in the mixture of chloroform and trifluoroacetic acid. Then the modifier was eliminated by using cold methanol as a non-solvent [16].

Recent studies have shown that phosphonium and imidazolium surfactants significantly improved the thermal stability and dispersion quality of polystyrene PCNs [17] and polyolefin PCNs [18]. Moreover, Cloisite 30B showed the best dispersion among a group of ammonium-modified montmorillonite (MMT) clays [19]. In this work, we evaluate the characteristics and performance of PET PCNs, prepared by melt compounding with Cloisite 30B and phosphonium and imidazolium-modified MMTs. Our efforts are focused on the morphological studies and the effect of different surfactants on the dispersion level of silicate layers. Mechanical, barrier and optical properties of PET/clay nanocomposite films will be presented elsewhere.

## **5.2 Experimental**

### **5.2.1 Materials**

An experimental grade high viscosity PET, Selar PTX295 (DuPont), was used in this study. The following organoclays were also used: Cloisite 30B (Southern Clay Co.), and MMTs modified in our laboratories with phosphonium [20], imidazolium and pyridinium surfactants [21]. The characteristics of the materials and chemical structure of the surfactants are summarized in Table 5.1 and Figure 5.1, respectively. As shown in Table 5.1, the phosphonium, imidazolium and pyridinium-modified clays exhibit higher thermal stability, as indicated by 5 wt% mass reduction related temperature ( $T_{5\%}$ ) in TGA experiments, than Cloisite 30B (C30B). For a more reliable

comparison, the neat PET pellets underwent the same melt processing conditions.

## 5.2.2 Melt Compounding

Melt compounding was carried out in a co-rotating twin screw extruder (TSE) (Leistritz ZSE 18 HP). The organoclay content was 2 wt% (nominal value) for the cases of C30B and phosphonium-modified MMT. Owing to limited available quantities, in the imidazolium and pyridinium-modified MMT cases, the organoclay content was 1.25 wt% (nominal value). The TSE screw diameter was 18 mm and the length/diameter (L/D) ratio was 40.

Table 5.1: Characteristics of the neat polymer and organically-modified clays

<i>PET</i>			
Code	$T_g$ (°C)	$T_m$ (°C)	
PTX295	83	248	
<i>Modified Clay</i>			
Code	Modifier	$T_{5\%}$ (°C)	$d$ -spacing (nm)
C30B	quaternary ammonium	233	1.84
C16-Im	1-vinyl hexadecyl imidazolium	287	1.78
2C16-Im	dihexadecyl imidazolium	271	2.20
C16-Py	hexadecyl pyridinium	288	1.76
P00208	tributyl tetradecyl phosphonium	320	2.13
P00308	tetrabutyl phosphonium	365	1.62
P00408	4-carboxybutyl triphenyl phosphonium	313	1.85

Figure 5.2 depicts the screw configuration. After the conveying and pressuring elements, the first mixing zones with 30, 60 and 90° elliptical elements are located as indicated in Figure 5.2a. The second (Figure 5.2b) and third (Figure 5.2c) mixing zones have 30 and 60° elliptical elements,

respectively. A circular die of 2 mm diameter was mounted on the barrel exit, and a water-ice bath was employed to cool the extrudate. In order to obtain a uniform feeding mixture, PET pellets were ground into a powder and dry-mixed with clay before feeding into the TSE hopper. PET PCNs were prepared at 175 rpm and the temperature profile of 240, 275, 270, 265, 265, 265, 265 and 260 °C. The nanocomposites extrudates were granulated and compression molded at 270 °C, under a purge of nitrogen, to obtain 25 mm disks. The obtained samples were used for X-Ray and morphological analysis. Since PET is sensitive to moisture, which has strong influence on its processing and performance properties, PET pellets and PET pelletized extrudates were dried in a vacuum oven at 110 °C for 24 h before mixing and molding. The C30B and the other modified clays were also dried at 50 and 110 °C under vacuum, respectively.

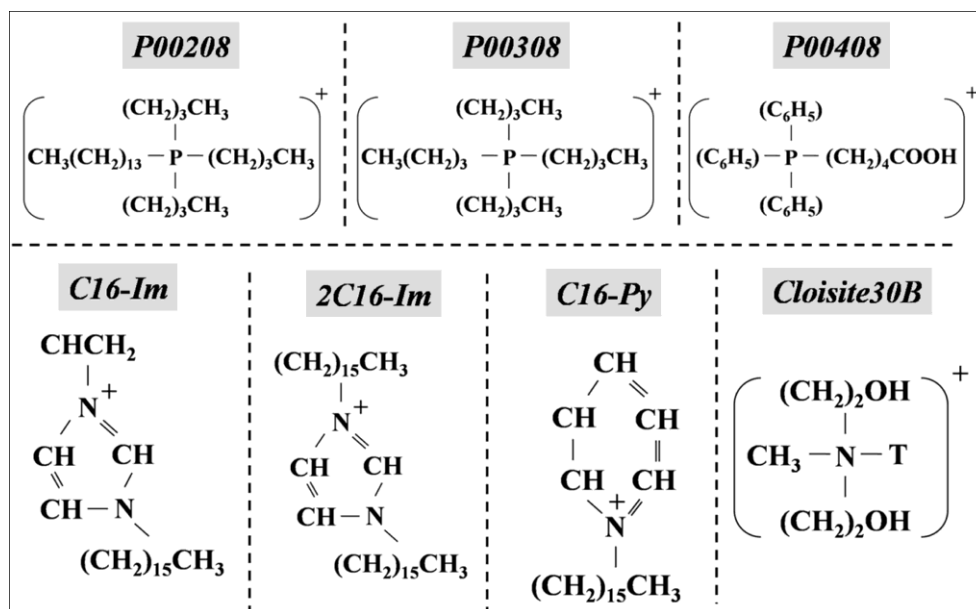


Figure 5.1: Chemical structure of the surfactants. The negatively charged counter-ions are chlorine or bromine

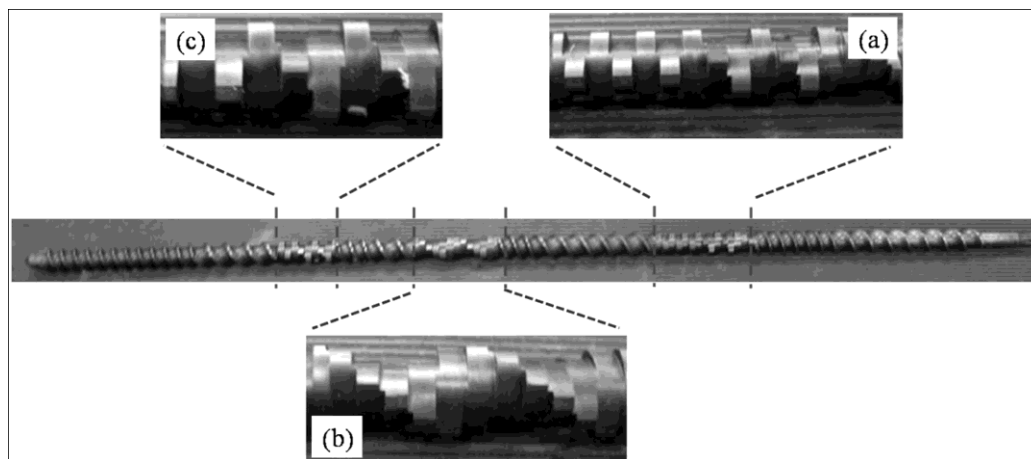


Figure 5.2: Screw configuration: *a*) 1<sup>st</sup> mixing zone with 30, 60 and 90° elliptical elements; *b*) 2<sup>nd</sup> mixing zone with 30° elliptical elements; *c*) 3<sup>rd</sup> mixing zone with 60° elliptical elements

### 5.2.3 Characterization

Wide angle X-ray diffraction (WAXD) (Philips X'pert) with CuK $\alpha$  radiation ( $\lambda=1.54056 \text{ \AA}$ ) was used to estimate basal spacing ( $d_{001}$ ) between silicate layers. The generator was operated at 50 kV and 40 mA. The samples were scanned from 1-10° at 0.01°/s.

Thermogravimetric analysis (TGA) (TGAQ500 TA instruments) was conducted under nitrogen by scanning at 10 °C/min up to 600 °C, to evaluate the thermal stability of the organoclays and PET PCNs.

Scanning electron microscopy (SEM) (Hitachi S4700 with a cold field emission gun, FEG-SEM) was used to investigate the distribution of clay in the PET matrix. The specimens were prepared using an Ultracut FC microtome (Leica) with a diamond knife and then coated with Pt vapor.

The quality of clay dispersion was evaluated using transmission electron microscopy (TEM) (JEOL JEM-2100F, operating at 200 kV). The samples were microtomed into approximately 50-80 nm thick slices, using the above microtome system at room temperature.

TEM micrographs were used to measure the free-path spacing distance between clay layers. The micrographs were manually digitized using a digitizing table from Wacom and SigmaScan v.5 software.

The thermal behavior of PET and the PCNs was studied, using differential scanning calorimetry (DSC) (DSCQ1000 TA instruments), under helium atmosphere, by scanning at 10 °C/min, following successive heating/cooling/heating cycles.

## **5.3 Results and discussion**

### **5.3.1 Ammonium surfactant**

The presence of two hydroxyl groups in C30B could bring about good compatibility between PET chains and the organoclay. On the other hand, they are suspicious of thermal degradation of the modifier at the processing temperature of PET.  $T_{5\%}$  of C30B occurs at around 30 °C below the processing temperature (Table 5.1). Moreover,  $T_{5\%}$  of PCN containing C30B is lower than that of neat PET extrudate (Table 5.2). Incorporation of a larger amount of C30B causes further reduction in the thermal stability of the resulting PCN. At 4 wt% nominal content of C30B,  $T_{5\%}$  of the PCN is 368 °C, which is 9 °C lower than  $T_{5\%}$  for the PCN containing 2 wt% C30B (Table 5.2). XRD shows that the  $d$ -spacing for C30B is around 1.8 nm (Table 5.1). The PCN incorporating C30B exhibits two distinct peaks. The first ( $d$ -spacing~3.5 nm) reflects intercalation of the clay layers and the second ( $d$ -spacing~1.6 nm) implies the degradation or the exuding of the modifier or could be related to a reflection of the first peak. As a result of various factors, including the random orientation of silicate layers, the inhomogeneous distribution of surfactant in the interlayer space, and the distribution of interlayer spacing, it is not possible to obtain a complete and detailed evaluation of the state of delamination of clay layers on the basis

of XRD analysis alone [22]. Thus, the XRD results should be coupled with direct observation by SEM and TEM analysis.

In SEM images (Figure 5.3), the quality of the distributive mixing of the tactoids appears to be good. Clay aggregates in C30B PCN are probably due to poor mixing and, in part, to the collapse of silicate layers as a result of degradation of the modifier at the processing temperature.

Table 5.2: TGA and XRD results of PCNs

	$T_{5\%}$ (°C)	Gallery opening $\Delta d_{001}$ (nm)
Neat PET -- Extrudate	385	----
PCN -- 2% C30B	379	1.7
PCN -- 1.25% C16-Im	382	1.5
PCN -- 1.25% 2C16-Im	384	1.1
PCN -- 1.25% C16-Py	380	1.6
PCN -- 2% P00208	388	0.60
PCN -- 2% P00308	387	0.20
PCN -- 2% P00408	388	0.05

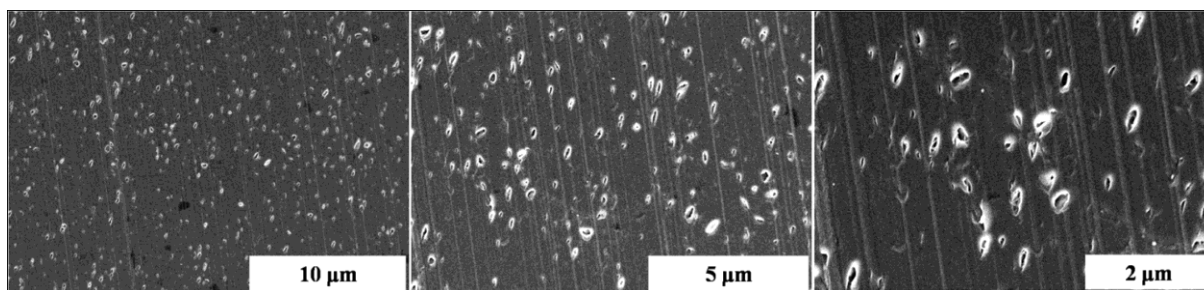


Figure 5.3: SEM images of the PCN with 2 wt% C30B

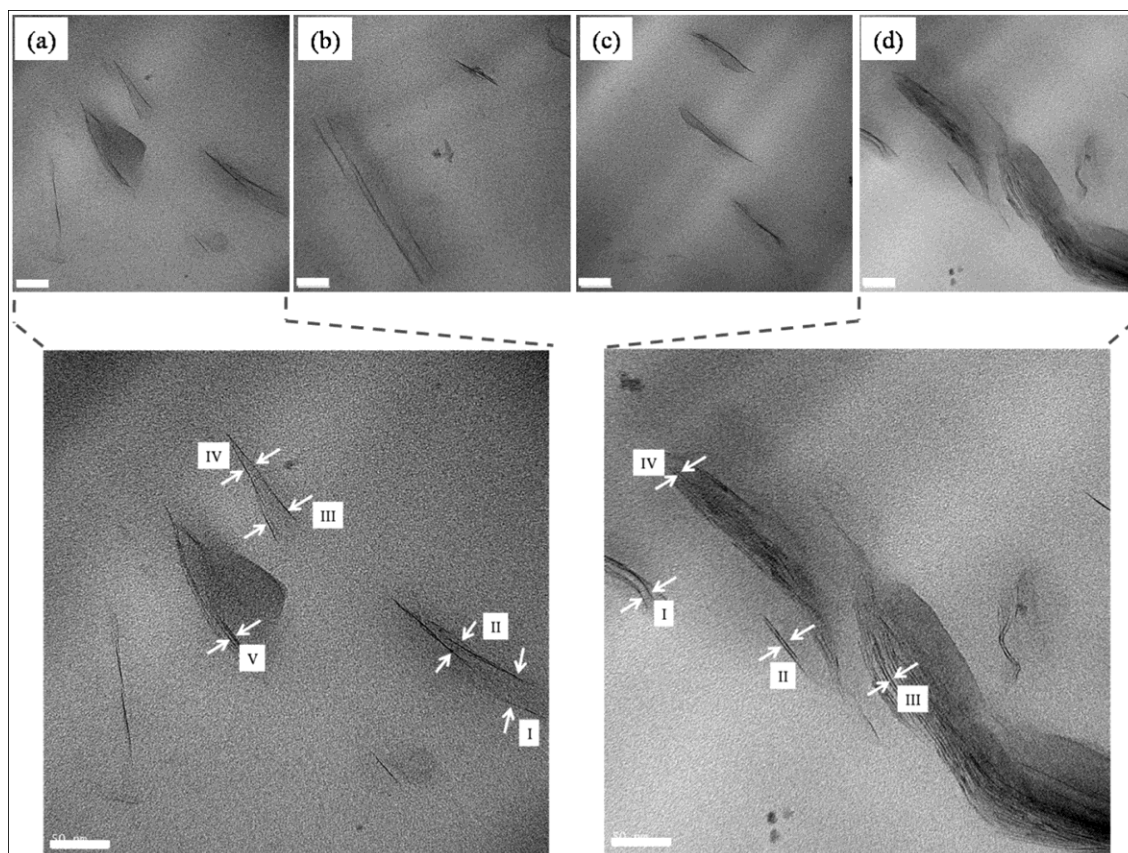


Figure 5.4: TEM images of the PCN with 2 wt% C30B (All scale bars represent 50 nm)

The results of the TEM analysis (Figure 5.4, a-d) are in agreement with the XRD patterns. Both individual platelets and tactoid aggregates are seen in the micrographs. The marked distances in Figure 5.4a (I~21.3, II~6.91, III~17.9, IV~6.01 and V~2.62 nm) represent partially an exfoliated and intercalated structure of PCNs with C30B. These results could not be obtained using XRD alone. Moreover, the *d*-spacings indicated in Figure 5.4d (I~5.96, II~2.15, III~1.73, IV~2.28 nm) reveal partial intercalation and collapse of silicate layers. The expansion of the gallery spacing may be associated with the compatibility between the organoclay and the PET chains, while the collapse or reduction of basal spacing may be attributed to degradation of the modifier. Figure 5.5 illustrates the break-up and peeling mechanisms that take place during melt compounding. The former involves overcoming the cohesive forces between clay layers by the

compounding stresses [23], while the latter is due to exerted shear stress by the penetrating polymer matrix [24].

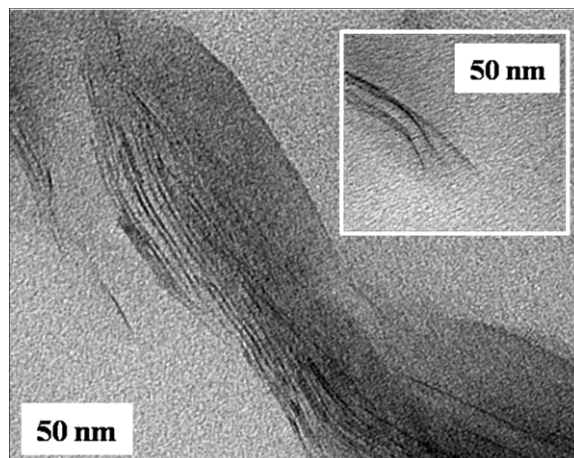


Figure 5.5: Various intercalation mechanisms for the PNC containing 2 % C30B. The main micrograph shows the break-up and inset depicts peeling.

Recently, a technique based on free-path spacing distance,  $D_{0.1}$ , was introduced to provide a quantitative estimate of the degree of layer dispersion in PCNs [25-26]. In this method, a random line (usually vertical or horizontal) is drawn to intercept the clay layers in a TEM micrograph. The free-path distance,  $x_i$ , between the platelets is measured. After constructing a histogram from calculated data (more than 100 measurements),  $D_{0.1}$  is defined as the probability of the free-path distance distribution in the range of  $\bar{x} \pm 0.1$  [25]:

$$D_{0.1} = 1.1539 \times 10^{-2} + 7.5933 \times 10^{-2} (\bar{x}/s) + 6.6838 \times 10^{-4} (\bar{x}/s)^2 - 1.9169 \times 10^{-4} (\bar{x}/s)^3 + 3.9201 \times 10^{-6} (\bar{x}/s)^4 \quad (1)$$

where  $\bar{x}$  and  $s$  are the mean and standard deviation values of a set of free-path data. Values of  $D_{0.1}$  over 8 % indicate an exfoliated structure, and values between 4 and 8 % indicate intercalation, while values lower than 4 % suggest an immiscible morphology [26]. The histogram and statistical results of free-path spacing for the PCN with C30B is displayed in

Figure 5.6a. The appearance of a sharp peak at low spacing and the value of 6.8% obtained for  $D_{0.1}$  provide further quantitative evidence of intercalation. The results of Figure 5.6b are discussed below in the section on phosphonium surfactants.

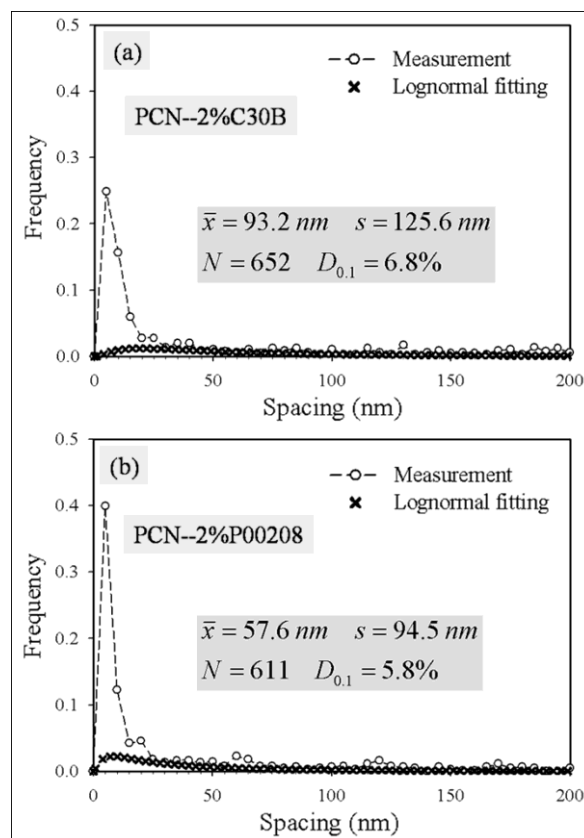


Figure 5.6: Layer spacing histogram of: a) the PCN with 2 wt % C30B; and b) the PCN with 2 wt% P00208

### 5.3.2 Imidazolium surfactants

Imidazolium and pyridinium-modified clays (see Table 5.1 and Figure 5.1) were melt-compounded with PET. XRD patterns reveal two distinct peaks for these nanocomposites (Table 5.2), which imply partial intercalation ( $d$ -spacing~3.3 nm) and also reduction of basal spacing ( $d$ -spacing~1.6 nm) due to degradation or exudation of the modifier from the silicate galleries. These observations are in harmony with the thermal stability results summarized in Table 5.1. However TGA shows better thermal stability for imidazolium and pyridinium-modified clays

than for C30B, but  $T_{5\%}$  is close to the processing temperature. The C=C and vinyl bonds are likely contributors to thermal degradation of modifiers.

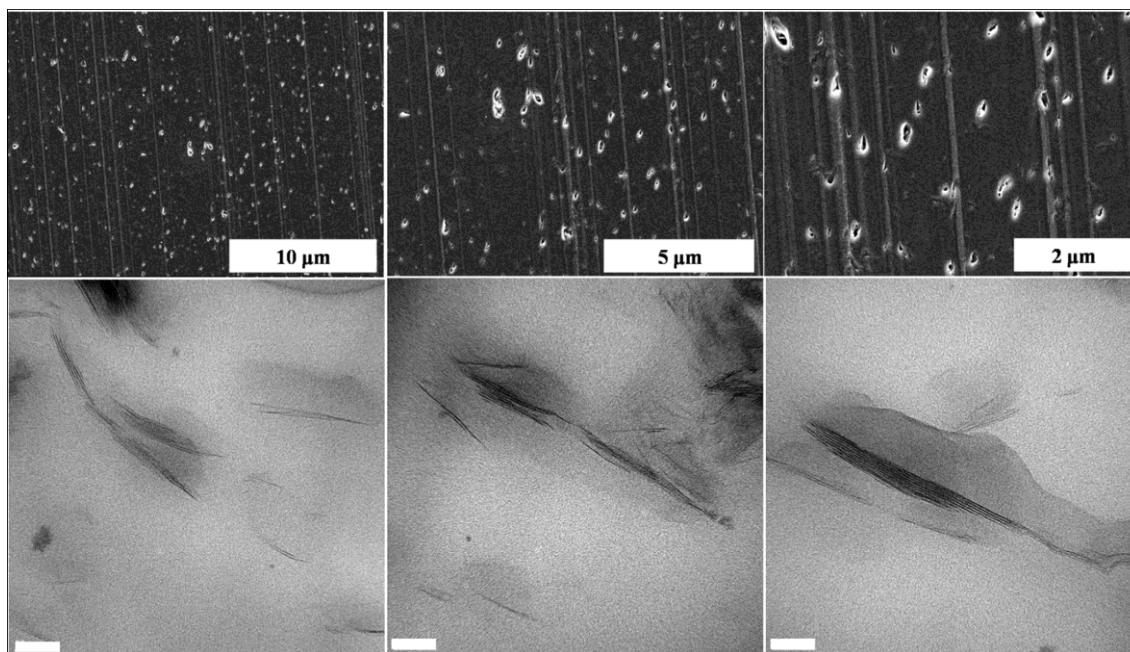


Figure 5.7: Morphology of the PCN containing 1.25% 2C16-Im a) SEM; and b) TEM (All scale bars in TEM micrographs represent 50 nm)

SEM micrographs of the PCNs containing 2C16-Im, which has the highest gallery spacing among the surfactants under consideration, show that the distribution of silicate layers in the matrix is acceptable (Figure 5.7a). Although the amounts of these clays were lower than C30B, some small aggregates could be observed. TEM micrographs also display partially intercalated structure and dispersed clay tactoids (Figure 5.7b). The SEM and TEM micrographs of the PCNs with C16-Im and C16-Py exhibited the same results. Regarding the chemical structure of the modifiers (Figure 5.1), lack of compatibility between PET chains and imidazolium and pyridinium surfactants could be an explanation for presence of tactoids in the system, instead of individual silicate layers. Regardless of improvement in thermal stability, compared to C30B, the poor dispersion level of clay layers is an important issue. Besides, these modified clays were lab-

made and only small quantities of them were available. Nevertheless, it allows for a qualitative comparison of the dispersion levels of these clays with other types of modified clay used in this work, hence providing helpful information for further investigations.

### 5.3.3 Phosphonium surfactants

In view of the low thermal stability of ammonium surfactants, a number of phosphonium surfactants were included in this study. These compounds and corresponding organoclays have shown improved resistance to thermal degradation at the processing temperature of PET (Table 5.1). The characteristics of these compounds are given in Table 5.1 and Figure 5.1. P00408, which contains carboxylic groups, was expected to provide better compatibility with PET. However, the XRD results of Table 5.2 indicate no change in the position of the nanocomposite peak and the SEM micrographs of Figure 5.8 show an important quantity of large aggregates in the nanocomposite.

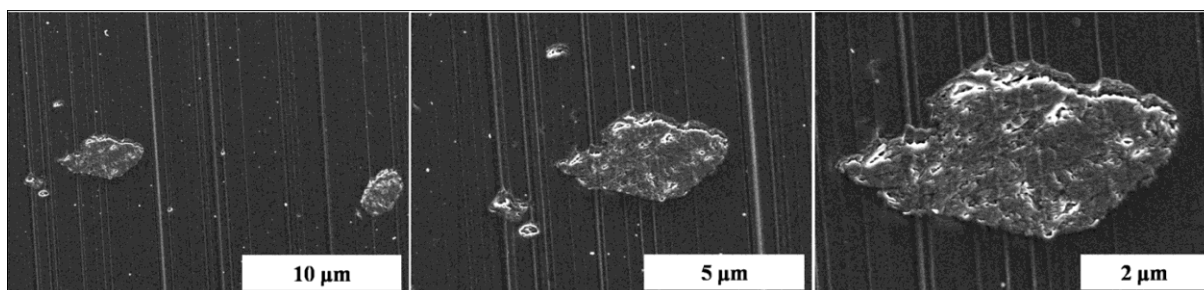


Figure 5.8: SEM images of the PCN containing 2% P00408

In the second phosphonium-modified clay, P00308, the carboxyl functionality is removed and the butyl groups are substituted for the rigid phenyl groups of P00408. While P00308 exhibited good thermal stability, XRD results of the corresponding nanocomposite showed little change in the position of the peak that was observed for the organoclay (Table 5.2). Moreover, the SEM micrographs of Figure 5.9 show the presence of large agglomerates in the system.

Apparently, the small pendant alkyl and rigid phenyl groups in P00308 and P00408, respectively, produce higher packing density of the modifier between the silicate layers. The aligned, confined and lateral arrangement of the modifier could bring about impediment to diffusion of polymer chains into the silicate interlayer space. Considering the interdigitated layer structure of organomodified clays [27] and effect of molecular length of surfactant on gallery opening [28], form factors for the phosphonium modified clays are calculated and presented in Table 5.3. The number of surfactant molecules per unit surface area was estimated from the specific surface area of the pristine clay ( $758 \text{ m}^2/\text{g}$ ) [29]. Assuming that the clay thickness is equal to 1 nm, the gallery opening can be obtained from XRD results (Table 5.1).

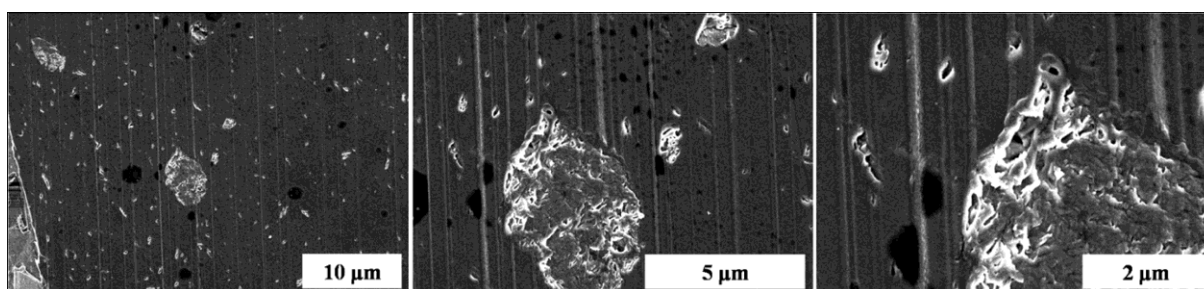


Figure 5.9: SEM images of the PCN containing 2% P00308

Table 5.3: Form factors of phosphonium-modified clays

	Ash content (%)	Molecules/ $\text{m}^2$ ( $10^{17}$ )	Molecular length (nm)	Gallery height nm	Tilt Angle ( $^\circ$ )
P00408	72	8.5	0.95	0.85	63.5
P00308	82	6.7	0.53	0.62	39.2
P00208	72	7.7	1.86	1.3	38.2

As seen in Table 5.3, the tilt angle of P00408 with rigid pendant phenyl groups is more than that of P00308. It also has more molecules per unit surface of clay. Therefore, there are less available sites for PET chains to reach the surface of the clay. However, the gallery height of

P00308 is a little more than the molecular length of the modifier, but the number of molecules is of the same order of magnitude as for P00408. It means that the packing density of the surfactant leads to saturation of the clay surface and prevents polymer chains to diffuse into the gallery.

Phosphonium surfactant P00208 incorporates a long alkyl chain as a substitute for one of the butyl group of P00308. However, as indicated by  $T_{5\%}$  (Table 5.1), its thermal stability at the processing temperature remains satisfactory. XRD shows that the peak has been shifted to a lower angle. Thus, basal spacing is increased (Table 5.2). Moreover, the SEM images of Figure 5.10 suggest that the distribution of silicate layers in the system is acceptable. The TEM images of PCN incorporating P00208 depict partially intercalated structure and the presence of agglomerates in the form of tactoids (Figure 5.11, a-d). The specified distances in Figure 5.11a (I~9.35, II~4.71, III~2.28 and IV~1.85nm) indicate partially intercalated arrangement of the silicate layers in the system. Figure 5.11d is in agreement with XRD patterns (I~3.21, II~2.69, III~2.64 and IV~2.04 nm). Also, this figure provides some information regarding the mechanism(s) of silicate layer delamination.

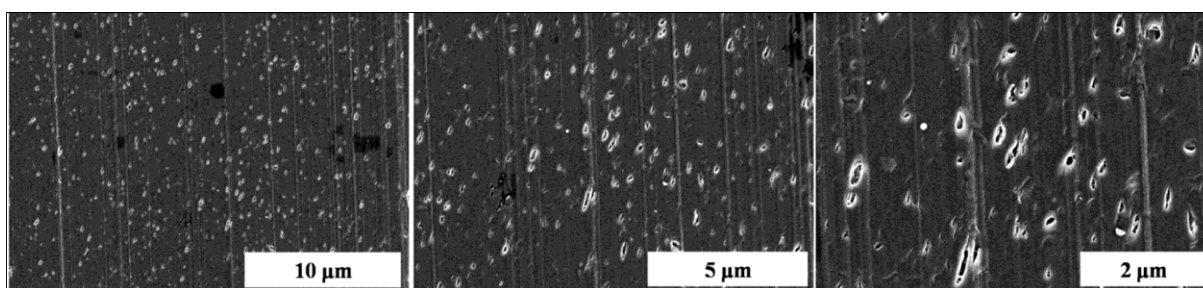


Figure 5.10: SEM images of the PCN containing 2% P00208

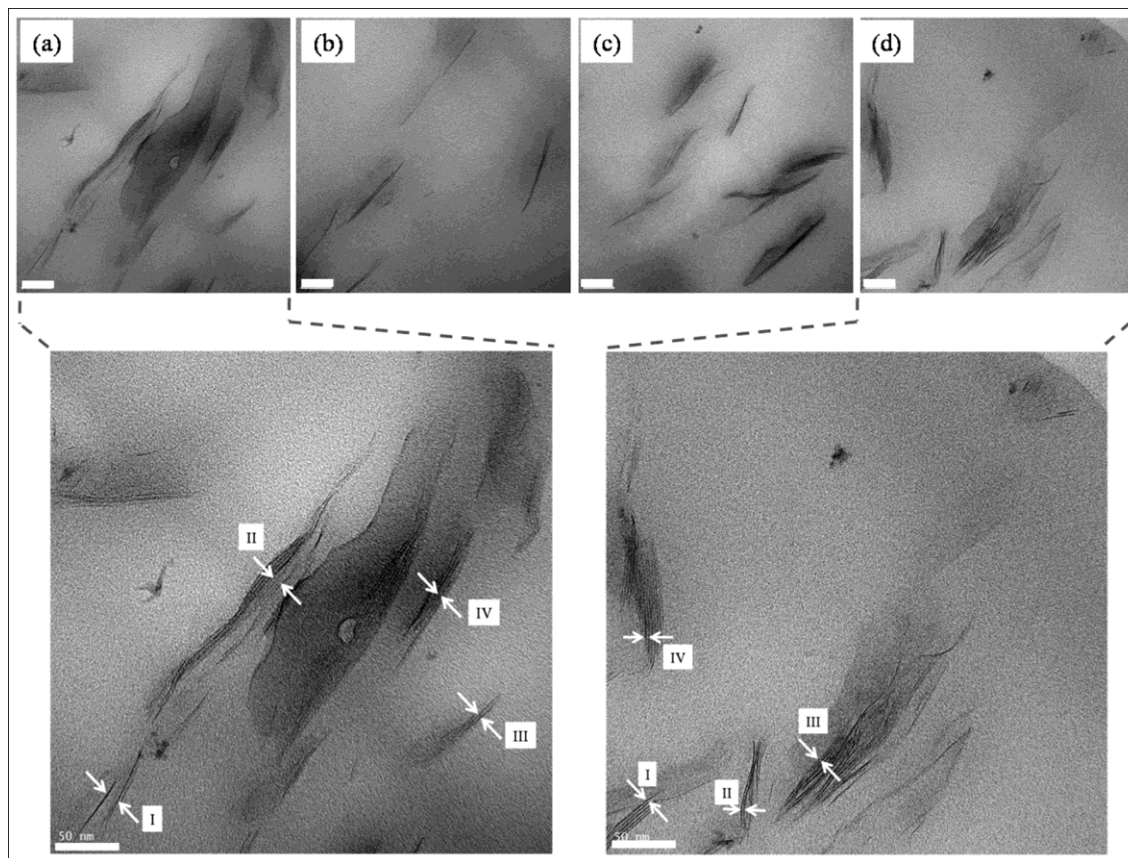


Figure 5.11: TEM images of the PCN with 2% P00208 (All scale bars represent 50 nm)

The statistical results of Figure 5.6b show that the free-path spacing distance,  $D_{0,1}$ , of PCN with P00208 is 5.8%, which is 1% lower than the value obtained for PCN with C30B. In the case of the PCN with P00208, the histogram of the free-path spacing reveals a higher peak at a lower spacing than the PCN with C30B. This indicates that the corresponding nanocomposite has more tactoids and a clustered structure. Various factors might explain the larger quantity of tactoids in the phosphonium based nanocomposites. These include lower diffusivity of PET into the gallery spacing of the silicate layers and possibly the need for employing a more intensive mixing for the case of phosphonium systems. The Hamaker constants calculated for these phosphonium-modified clays at the processing temperature are larger than the value for C30B [30]. The interlayer population density influences the degree of intercalation in the system. Although, the

organophilicity of the clay is enhanced by a higher interlayer population density, the PET chains would penetrate with difficulty the galleries due to saturation by surfactant molecules or high organic content. Compared to the first two phosphonium surfactants, P00208 has one long aliphatic tail, which can provide more sites at the surface of the clay for interaction with the polymeric chains.

Figure 5.12 displays the comparison between DSC results of PCNs with C30B and P00208. The first heating cycle was conducted to erase the thermal history of the sample. In the second cycle, the melted sample was cooled. The peak of the crystallization temperature appears at higher temperatures (Figure 5.12a) and the rate of crystallization increases (Figure 5.12b) with incorporation of clay (Table 5.4). The relative degree of crystallinity (Figure 5.12b) is obtained by calculating the area under the exothermic crystallization peak in the cooling cycle (Figure 5.12a), i.e.

$$X_t = \frac{\int_0^t dH_C(t) dt}{\int_0^{t_\infty} dH_C(t) dt} \quad (2)$$

where  $H_C(t)$  is the heat flow at time  $t$  and  $t_\infty$  is the end of crystallization. The degree of crystallinity was calculated according to the following equation:

$$\text{Crystallinity}(\%) = \frac{\Delta H_C}{\Delta H_0(1-x)} \quad (3)$$

where  $x$  indicates the percentage of clay,  $C$  index represents the cold crystallization and  $\Delta H_0$  refers to the heat of fusion of 100% crystalline PET, which is 115 J/g [31].

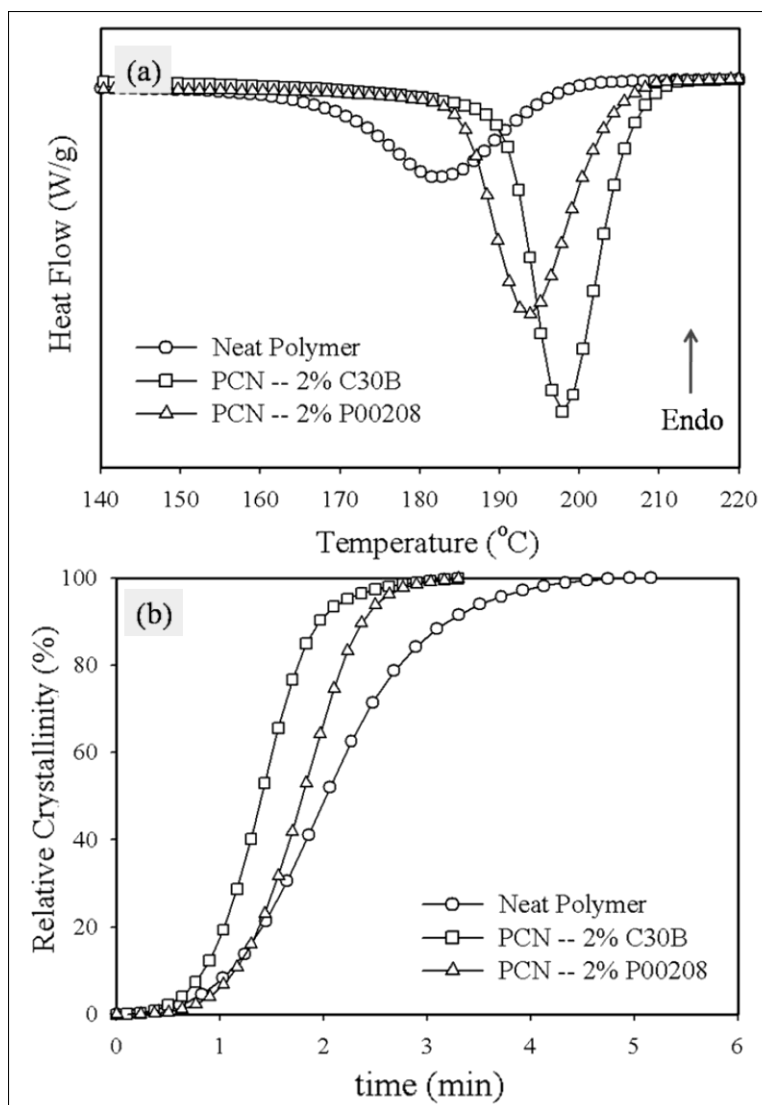


Figure 5.12: DSC results of the PCNs with C30B prepared by TSE, at 10°C/min *a*) Cooling cycle (2nd cycle); and *b*) Relative crystallinity vs. time

Table 4 shows that the value of  $t_{1/2}$  decreases in the presence of clay. It means that the overall rate of quiescent crystallization increases, which is proportional to the  $t_{1/2}$ , reciprocally. This behavior is usually explained by the nucleating role of silicate layers in the system [32-33]. According to the state of delamination (see Figure 5.6) and also TEM micrographs (Figure 5.4 and Figure 5.11), the higher cold crystallization temperature and lower  $t_{1/2}$  of PCNs with C30B

could be attributed to a better intercalation. Since the lab-made thermally stable phosphonium modified clay was washed with distilled water several times and titrated with silver nitrate to detect any trace of chloride [20], the increase of the crystallization rate pertains to the nucleating effect of silicate layers. On the other hand, degradation of PET in the presence of C30B is plausible [34] suggesting that a reduction of molecular weight may contribute to the increment in the overall crystallization rate [35]. However, in this study, PCNs with C30B exhibited a better intercalated structure than the phosphonium modified clay and its crystallization started sooner. More research efforts are required to shed light on the role of either clay or molecular weight reduction on the crystallization behavior of PCNs.

Table 5.4: DSC results of PCNs with C30B

	$T_c$	$t_{1/2}$	Crystallinity
	(°C)	(s)	(%)
Neat Polymer	182.1	121.5	34.7
PCN -- 2% C30B	197.9	84.2	36.9
PCN -- 2% P00208	193.5	107.9	35.7

## 5.4 Conclusion

PET PCNs were prepared using a twin-screw extruder by melt compounding of PET with different types of clay, including a commercial ammonium-based surfactant (C30B), experimental thermally stable phosphonium surfactants (P00 series) and experimental thermally stable imidazolium surfactants. The properties of the PCNs containing these new modifiers were compared in terms of thermal stability and various factors contributing to the quality of

dispersion. The phosphonium based nanocomposites exhibited better thermal stability, but they showed a lower degree of intercalation than the ammonium and imidazolium-based nanocomposites. Nanocomposites incorporating P00208 exhibited a better dispersion than those incorporating the other phosphonium compounds. A higher dispersion parameter,  $D_{0.1}$ , for PCNs with C30B was obtained compared to PCNs incorporating P00208.

From a comparison between the different modified clays, prepared in this study under the same extrusion conditions the PCNs with C30B exhibited a better dispersion and intercalation than the phosphonium and imidazolium modified clays. On the other hand, the thermal stability of the phosphonium modified clays was significantly better than the C30B systems. Since our efforts in this step were only concentrated on morphological effects of different types of modified clay, further investigations are required to optimize the chemical structure of the surfactants and the processing conditions (including applied shear), in order to achieve both improved dispersion and thermal stability of PET nanocomposites.

## 5.5 Acknowledgments

The authors would like to gratefully thank CREPEC members, Dr. Karen Stoeffler who provided thermally stable imidazolium and pyridinium-modified clays and Ms. Leelapornpisit who prepared SEM and TEM micrographs. We also thank DuPont Canada for supplying the PET resins used in this study.

## 5.6 References

1. C.P. Barker, K.H. Kochem, K.M. Revell, R.S.A. Kelly, and J.P.S. Badyal, *Thin Solid Films*, **259**, 46 (1995)

2. E. Schmachtenberg, F.R. Costa, and S. Gobel, *J. Appl. Polym. Sci.*, **99**, 1485 (2006)
3. P. Zhu, M. Teranishi, J. Xiang, Y. Masuda, W.S. Seo, and K. Koumoto, *Thin Solid Films*, **473**, 351 (2005)
4. W. Perkins, *Polym. Bull.*, **19**, 397 (1988).
5. E.L.V. Lewis, R.A. Duckett, I.M. Ward, J.P.A. Fairclough, and A.J. Ryan, *Polymer*, **44**, 1631 (2003)
6. O. Motta, L. Di Maio, L. Incarnato, and D. Acierno, *Polymer*, **37**, 2373 (1996)
7. V. Prattipati, Y. S. Hu, S. Bandi, D. A. Schiraldi, A. Hiltner, E. Baer, and S. Mehta, *J. Appl. Polym. Sci.*, **97**, 1361 (2005)
8. W. Wu, M.H. Wagner, Q. Qi, P. Weiguang, and S. Kheirandish, *J. Appl. Polym. Sci.*, **101**, 1309 (2006)
9. Z. Ke, and B. Yongping, *Mater. Lett.*, **59**, 3348 (2005)
10. A. Sanchez-Solis, A. Garcia-Rejon , and O. Manero, *Macromol. Sy.*, **192**, 281 (2003)
11. C. Thellen, C. Orroth, D. Froio, J. Lucciarini, J. Ratto, A. Ranade, and N.A. D'Souza, *SPE ANTEC*; 2130 (2004)
12. G.D. Barber, B.H. Calhoun, and R.B. Moore, *Polymer*, **46**, 6706 (2005)
13. C.H. Davis, L.J. Mathias, J.W. Gilman, D.A. Schiraldi, J.R. Shields, P. Trulove, T.E. Sutto, and H.C. Delong, *J. Polym. Sci. Pol. Phys.*, **40**, 2661 (2002)
14. M.C. Costache, M.J. Heidecker, E. Manias, and C.A. Wilkie, *Polym. Advan. Technol.*, **17**, 764 (2006)
15. L.S. Brandao, L.C. Mendes, M.E. Medeiros, L. Sirelli, and M.L. Dias, *J. Appl. Polym. Sci.*, **102**, 3868 (2006)
16. J.W. Chung, S.B. Son, S.W. Chun, T.J. Kang, and S.Y. Kwak, *Polym. Degrad. Stabil.*, **93**, 252 (2008)

17. J.U. Calderon, and M.R. Kamal, SPE ANTEC, 357 (2006)
18. K. Stoeffler, P.G. Lafleur, and J. Denault, SPE ANTEC, 123 (2007)
19. U. Gurmendi, J.I. Eguiazabal, and J. Nazabal, Macromol. Mater. Eng., **292**, 169 (2006)
20. J.U. Calderon, B. Lennox, and M.R. Kamal, Appl. Clay Sci., **40**, 90 (2008)
21. K. Stoeffler, P.G. Lafleur, and J. Denault, Polym. Eng. Sci., **48**, 1449 (2008)
22. A. Vermogen, V.K. Masenelli, R. Séguéla, R.J. Duchet, S. Boucard, and P. Prele, Macromolecules, **38**, 9661 (2005)
23. R.A. Vaia, K.D. Jandt, E.J. Kramer, and E.P. Giannelis, Chem. Mater., **8**, 2628 (1996)
24. N.K. Borse, and M.R. Kamal, Polym. Eng. Sci., **46**, 1094 (2006)
25. Z.P. Luo, and J.H. Koo, J. Microsc., **225**, 118 (2007)
26. Z.P. Luo, and J.H. Koo, Polymer, **49**, 1841 (2008)
27. O. Yoshida, and M. Okamoto, Macromol. Rapid Comm., **27**, 751 (2006)
28. J.U. Calderon, and M.R. Kamal, "Evaluation of various surfactants and compatibilizers for preparation of PS/Clay nanocomposites by melt compounding", J. Polym. Eng., in press
29. A.K. Helmy, E.A. Ferreiro, and S.G. Bussetti, J. Colloid Interf. Sci., **210**, 167 (1999)
30. M.R. Kamal, J.U. Calderon, and R.B. Lennox, J. Adhes. Sci. Technol., **23**, 663 (2009)
31. L. Mandelkern, Crystallization of Polymers, McGraw-Hill, (1964)
32. G. Guan, C. Li, X. Yuan, Y. Xiao, X. Liu, and D. Zhang, J. Polym. Sci. Pol. Phys., **46**, 2380 (2008).
33. S.J. Lee, W.G. Hahm, T. Kikutani, and B.C. Kim, Polym. Eng. Sci., **49**, 317 (2009).
34. X. Xu, Y. Ding, Z. Qian, F. Wang, B. Wen, H. Zhou, S. Zhang, and M. Yang, Polym. Degrad. Stabil., **94**, 113 (2009)
35. X. Chen, H. Gong, C. Yujun, Y. Kun, D. Yeping, and Z. Hui, Polym. Test., **26**, 144 (2007)

## CHAPTER 6

### Properties of PET nanocomposite films<sup>1</sup>

Ghasemi Hesam<sup>1</sup>, Carreau Pierre J.<sup>1</sup>, Kamal Musa R.<sup>2</sup>, Tabatabaei Seyed H.<sup>1</sup>

1) CREPEC, Chemical Engineering Department, Ecole Polytechnique  
2500 Chemin Polytechnique, H3T 1J4, Montreal, Quebec, Canada

2) CREPEC, Department of Chemical Engineering, McGill University  
3610 University Street, H3A 2B2, Montreal, Quebec, Canada

#### Abstract

Polyethylene terephthalate (PET) nanocomposite films were prepared by cast extrusion followed by uniaxial stretching, using chill rolls. Transmission electron microscopy (TEM) and wide angle X-ray diffraction (WAXD) showed that the clay layers were aligned in the machine direction (MD) in the PET/clay nanocomposite (PCN) films. Differential scanning calorimetry (DSC) showed that PCN films have higher crystallinity than the neat PET films, possibly due to the nucleating role of the silicate layers. The PCN films became hazier as the clay content increased, but the film transparency remained in the acceptable range. Oxygen permeability of the PCN films decreased by 23% compared to the neat PET film. This is comparable to predictions of models proposed in the literature. Silicate incorporation brought about 20% increase in the tensile modulus, while the puncture and tear propagation resistance were reduced, due to brittleness of the PCN films. The measured modulus (1.7 GPa) was somewhat smaller than the values predicted using the Pseudo-inclusion model (2.1 GPa).

---

1. Submitted to *Polymer Engineering and Science*

## 6.1 Introduction

Polarity, high chain stiffness, close chain packing via symmetry, intermolecular bonding, and high levels of glass transition temperature, crystallinity or orientation are desirable attributes in polymer films used in barrier applications. Polyethylene terephthalate (PET) is a semi-crystalline engineering polymer that fulfills the above features to varying degrees. However, gas permeability to oxygen has been a challenge in some applications, such as soft drinks and beer. Surface modification improves the barrier properties, but the brittleness and high cost of the coated films are common shortcomings of the coating techniques [1-2].

The incorporation of layered silicate clay as an impermeable nanoparticle phase in a PET matrix is an attractive approach to enhance gas barrier properties [3]. The relatively impermeable silicate layers create a tortuous path within the polymer matrix, thus reducing gas permeability. Melt compounding and in situ polymerization are the main techniques employed to produce PET nanocomposites. Melt compounding is the preferred method for preparation of polymer nanocomposites, due to the absence of solvents and monomers, which have environmental and cost disadvantages. Furthermore, the high deformation rates employed in extrusion compounding enhance the dispersion of nanoparticles in the molten polymer matrix.

Few reports are available in the literature regarding the properties of PET/clay nanocomposite (PCN) products. A study showed that the ultimate tensile strength of PCN fibers incorporating phosphonium-modified clay increased with clay content [4]. The modulus of the prepared fibers using a capillary rheometer was approximately twice that of the neat PET fibers. Another study showed that the addition of nanoclay led to increase of drawability of PET fibers in hot air [5]. The modulus and tenacity improved at 1 wt% loading of clay, but at higher concentration, the presence of large aggregates prohibited the efficient orientation along the fiber

axis. Biaxial stretching (by a factor of 3) of PCN sheets, containing 2 wt% synthetic clay, led to an increase in the tactoid length, thus causing a ca. 20% reduction of oxygen permeability [6]. Another study showed that incorporation of 5 wt% Nanoter™ 2000 clay in PET, using a batch internal mixer caused approximately 30% reduction in oxygen permeability [7]. Compounding a bottle grade PET with ammonium modified clay led to an increase in the tensile modulus by 20% for partially intercalated PCNs [8]. A reduction of about 20% in oxygen permeability was reported for specimens prepared by compression molding.

In this work, PCN thin films (25-90  $\mu\text{m}$ ) were prepared by cast extrusion followed by stretching, using chill rolls. Thermal, optical, barrier and mechanical properties of the final film products were studied.

## **6.2 Experimental**

### **6.2.1 Materials**

Experimental grade high viscosity PET Selar PTX 295 (DuPont) and low viscosity general purpose PET 9921 (Eastman Chemical Co.) were used in this study. The complex viscosity behavior of both resins is presented in Figure 6.1. PTX295 is more viscous and exhibits more shear-thinning than PET 9921. In order to improve the processability, the two PET resins were blended at a ratio of 4:1 (low: high viscosity). The results of a study relating to the compounding of different organomodified clays and PET have been reported elsewhere [9]. Based on that study, a commercial ammonium modified clay (Cloisite 30B, Southern Clay Co.) was compounded with the PET blend (in powder form) at two different nominal levels of clay (1 and 3 wt%).

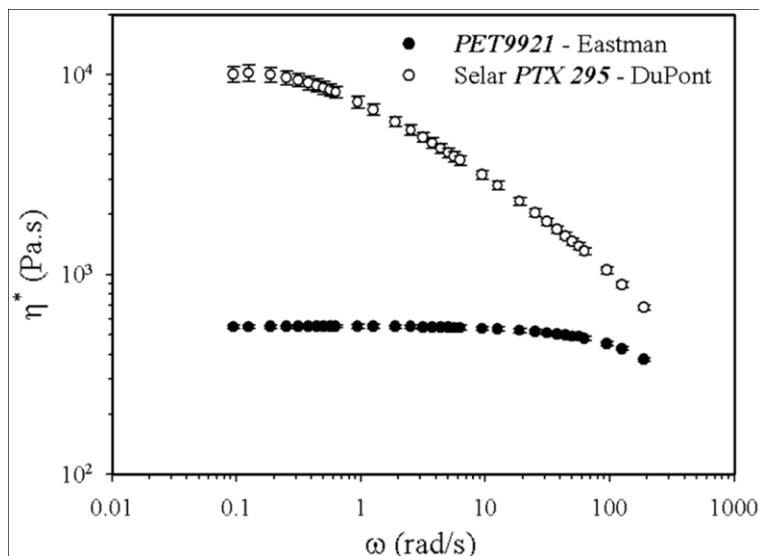


Figure 6.1: Complex viscosity of the neat polymers measured with a CSM rheometer at a stress amplitude of 200 Pa and 280 °C

## 6.2.2 Melt Compounding

Melt compounding was carried out in an intermeshing co-rotating twin screw extruder (TSE) (Werner & Pfleiderer ZSK-30). The clay was premixed with the ground PET and then fed to the extruder hopper. The TSE had 30 mm screw diameter and  $L/D$  of 40. Figure 6.2 depicts the screw configuration. After the conveying and pressuring elements, the first mixing zones with 45° right and left hand (LH) kneading blocks (KB) are located as indicated in Figure 6.2a. The second mixing zone (Figure 6.2b) includes a short 45° kneading block and the third mixing zones (Figure 6.2c) consists of 45° and 90° kneading blocks. A slit die 1.9 mm thick and 20 cm wide was used to prepare films, and an air knife was mounted on both sides of the die to supply air on the surface of the film. At low air flow rates, necking was significant and at high air flow rates, the films wrinkled and creased. Therefore, a medium air flow rate (45%), corresponding to an air velocity of 6.3 m/s was chosen. The chill rolls were employed to stretch the extrudate. The applied draw ratios varied in the range of 25-65 and the distance between the die and chill roles

was ca. 10 cm. Under these conditions, the average necking was ca. 26% which means the width of films is 15 cm, and the thickness of the films was in the range of 25-90  $\mu\text{m}$ . The extrusion was conducted at 175 rpm and temperature profile of 240, 275, 265 and 265  $^{\circ}\text{C}$  with a feeding rate of 2 kg/h. Since PET is sensitive to humidity, which has strong influence on the processing and performance properties of the products, PET and clays were dried in a vacuum oven for 24 h before processing, at 110 and 60  $^{\circ}\text{C}$ , respectively.

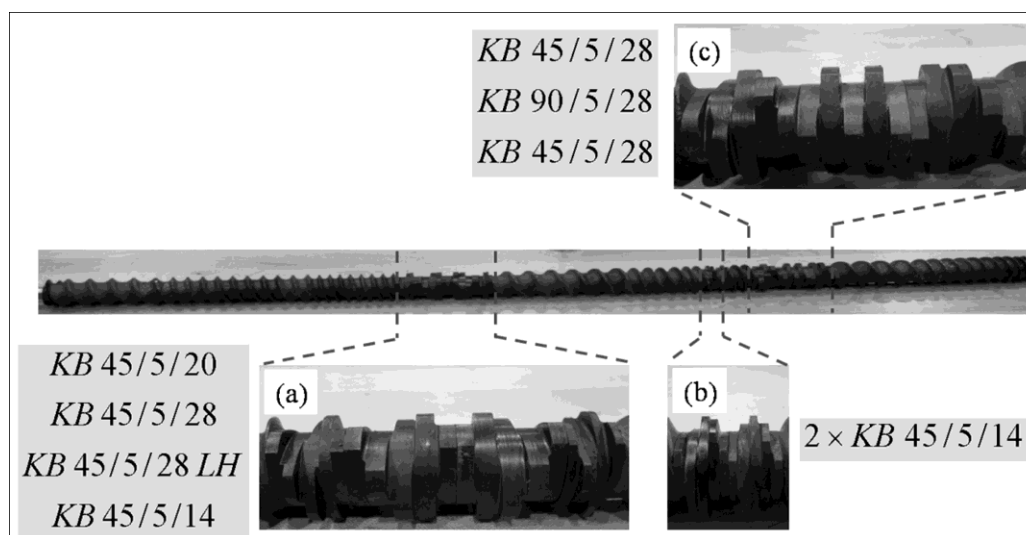


Figure 6.2: Screw configuration: a) 1<sup>st</sup> mixing zone composed of both 45 $^{\circ}$  right and left hand kneading blocks; b) 2<sup>nd</sup> mixing zone with 45 $^{\circ}$  right hand kneading blocks; and c) 3<sup>rd</sup> mixing zone including 45 $^{\circ}$  and 90 $^{\circ}$  kneading blocks. KB and LH denote kneading block and left hand, respectively. The first two numbers indicate the staggering angle and number of blocks, respectively and the third one represents the length in mm.

### 6.2.3 Characterization

The quality of the clay dispersion was evaluated using transmission electron microscopy (TEM) (JEOL JEM-2100F, Japan, operating at 200 kV). In order to study the orientation of platelets and tactoids, microtoming was done along the machine direction. To cut the specimens into

approximately 50-80 nm thick slices, they were embedded in epoxy resin and microtomed using an Ultracut FC microtome (Leica, Germany) with a diamond knife at room temperature.

XRD measurements were carried out using a Bruker AXS X-ray goniometer (USA) equipped with a Hi-STAR two-dimensional area detector. The generator was set at 40 kV and 40 mA and copper Cu K $\alpha$  radiation ( $\lambda=1.542 \text{ \AA}$ ) was selected, using a graphite crystal monochromator. The sample to detector distance was fixed at 12 cm for wide angle X-ray diffraction. To get the maximum diffraction intensity, several cast film layers were stacked together to obtain a total thickness of about 2 mm.

TEM micrographs were used to measure the average aspect ratio of dispersed clays. The micrographs were manually digitized using SigmaScan v.5 software (SPSS Inc., USA) and a digitizing tablet (Wacom, Japan).

The crystallization and the melting behavior of the PCN films were studied, using differential scanning calorimetry (DSC) (DSCQ1000 TA instruments, USA) under helium atmosphere, by scanning at 10 °C/min from 50 to 280 °C. The samples were also annealed in a vacuum oven, at 150 °C for 15-20 min, and the same DSC procedure was applied to the annealed specimens. Haze-gard plus (Qualitest International Inc., Canada) was used to measure haze and clarity of the produced films.

An Instron 5548 micro tester (USA) was used to measure tensile properties. Rectangular samples, 13 mm wide and 35 mm long, were stretched at 25 mm/min at room temperature. The tear resistance of the films was measured in both machine (MD) and transverse (TD) directions according to ASTM D1922. Rectangular samples, 7.6 cm (3 in.) in length by 6.4 cm (2.5 in.) in width, were cut and plainly marked to denote the intended direction of tear. The required work for tearing was measured based on the angular position of the pendulum during the tearing operation. Puncture tests were performed using a 100 N load cell of an Instron 5500R (USA).

The samples were pierced by a needle with 0.5 mm radius and 25 mm/min speed. The displacement of the film was recorded against the force (N) and the maximum force was reported as the puncture strength.

Oxygen transmission rates (OTRs) were determined using an Ox-Tran Model 2/21 oxygen permeability MD Module from Mocon (USA) at 23 °C. The 100% dry oxygen test gas concentration was used as the driving force and all the tests were done under barometric pressure 700 mmHg. According to the definition, to obtain the permeability coefficient, all measured OTR values have been normalized (multiplied) by the films thickness.

## **6.3 Results and discussion**

### **6.3.1 Morphology**

TEM micrographs of PCN films containing 3 wt% Cloisite 30B (C30B) prepared at the largest draw ratio (65) show a partially exfoliated/intercalated structure with dispersed tactoids (Figure 6.3). The individual delaminated silicate layers, observed at higher magnification, reflect the compatibility and surface interactions between PET chains and the hydroxyl groups of C30B, which facilitate the separation of the silicate layers. At the same time, thermal stability of surfactant is a concern in PCNs processing. This degradation might contribute to the presence of the dispersed tactoids, seen at lower magnification [9]. WAXD patterns (MN plane, Figure 6.4a) of PCN films reveal that the silicate layers are laid in the flow direction, which is in agreement with direct observation by TEM. The incident beam, which strikes the surface of the film (MT plane, Figure 6.4b), is parallel to the normal vector of the silicate layers and accordingly no pattern is observed. It can be better shown when the intensity is plotted as a function of the azimuthal angle (Figure 6.5a).

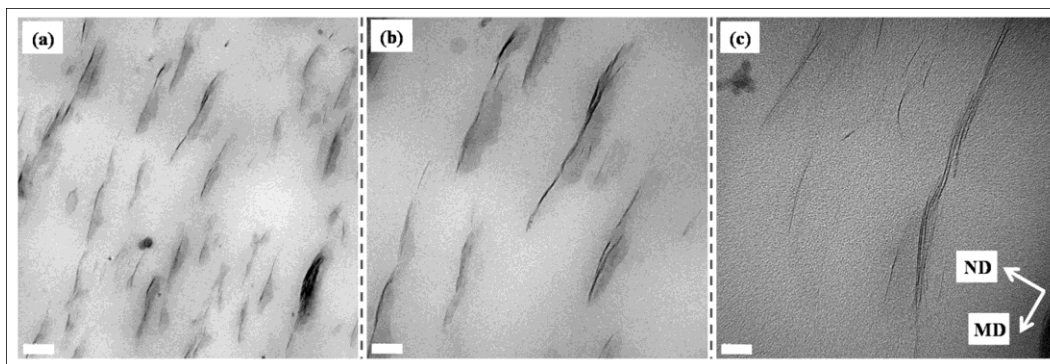


Figure 6.3: TEM micrographs of PCN films containing 3% C30B at the largest draw ratio (65) MD and ND denote machine and normal direction, respectively. The scale bars represent a) 0.2  $\mu\text{m}$ ; b) 100 nm; and c) 20 nm.

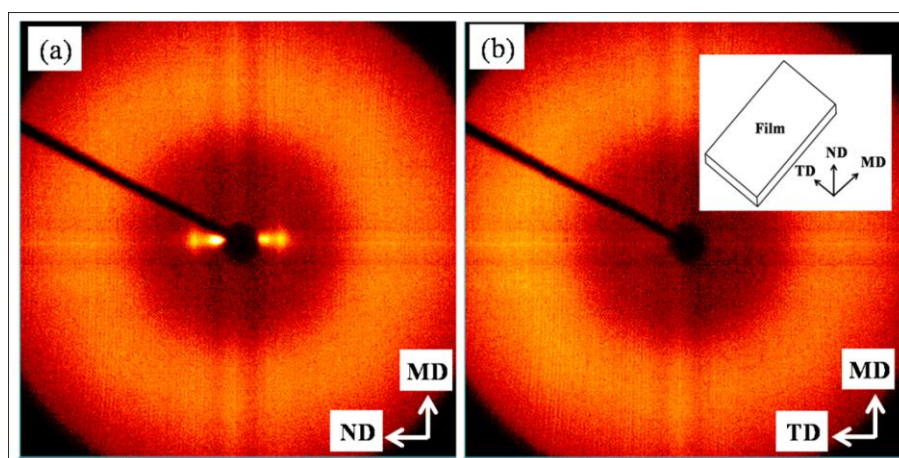


Figure 6.4: 2-D WAXD patterns of PCN films containing 1% C30B at the largest draw ratio (65) in: a) MN; and b) MT plane The insert depicts the observed planes.

The azimuthal angle,  $\phi$ , is 0 or 180° along the equator and 90 or 270° along the meridian. The noticeable peak at the azimuthal angle of 0° is another proof that the silicate layers are oriented in the flow direction. The diffraction intensity profiles (Figure 6.5b) of PCN films with C30B show two distinct diffractions corresponding to the delamination state of silicate layers [9]. The first peak ( $d$ -spacing~3.5 nm) is related to the intercalated morphology. The second peak ( $d$ -

spacing~1.6 nm), which appears at lower  $2\theta$ , could be related to the degradation of the modifier. Figure 6.6 compares the azimuthal intensity profiles of PCN films at the lowest and largest draw ratios. The full width at half maximum (FWHM) is a criterion for the orientation level. FWHM of the PCN films at a draw ratio of 65 is slightly lower than that at a draw ratio of 25. It demonstrates that in cast film extrusion owing to the stretching at the exit of the slit die, most of the silicate layers are in MD and increasing the draw ratio has no significant effect on the state of orientation of the clays

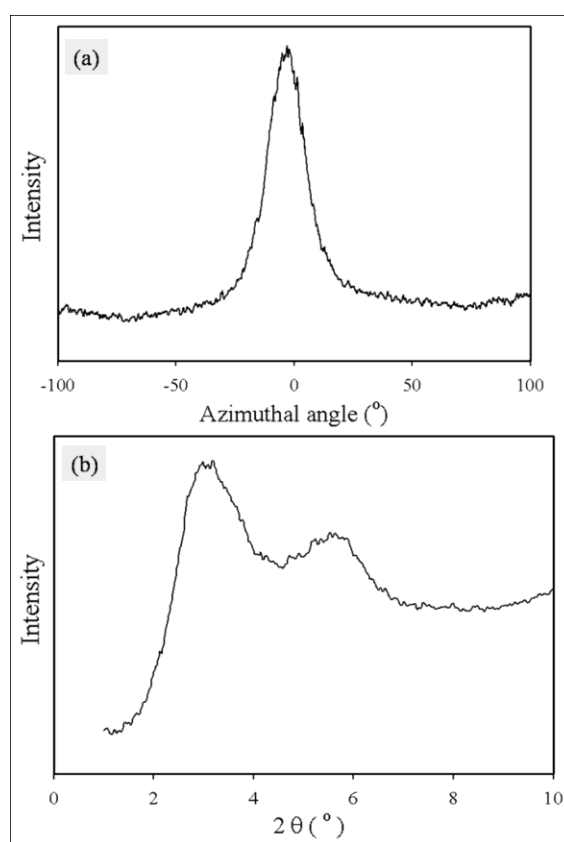


Figure 6.5: a) Azimuthal intensity profile; and b) Diffraction spectrum of PCN films with 1% C30B at the largest draw ratio (65) in MN plane

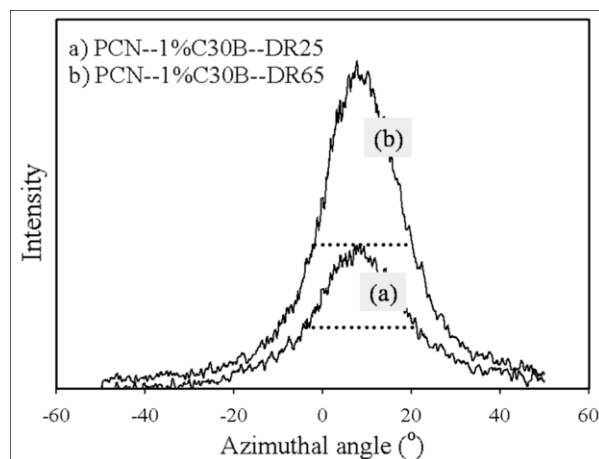


Figure 6.6: Azimuthal intensity profiles of PCN films containing 1% C30B at a) the smallest (25); and b) largest (65) draw ratios in MN plane

### 6.3.2 Crystallization Behavior

DSC measurements were carried out at 10 °C/min from 50 to 280°C. Samples were also annealed at 150 °C for 15-20 min, and the same procedure was applied to the annealed specimens. The results are presented in Figure 6.7. At a given draw ratio, the cold crystallization temperature (determined at the peak),  $T_C$ , decreases by ca. 5°C when C30B is incorporated into the neat PET, indicating that the clay acts as a nucleating agent during cold crystallization (Figure 6.7a). When crystallization takes place further below the melting region, it is controlled by growth from a kinetic point of view [10]. Thus, the presence of more nuclei in the system leads to faster rate of crystallization [11-12]. After annealing at 150 °C for 15-20 min, the cold crystallization peak disappears and a small endothermic peak is observed at 20-25 °C above the annealing temperature (Figure 6.7b). The first endothermic peak (between 170-190 °C) is due to the melting of the less perfect secondary crystals between lamellae stacks [13]. This peak shifts to higher temperature with clay content (Figure 6.7c). The second endothermic peak pertains to the melting of the primary crystals formed in the first step of the crystallization (lamella formation and three-

dimensional crystal growth) [14]. The position of the second melting point shifts by only 2 °C with clay content. The results illustrated in Figure 6.7c are almost independent of draw ratio (the difference is less than 0.5°C).

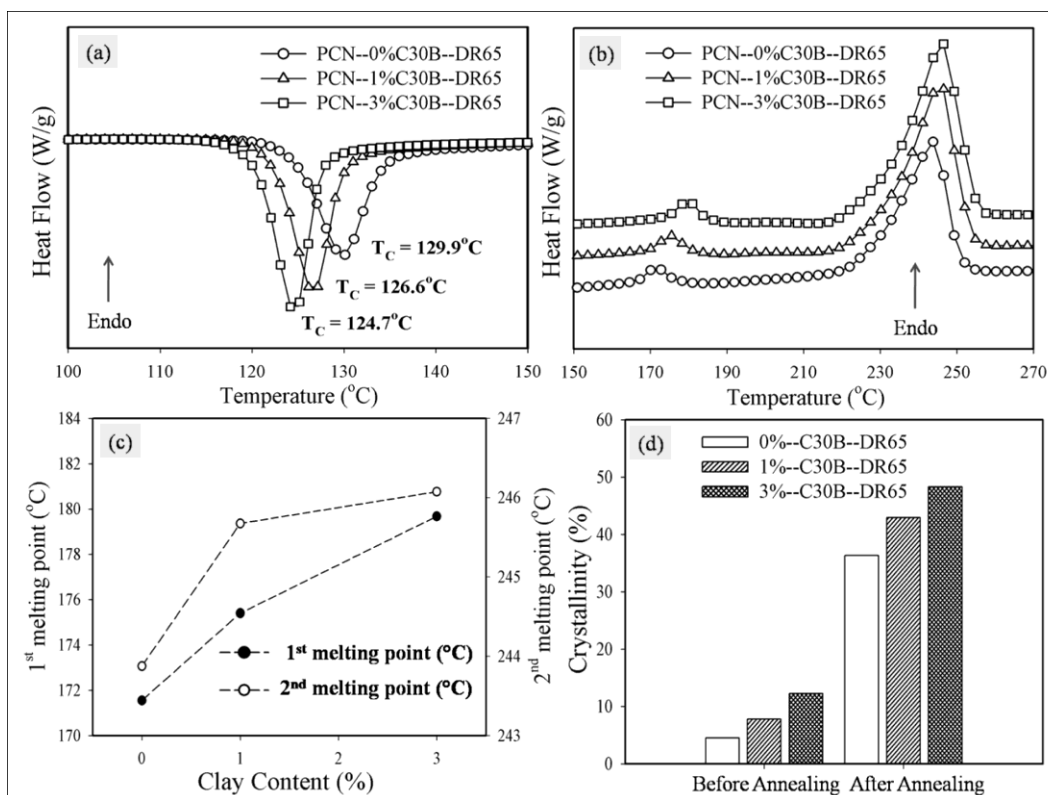


Figure 6.7: DSC results of PCN films with C30B. a) DSC traces during cold crystallization; b) DSC of annealed films; c) melting points of annealed samples vs. clay content; d) crystallinity before and after annealing

The crystallinity of the PCN films was calculated according to the following equation:

$$\text{Crystallinity}(\%) = \frac{\Delta H_m - \Delta H_{cc}}{\Delta H_0(1-x)} \quad (1)$$

where  $x$  indicates the percentage of C30B,  $m$  and  $cc$  subscripts represent melting and cold crystallization, respectively, and  $\Delta H_0$  refers to the heat of fusion of a 100% crystalline PET, which is 115 J/g [15]. As shown in Figure 6.7d, the crystallinity at a given draw ratio increases

by a factor larger than 2 for the PCN incorporating 3 wt% C30B. The above equation was also used to measure the crystallinity of the annealed samples. In this case, the cold crystallization enthalpy was omitted from the numerator and the melting enthalpy was considered as the sum of areas under the endothermic peaks. Annealing had a substantial influence on the degree of crystallinity, as shown in Figure 6.7d. The degree of crystallinity is enhanced by ca. 7, 5 and 4 times for the PCN without and with 1 and 3 wt% C30B, respectively. The presence of silicate layers enhances the crystallinity in both annealed and non-annealed samples. The crystallinity of non-annealed samples represents the amount of crystallinity induced during the cast extrusion process.

WAXD patterns of PCN films with 3% C30B before and after annealing are seen in Figure 6.8. The rings that appear after annealing are related to the crystalline reflections of PET. The diffraction spectra confirm the DSC results. The increase of area under the peak in Figure 6.9 shows that the silicate layers provide more sites for crystallization.

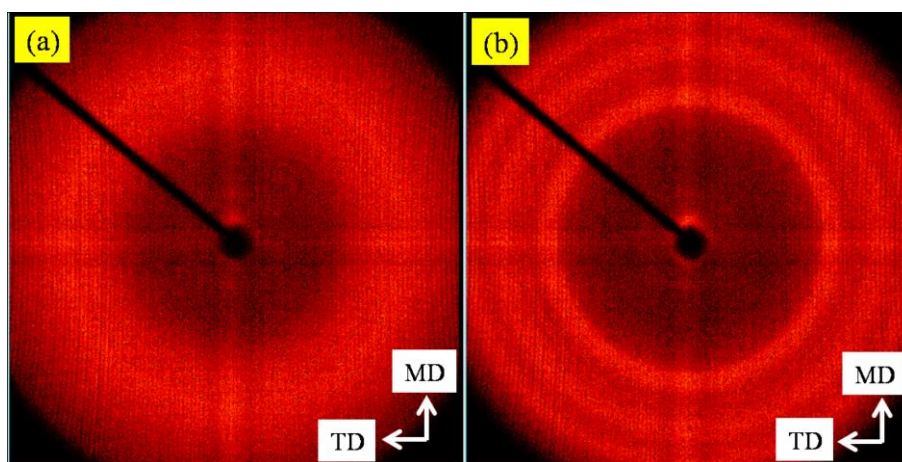


Figure 6.8: 2-D WAXD patterns of PCN films with 3% C30B at the largest draw ratio (65). a) before; and b) after annealing

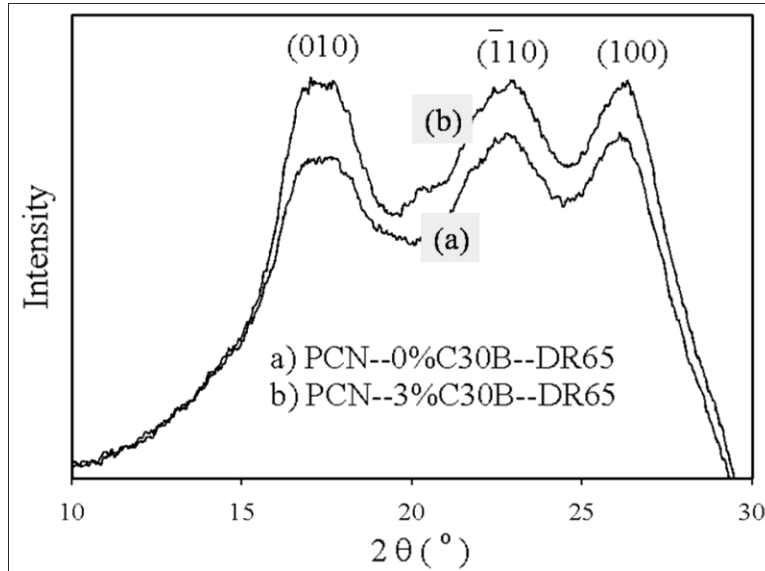


Figure 6.9: Diffraction spectrum of PCN films after annealing: a) neat PET; and b) PCN with 3% C30B

### 6.3.3 Optical Properties

Haze is defined as the fraction of transmitted light, which scatters and deviates more than  $2.5^\circ$  from the axis of the incident light [16]:

$$\text{Haze}(\%) = \frac{I_{S > 2.5^\circ}}{I_S + I_R} \times 100 \quad (2)$$

where  $I_r$  and  $I_s$  represent the regular transmitted and scattered transmitted light intensity, respectively. High haze values indicate that an object will appear milky or cloudy, when viewed through the film. Clarity or transparency is the fraction of incident light  $I_0$  that scatters by less than  $0.1^\circ$  while passing through a film [16]:

$$\text{Clarity}(\%) = \frac{I_{r < 0.1^\circ}}{I_0} \times 100 \quad (3)$$

High clarity values are associated with a clear and sharp image of an object viewed through the film. If the clarity decreases, an object seen through the film appears out of focus and fuzzy.

Figure 6.10 shows, for PCN films obtained at a draw ratio of 65, that the presence of silicate

layers reduces the clarity and increases haze, as expected for the case of incomplete exfoliation. At the highest draw ratio, the thinnest sample, the haze increased by a factor of 9 for the PCN with 3 wt% C30B, and clarity decreased by 15%. These effects are reinforced by the increased crystallinity of the polymer and the samples became completely opaque and white after annealing. Since the haze and clarity values for the PCNs are less than 6% and more than 85%, respectively, the transparency of the PCN films could be considered acceptable (ASTM D1003). Similar behavior was observed for other draw ratios (results not shown). Needless to say, the optical properties of a film depend on thickness and the haze values slightly decrease at higher draw ratio (reduction in thickness) for both neat PET and PCN films.

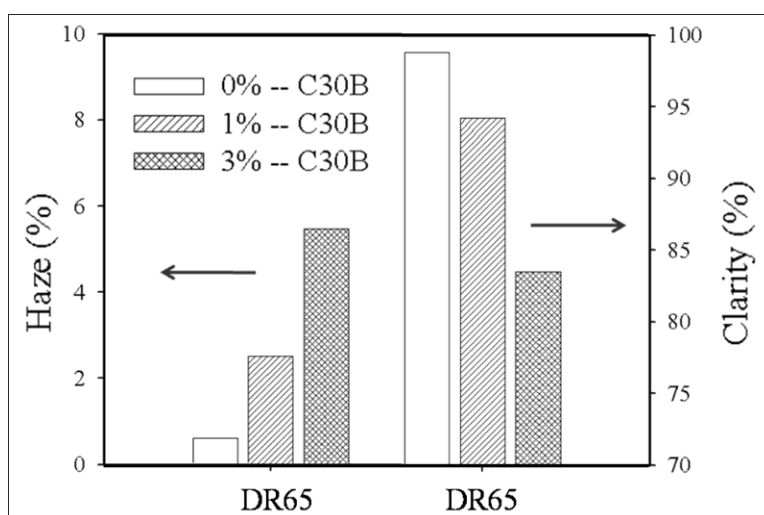


Figure 6.10: Haze and clarity of PCN films with C30B at the largest draw ratio (65)

### 6.3.4 Oxygen Permeability

In the steady-state conditions, the permeability coefficient is defined as “the volume of vapor passing per unit time through unit area of a polymer film having unit thickness with a unit pressure difference across the sample” [17]. Mathematically, the permeability coefficient ( $P$ ) is the product of the diffusivity ( $D$ ) and the solubility coefficient ( $S$ ), i.e.:

$$P = D S \quad (4)$$

By ignoring the effect of filler on the surrounding polymer matrix, the composite solubility coefficient can be described as [18]:

$$S = S_0 (1 - \phi) \quad (5)$$

where  $S_0$  is the solubility coefficient of the neat polymer and  $\phi$  is the volume fraction of the dispersed particles. In fact, the impermeable silicate layers create a tortuous path in the polymer matrix and, as a consequence, gas molecules penetrate with more difficulty. Hence, according to the above equations, the relative permeability can be obtained as a function of volume fraction of silicate layers and tortuosity ( $\tau$ )

$$K = \frac{P}{P_0} = \frac{(1 - \phi)}{\tau} \quad \text{where} \quad \tau = \frac{D_0}{D} \quad (6)$$

where 0 subscript indicates the neat polymer. Several attempts, including analytical and numerical modeling, have been made to predict the tortuosity parameter and permeability of filled systems [19-33]. The main models are summarized in Table 6.1.

The measured oxygen permeability values of the PCN films at different draw ratios are shown in Figure 6.11a. As seen, the draw ratio does not have a significant effect on the barrier properties of the products. At a 3 nominal wt% C30B, 23 % reduction in oxygen permeability was obtained, which is to be expected, according to the morphology studies (see Figure 6.3). Figure 6.11b shows that after 20 min annealing at 150 °C, the oxygen permeability of the neat PET and the PCN films at the same draw ratio (65) decrease by ca. 40 and 46%, respectively. Besides the tortuosity, chain segment immobility due to confined environmental geometry should be taken into account [34].

After annealing (see Figure 6.7d), crystal lamellas introduce more confinement and entropic penalty into the matrix, which leads to less chain mobility and reduction of permeation. In other

words, along with the effect of silicate layers, the low permeability of the crystalline phase compared to the amorphous phase indicates a complementary approach for reducing gas permeation through matrix. The volume fraction of the clay in the PCNs can be calculated as:

$$\phi = \frac{wt\% \text{ clay}}{100} \times \frac{\rho_{PCN}}{\rho_{clay}} \quad \text{where} \quad \rho_{PCN} = \frac{100}{\frac{wt\% \text{ clay}}{\rho_{clay}} + \frac{100 - wt\% \text{ clay}}{\rho_{matrix}}} \quad (7)$$

where  $\rho$  represents the density. The reported density of Cloisite Na<sup>+</sup> (natural montmorillonite) (2.86 g/mL [35]) and the measured density of the neat PET (1.27 g/mL) were used in this study.

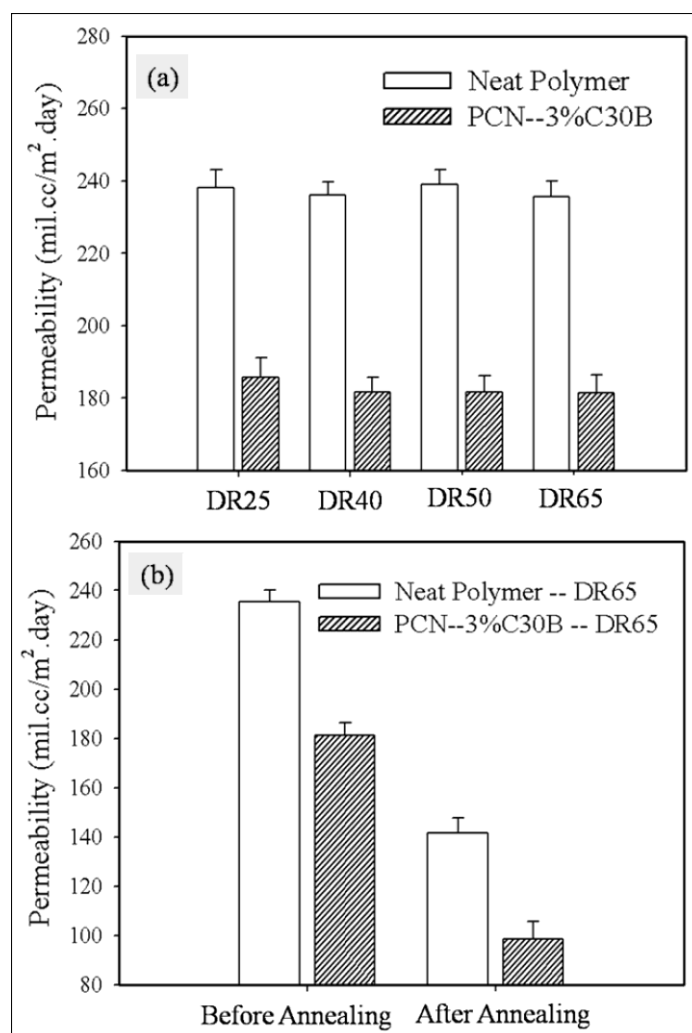


Figure 6.11: a) Oxygen permeability of PCN films vs. draw ratio; and b) Effect of crystallization on barrier properties of PCN films with C30B at the largest draw ratio (65)

The density of neat PET was determined using a HAAKE PVT100. The specific volume was measured at high pressures and extrapolated to the atmospheric pressure. The measured ash content is a reliable representative of the silicate layer content in the system. A known amount of sample (few grams) was put in the furnace and the organic material was burned at high temperature ( $\sim 800$  °C), overnight. The difference between the weight of the sample before and after burning depicts the inorganic content. C30B per se has 30% organic surfactant, which means for the PCN with 3 (nominal) wt% C30B, the expected ash content should be 2.1%. However, the measured ash content was 1.83%, probably due to loss of clay during feeding in the extruder hopper. This corresponds to a volume fraction of the silicate layers of  $\phi=0.009$  in the PCN. Based on the experimental reported percolation threshold for permeability of PCNs [36-37], and predicted value obtained by renormalization group model [38], the aspect ratio ( $\alpha$ ) of the silicate layers was assumed to be 150. The predicted relative permeability values obtained by various models are summarized in Table 6.1. As seen, the relative permeability decreases as the geometric factor  $\mu$  of the Cussler model [26] increases. The predictions of the Nielson [21] (analytical) and the Gusev [32] (numerical) model are close to our experimental value. In our PNC films, the silicate layers are oriented in MD (see Figure 6.4). Thus, the order parameter ( $O$ ) in the Bharadwaj model [33] can be taken as 1. It has to be mentioned that fully dispersed and oriented structure is the common assumption of the indicated models.

Since the morphology of the PCN films (see Figure 6.3) shows a partially intercalated structure, the difference between the values reported in Table 6.1 and the experimentally measured relative permeability ( $K=0.77$ ) is reasonable. Regarding the predicted values by the models of Table 6.1, one can conclude that even in the assumption of a completely exfoliated structure, the barrier properties would be at most lowered to half of the value for neat PET at this

level of clay ( $\phi=0.009$ ). TEM micrographs were used to estimate the average aspect ratio,  $\alpha$ , which is the ratio of the length ( $\ell$ ) to the thickness ( $t$ ) of clay particles as shown in Figure 6.12.

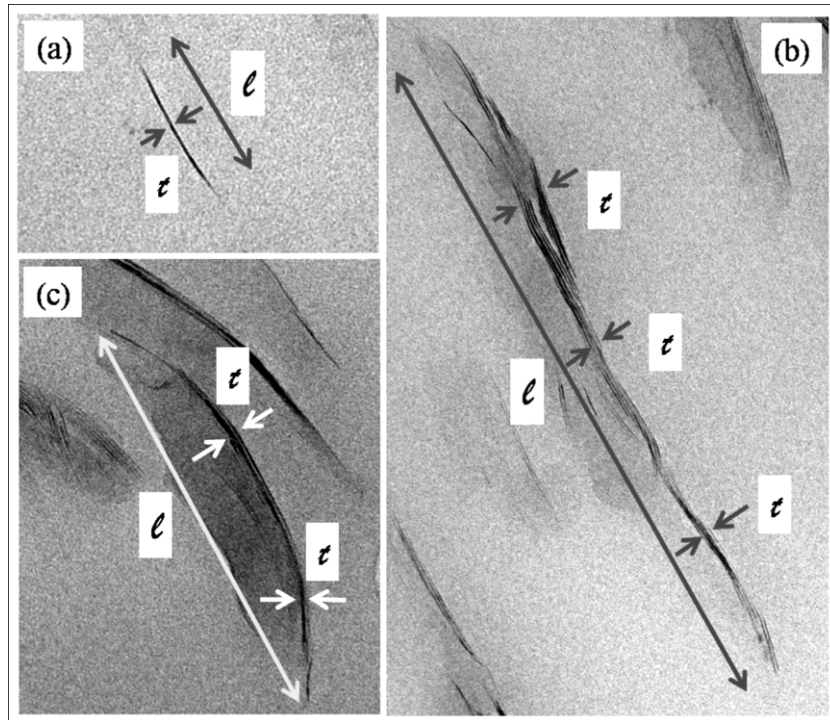


Figure 6.12: Measuring the aspect ratio of the silicate layers by image analysis. Silicate layers are laid in MD

Figure 6.12a shows the case of an exfoliated particle, while the average thickness and final length were used for overlapped tactoids (Figure 6.12b) and, for the curved tactoids (Figure 6.12c), the end-to-end vector was considered to be the length. Figure 6.13 shows the histogram of the image analysis results of ca. 200 calculated ratios. These results indicate that the average aspect ratio of the silicate particles is 47. Entering the experimental relative permeability ( $K=0.77$ ) in the Nielson [21] (analytical) and the Gusev [32] (numerical) model yields aspect ratios of 63 and 55, respectively, which are in fair agreement with the value obtained by image analysis.

Table 6.1: Predicted relative permeability values for different models. ( $\phi=0.009$  &  $\alpha=150$ )

Model	tortuosity parameter ( $\tau$ )	Geometrical Assumption	Relative Permeability (K)
Nielson [21]	$1 + \frac{\alpha \phi}{2}$	Aligned ribbons with infinite length	0.59
Cussler [26] <sup>a</sup>	$1 + \frac{\mu}{4} \left[ \frac{(\alpha \phi)^2}{1 - \phi} \right]$	Aligned ribbons with infinite length ( $\mu=1$ [27])	0.68
		Ribbons with infinite length and equal probability of alignment and misalignment ( $\mu=1/2$ [28])	0.81
		Hexagonal flakes with random orientation ( $\mu=2/27$ [29])	0.96
Cussler [30]	$1 + \left( \frac{\alpha \phi}{3} \right)^2$	Monodisperse rectangular flakes with infinite length and random planar distribution	0.47
Fredrickson [31]	$4 \left[ \frac{1+x+0.125x^2}{2+x} \right]^2$ where $x = \frac{\pi \alpha \phi}{2} \ln \left( \frac{\alpha}{2} \right)$	Monodisperse oriented disks placed in a nematic structure	0.66
Gusev [32]	$\exp \left[ \left( \frac{\alpha \phi}{3.47} \right)^{0.71} \right]$	Randomly dispersed disks without overlapping	0.59
Bharadwaj [33] <sup>b</sup>	$1 + \frac{\alpha \phi}{2} \left( \frac{2}{3} \right) \left( O + \frac{1}{2} \right)$	Aligned ribbons with infinite length ( $O=1$ )	0.59
		Randomly oriented ribbons with infinite length ( $O=0$ )	0.81

a)  $\mu$  is a geometric factor, which depends on the shape of the dispersed particles

b)  $O$  is an orientation function, which depends on the angle between the normal unit vector of silicate layers and the direction of the preferred orientation.

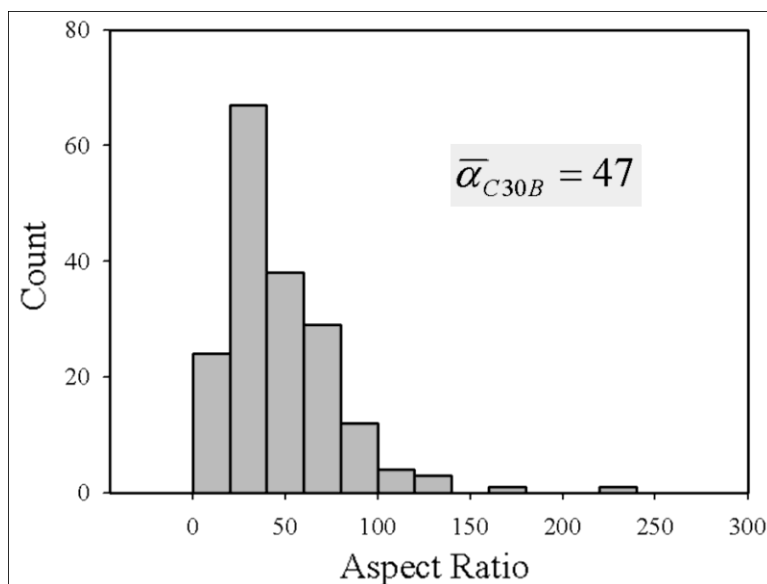


Figure 6.13: Histogram of calculated aspect ratio for PCN films with 3% C30B

### 6.3.5 Mechanical Properties

The values of the tear resistance of the PCN films at the highest draw ratio, in both MD and TD, are presented in Figure 6.14. The tear resistance decreases with clay content, in both directions. The same trend was also observed for co-extrudate multilayer nanocomposite films [39]. The resistance to tear propagation in TD is slightly higher than in MD. This might be due to the partial orientation of the PET chains in the flow direction. Tearing samples with the highest clay content obtained at low draw ratios (thicker samples) occurred along a zigzag path, leading to variable tear resistance values. Thus, the results are not reported here.

Tensile modulus in the machine direction and puncture strength of the PCN films at the highest draw ratio are shown in Figure 6.15. Clay incorporation leads to an increase of the tensile modulus and more brittleness, in comparison with the neat PET films. At 3 wt% C30B, the tensile modulus increases by around 20%, with a small increase in yield strength (data not shown). Puncture resistance is reduced by ca. 60% in comparison with the neat polymer.

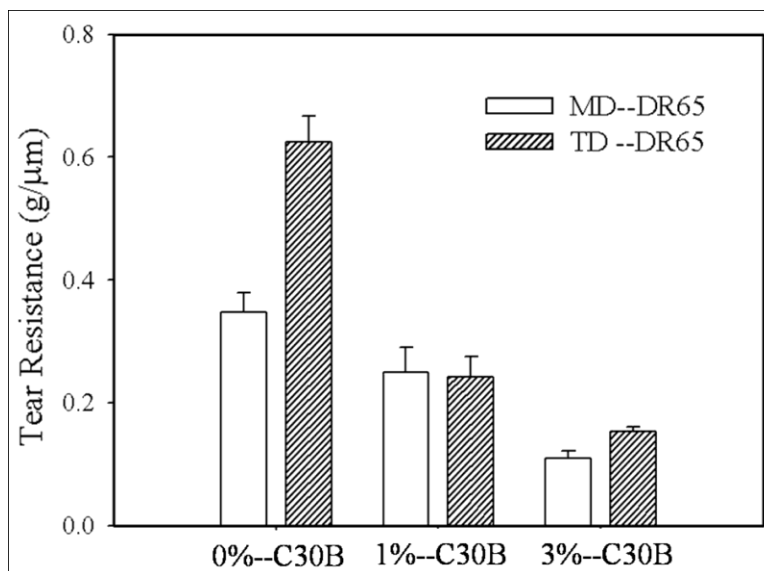


Figure 6.14: Tear resistance of PCN films in the machine (MD) and transverse (TD) directions at the largest draw ratio (65)

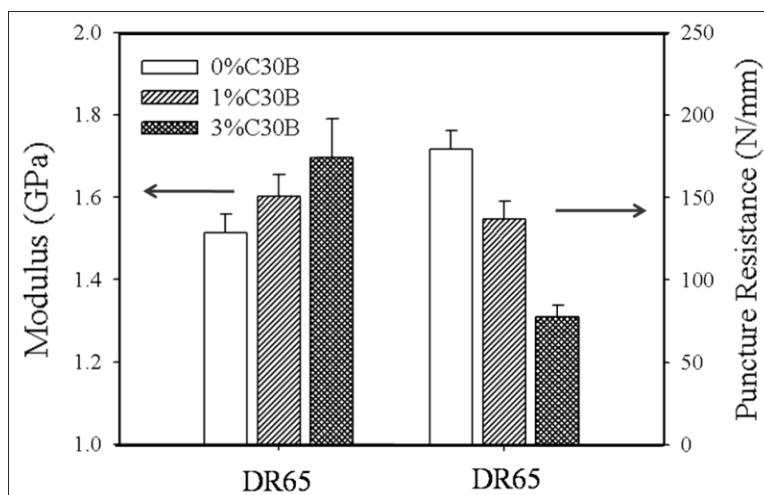


Figure 6.15: Tensile modulus in MD and puncture resistance of PCN films at the largest draw ratio (65)

It was discussed earlier that the PCNs exhibited a mix of intercalated structure and dispersed tactoids. This morphology has a significant effect on the reinforcement efficiency. A stack of platelets including organomodifier or polymer chains between clay layers can be considered as a pseudoparticle, which has a lower effective aspect ratio and higher volume fraction. Thus, a

modification of the Halpin-Tsai model [40] to account for the partially intercalated morphology leads to the Pseudo-inclusion model [41] as presented in Table 6.2. The  $d$ -spacing was determined by WAXD to be 3.5 nm (see Figure 6.5b).

Table 6.2: Halpin-Tsai and Pseudo-inclusion models

Model	Predicted Modulus
Halpin-Tsai [40]	$E = E_m \frac{1 + 2\alpha\phi\eta}{1 - \phi\eta}$ $\eta = \frac{E_r - 1}{E_r + 2\alpha}$ $E_r = \frac{E_{clay}}{E_{Matrix}}$
Pseudo-inclusion [41] <sup>a</sup>	$\hat{N} = N + (1 - N) \left( \frac{s}{t} \right) \left( \frac{\phi}{1 - \phi} \right)$ $b = 1 + \left( 1 - \frac{1}{\hat{N}} \right) \left( \frac{s}{t} \right)$ $\alpha_p = \frac{\alpha}{\hat{N}b}, \quad \phi_p = b\phi, \quad E_{rp} = \frac{E_r + 1 - b}{b}$

a)  $N$  and  $s/t$  represent the number of intercalated tactoids and gallery spacing, respectively and  $b$  is an auxiliary parameter to calculate the modified aspect ratio,  $\alpha_p$ , volume fraction,  $\phi_p$  and reduced modulus,  $E_{rp}$ . These parameters should be substituted for  $\alpha$ ,  $\phi$  and  $E_r$  in Halpin-Tsai model.

Based on the image analysis of TEM micrographs used in the preceding section, the average number of clay layers in intercalated tactoids,  $N$ , is 5. The modulus of the matrix in the longitudinal direction, measured in tensile tests (Figure 6.15), is 1.5 GPa, and the modulus of clay is 170 GPa [39]. Assuming an aspect ratio of 150, the Pseudo-inclusion model (see Table 6.2) predicts a modulus of 2.1 GPa. On the other hand, the image analysis employed in the former section gave an average aspect ratio for the silicate layers of 47. Considering the value of  $N=1$ ,

the Pseudoinclusion model becomes the classical Halpin-Tsai model (see Table 6.2), and predicts a modulus of 2.2 GPa. Both predictions are larger than the experimental modulus, 1.7 GPa. According to the Pseudo-inclusion model, a stack of platelets ( $N=5$ ) with aspect ratio of 150 would have smaller equivalent volume fraction ( $\phi_p$ ) and lower aspect ratio ( $\alpha_p$ ) than the individual layers with estimated aspect ratio of 47, which explains the discrepancy.

## 6.4 Conclusion

PCN films were prepared by cast extrusion followed by stretching, using chill rolls. TEM and WAXD were used to study the morphology and the state of delamination. The PCNs with C30B showed a partially exfoliated/intercalated structure. WAXD patterns showed that the silicate layers were oriented in MD (machine direction), which is in agreement with TEM analysis. DSC studies showed that cold crystallization of PCN films with C30B occurred at a lower temperature due to the nucleation effect of clay. The presence of clay resulted in more hazy films, but the products were still in the acceptable range of transparency. Incorporation of nominal 3 wt% C30B led to a 23% reduction in oxygen permeability, which is approximately half of the best predictions of models proposed in the literature. The PNCs exhibited about a 20% increase in tensile modulus, but the resistance to puncture and tear propagation was reduced due to brittleness of the PCN films. The measured modulus was smaller than the predictions of the Pseudo-inclusion model.

## 6.5 Acknowledgments

The authors would like to gratefully thank CREPEC member, Ms. Leelapornpisit, who prepared TEM micrographs. We also appreciate the generosity of DuPont for supplying one PET resin.

This project was jointly funded by NRC-NSERC-BDC.

## 6.6 References

1. C.P. Barker, K.H. Kochem, K.M. Revell, R.S.A. Kelly, and J.P.S. Badyal, *Thin Solid Films*, **259**, 46 (1995)
2. E. Schmachtenberg, F.R. Costa, and S. Gobel, *J. Appl. Polym. Sci.*, **99**, 1485 (2006)
3. Z. Ke, and B. Yongping, *Mater. Lett.*, **59**, 3348 (2005)
4. J.H. Chang, *Polym.-Plast. Technol.*; **47**, 791 (2008)
5. D.W. Litchfield, and D. G. Baird, *Polymer*, **49**, 5027 (2008);
6. R.S. Rajeev, J. E. Harkin, K. Soon, T. McNally, G. Menary, C.G. Armstrong, and P.J. Martin, *Eur. Polym. J.*, **45**, 332 (2009)
7. M.D. Sanchez-Garcia, E. Gimenez, and J.M. Lagaron, *Journal of Plastic Film and Sheeting*, **23**, 133 (2007)
8. M. Frounchi, and A. Dourbash, *Macromol. Mater. Eng.*, **294**, 68 (2009)
9. H. Ghasemi, P.J. Carreau, M.R. Kamal, and J.U. Calderon; "Preparation and characterization of PET/Clay nanocomposites by melt compounding"; Accepted in *Polym. Eng. Sci.* (2010)
10. J.I. Lauritzen, and J.D. Hoffman, *J. Appl. Phys.*, **44**, 4340 (1973)
11. M.R. Kamal, N.K. Borse, and A. Garcia-Rejon, *Polym. Eng. Sci.*, **42**, 1883 (2002)
12. Y. Ke, C. Long, and Z. Qi, *J. Appl. Polym. Sci.*, **71**, 1139 (1999)
13. Z.G. Wang, B.S. Hsiao, B.B. Sauer, and W.G. Kampert, *Polymer*, **40**, 4615 (1999)
14. Y. Kong, and J.N. Hay, *Polymer*, **44**, 623 (2003)
15. L. Mandelkern, *Crystallization of Polymers*, McGraw-Hill, (1964)
16. P. le Roy, *Journal of Plastic Film and Sheeting*, **9**, 173 (1993)

17. L.H. Sperling, Introduction to physical polymer science, John Wiley & Sons, (2006)
18. S. Takahashi, H.A. Goldberg, C.A. Feeney, D.P. Karim, M.Farrell, K.O'Leary, and D.R. Paul, *Polymer*, **47**, 3083 (2006)
19. J.C. Maxwell, Treatise on Electricity and Magnetism, Claredon Press, Vol.I (1881)
20. L. Raleigh, *Philos. Mag.*, **34**, 481 (1892)
21. L.E. Nielsen, *J. Macromol. Sci. A.*, **1**, 929 (1967);
22. R. Aris, *Arch. Ration. Mech. An.*, **95**, 83 (1986)
23. W.R. Falla, M. Mulski, and E.L. Cussler, *J. Membrane Sci.*, **119**, 129 (1996)
24. M. Minelli, M.G. Baschetti, and F. Doghieri, *J. Membrane Sci.*, **327**, 208 (2009)
25. C. Swannack, C. Cox, A. Liakos, and D. Hirt, *J. Membrane Sci.*, **263**, 47 (2005)
26. E.L. Cussler, S.E. Hughes, W.J. Ward, and R. Aris, *J. Membrane Sci.*, **38**, 161 (1988)
27. C. Yang, E.E. Nuxoll, and E.L. Cussler, *AIChE*; **47**, 295 (2001)
28. C. Yang, W.H. Smyrl, and E.L. Cussler, *J. Membrane Sci.*, **231**, 1 (2004)
29. G.D. Moggridge, N.K. Lape, C. Yang, and E.L. Cussler, *Prog. Org. Coat.*, **46**, 231 (2003)
30. N.K. Lape, E.N. Nuxoll, and E.L. Cussler, *J. Membrane Sci.*, **236**, 29 (2004)
31. G.H. Fredrickson, and J. Bicerano, *J. Chem. Phys.*, **110**, 2181 (1999)
32. A.A. Gusev, and H.R. Lusti, *Adv. Mater.*, **13**, 1641 (2001)
33. R.K. Bharadwaj, *Macromolecules*, **34**, 9189 (2001)
34. B. Xu, Q. Zheng, Y. Song, and Y. Shanguan, *Polymer*, **47**, 2904 (2006)
35. <http://www.scprod.com/msds.asp>
36. K. Yano, A. Usuki, and A. Okada, *J. Polym. Sci. A1*, **35**, 2289 (1997)
37. S.S. Ray, K. Okamoto, and M. Okamoto, *Macromolecules*, **36**, 2355 (2003)
38. C. Lu, and Y.W. Mai, *Phys. Rev. Lett.*, **95**, 1 (2005)
39. C. Thellen, S. Schirmer, J. A. Ratto, B. Finnigan, and D. Schmidt, *J. Membrane Sci.*, **340**, 45

(2009)

40. J.C. Halpin, and J.L. Kardos, Polym. Eng. Sci., **16**, 344 (1976)
41. D.A. Brune, and J. Bicerano, Polymer, **43**, 369 (2002)
42. D. Shia, C.Y. Hui, S. D. Burnside, and E.P. Giannelis, Polym. Composite., **19**, 608 (1998)

## CHAPTER 7

# Effect of processing conditions on properties of PET/clay nanocomposite films<sup>1</sup>

Ghasemi Hesam<sup>1</sup>, Carreau Pierre J.<sup>1</sup>, Kamal Musa R.<sup>2</sup>, Chapleau Nathalie<sup>3</sup>

1) CREPEC, Chemical Engineering Department, Ecole Polytechnique  
C.P. 6079 SUC. CENTRE-VILLE, H3T 1J4, Montreal, Quebec, Canada

2) CREPEC, Department of Chemical Engineering, McGill University  
3610 University Street, H3A 2B2, Montreal, Quebec, Canada

3) CREPEC, Industrial Materials Institute, National Research Council Canada,  
75 de Mortagne Blvd., J4B 6Y4, Boucherville, Quebec, Canada

### Abstract

Polyethylene terephthalate (PET) nanocomposite films (with 3 wt% Cloisite 30B) were prepared by cast extrusion followed by uniaxial stretching, using chill rolls. Two screw profiles with different mixing elements under different screw speed ( $N$ ) and feeding rate ( $Q$ ) were used to prepare PET/clay nanocomposite (PCN) films. Transmission electron microscopy (TEM) and wide angle X-ray diffraction (WAXD) showed that the clay layers were aligned in the machine direction (MD). XRD patterns depicted that the interlayer distance of clay platelets in the state of intercalation is somehow independent of the processing conditions, but the macro-scale characterization, including barrier and mechanical properties, showed that the level of clay layer delamination was affected by processing conditions. The results reveal that the applied strain has stronger effect than residence time on the barrier and mechanical properties. At the highest screw speed ( $N=250$  rpm), 27% reduction in oxygen permeability and 30% improvement in tensile modulus were obtained for the more severe screw profile.

---

1. Accepted in *International Polymer Processing*

## 7.1 Introduction

Polyethylene terephthalate (PET) is a semi-crystalline engineering thermoplastic used widely in packaging applications. The polarity, close chain packing via symmetry, intermolecular bonding and high glass transition temperature make PET a good candidate for barrier applications. However, gas permeability to oxygen has been a challenge for some applications, such as soft drinks and beer containers. Surface modification by coating improves the barrier properties, but the brittleness and high cost of the coated films are common shortcomings of the coating techniques (Barker et al., 1995; Schmachtenberg et al., 2006). The incorporation of layered silicate clay as an impermeable nanoparticle phase in a PET matrix is an attractive approach to enhance gas barrier properties (Ke and Yongping, 2005). The relatively impermeable silicate layers create a tortuous path within the polymer matrix, thus reducing gas permeability. Melt compounding and in situ polymerization are the main techniques employed to produce PET nanocomposites. Melt compounding is the preferred method for preparation of polymer nanocomposites, due to the absence of solvents and monomers, which have environmental and cost disadvantages. Furthermore, the high deformation rates employed in extrusion compounding enhance the dispersion of nanoparticles in the molten polymer matrix. It was shown that a single screw extruder is not an effective tool to delaminate the clay layers in a polymeric matrix in comparison with a twin screw extruder (Cho and Paul, 2001).

To form a nanocomposite in melt extrusion, the stacks of clay platelets must be broken into smaller tactoids, first. Then, the polymer chains should penetrate the gallery space (Dennis et al., 2001). Strain is a key factor in breaking the clay aggregates (Lin et al., 2009), but the affinity of polymer and organo-modified clay and their polar interactions dictate the level of exfoliation (Ramirez-Vargas et al., 2009). If the compatibility between the polymer and clay is low,

processing conditions would not influence the intercalation quality of the nanocomposite (Tarapow et al., 2009).

The state of nanoclay dispersion, intercalation and/or exfoliation, in a polymeric matrix depends on several parameters, such as polymer properties (Bikiaris et al., 2006; Fornes et al., 2002a; Hotta and Paul, 2004) or the chemical structure of the organomodifier (Barber et al., 2005; Brando et al., 2006; Chung et al., 2008; Costache et al., 2006; Fornes et al., 2002b; Fornes et al., 2004; Ghasemi et al., 2010a; Gurmendi et al., 2006; Zhao et al., 2003;). While processing conditions have no significant effect on interlayer spacing or the state of intercalation (Lertwimolnun and Vergnes, 2006), they seem to influence the level of exfoliation (Davis et al., 2002; Lertwimolnun and Vergnes, 2005; Li et al., 2002; Zhu and Xanthos, 2004). It was reported that for a given screw profile, the state of delamination of clay layers depends on the screw speed (Peltola et al., 2006; Tanoue et al., 2006), feeding rate (Kim et al., 2008; Lertwimolnun and Vergnes, 2007) and temperature profile (Fasulo et al., 2004; Modesti et al., 2005). Higher screw speed and lower feeding rate lead to better delamination of clay platelets (Fasulo et al., 2004; Kim et al., 2008; Lertwimolnun and Vergnes, 2007). The former indicates the influence of higher strain rates and the latter implies the influence of longer residence time.

Properties of PET/clay nanocomposite (PCN) films reported earlier and showed that incorporation of 3 wt% Cloisite 30B (C30B) caused a 23% reduction in oxygen permeability and 20% increase in tensile modulus under a selected set of processing conditions (Ghasemi et al., 2010b). In this work, the effects of processing conditions, including screw speed, screw profile and feeding rate, on barrier and mechanical properties of PCN films were studied.

## 7.2 Experimental

### 7.2.1 Materials

In order to improve the processability, an experimental grade high viscosity PET Selar PTX 295 (DuPont) and low viscosity general purpose PET 9921 (Eastman Chemical Co.) were blended at a ratio of 4:1 (low: high viscosity). The complex viscosity behavior of both resins is presented in Figure 7.1. PTX295 is more viscous and exhibits more shear-thinning than PET 9921. Commercial ammonium modified clay (Cloisite 30B, Southern Clay Products Co.) was compounded with the PET blend (in powder form) at 3 wt% nominal level of clay.

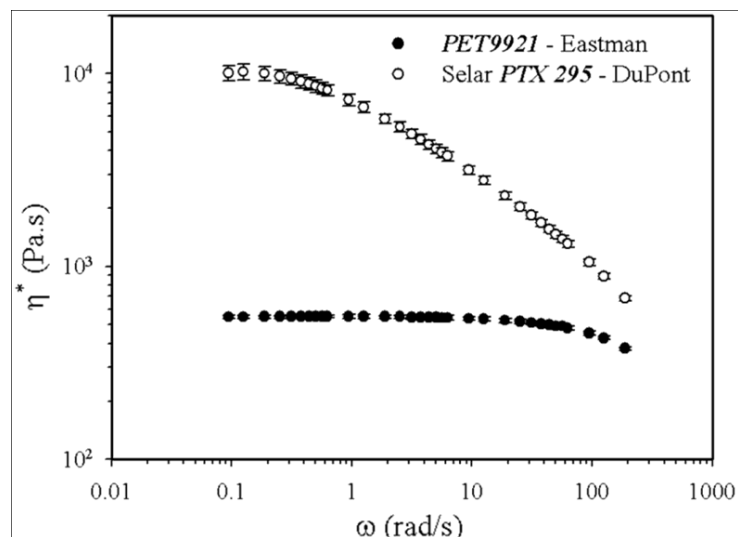


Figure 7.1: Complex viscosity of the neat polymers measured with a CSM rheometer at a stress amplitude of 200 Pa and 280 °C

### 7.2.2 Melt Compounding

Melt compounding was carried out in an intermeshing co-rotating twin screw extruder (TSE) (Leistritz, Germany). The clay was premixed with the ground PET and then fed to the extruder hopper. The diameter of the TSE screw was 34 mm and  $L/D$  was 42. Two different screw profiles

were used to prepare PCN films, and each configuration consisted of three mixing zones (Figures 7.2 and 7.3). In the first screw profile (Figure 7.2), after the conveying and pressuring elements, the first mixing zone was composed of 10 kneading elements (KS) with both positive (right handed) and negative (left handed)  $60^\circ$  staggering angle (Figure 7.2a). In KS notation, the first number indicates the number of kneading elements, the second number represents the width of each kneading lobe in mm and the third number implies the staggering angle. The positive and negative staggering angle provides forward and backward flow, respectively. The second mixing zone (Figure 7.2b) included two left (*L*) and right (*R*) handed gear type mixing elements (ZME). The first number indicates the number of teeth around the circumference, the second number represents the number of gears in each ZME block and the third number shows the length of ZME block in mm. The third mixing zone (Figure 7.2c) had 15 kneading elements with a positive  $60^\circ$  staggering angle.

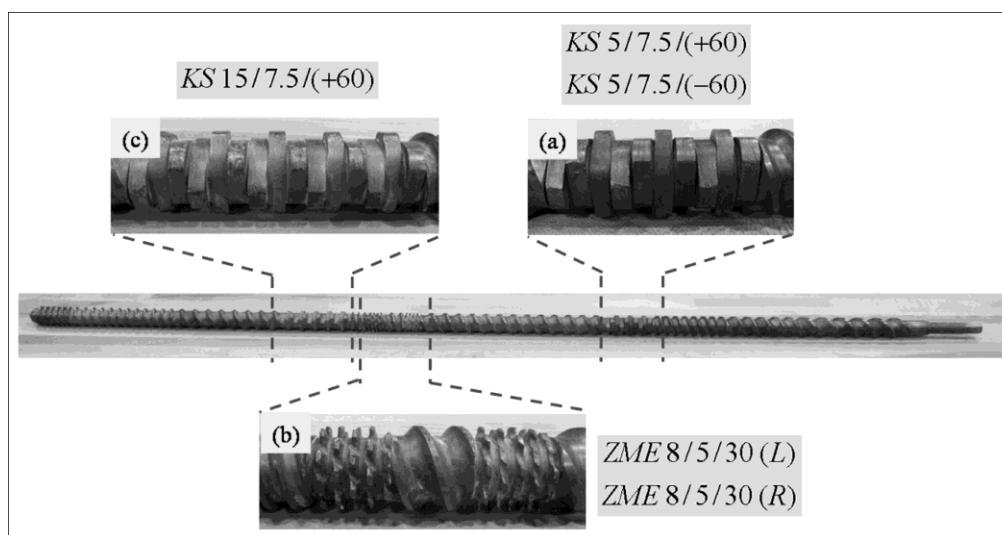


Figure 7.2: First screw profile: a) 1<sup>st</sup> mixing zone composed of 10 kneading elements with both positive (right hand) and negative (left hand)  $60^\circ$  staggering angle; b) 2<sup>nd</sup> mixing zone with two left and right hand ZME elements; and c) 3<sup>rd</sup> mixing zone including kneading elements with positive  $60^\circ$  staggering angle.

Good mixing of solid additives in molten polymers requires both dispersive and distributive mechanism (McKelvey, 1962). In dispersive mixing, the cohesion forces between solid particles should be overcome and the aggregates should be broken into smaller particles (Hartley and Parfitt, 1985). In distributive mixing, the smaller particles should be distributed uniformly in the matrix (Spencer and Wiley, 1951). Lengthening the kneading elements enhances dispersive mixing (Manas-Zloczower, 2009). In all three mixing sections of the second screw configuration (Figure 7.3), wider kneading lobes were placed first, followed by narrower kneading elements.

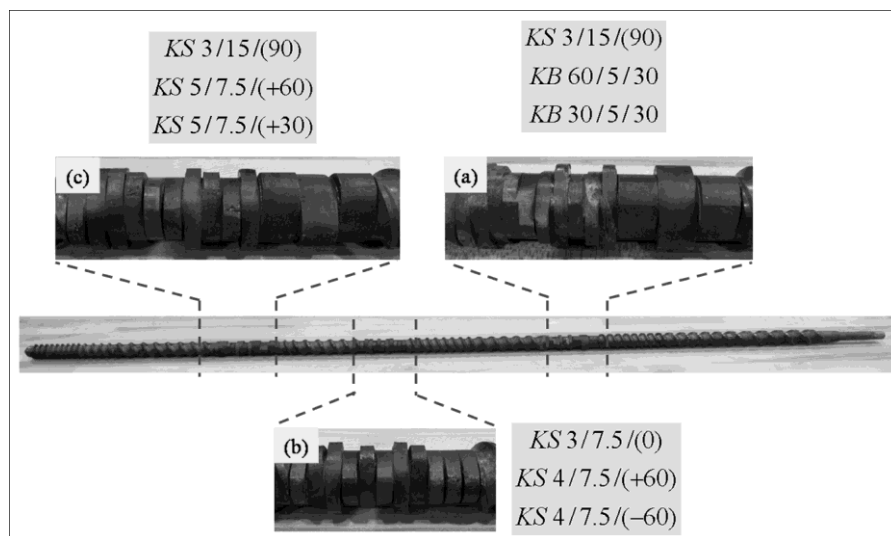


Figure 7.3: Second screw profile: a) 1<sup>st</sup> mixing zone composed of three wide kneading elements with 90° staggering angle followed by two narrow kneading blocks with 30° and 60° staggering angle; b) 2<sup>nd</sup> mixing zone with three kneading elements (0°) followed by 8 kneading elements with both positive (right hand) and negative (left hand) 60° staggering angle; and c) 3<sup>rd</sup> mixing zone including three wide kneading elements with 90° followed by 10 kneading elements with 30° and 60° staggering angle.

After the conveying and pressuring elements, three wide kneading elements with 90° staggering angle followed by two narrow kneading blocks with 30° and 60° staggering angle formed the first mixing zone (Figure 7.3a). KB denotes a kneading block. The first two numbers

indicate the staggering angle and number of lobes, respectively, and the third one represents the length in mm. The second mixing zone (Figure 7.3b) had three kneading elements ( $0^\circ$ ) followed by 8 kneading elements, with both positive and negative  $60^\circ$  staggering angle. The third mixing part (Figure 7.3c) included three wide kneading elements with  $90^\circ$  followed by 10 kneading elements with  $30^\circ$  and  $60^\circ$  staggering angle.

Table 7.1: Processing conditions and sample identification

Temperature profile from the feed throat to the die ( $^\circ\text{C}$ )														
230	275	270	265	265	265	260	260	260	260	260	260	260	260	260
First screw profile (Figure 7.2)				Second screw profile (Figure 7.3)										
Code	Sample	$N$ (rpm)	$Q$ (kg/h)	Code	Sample	$N$ (rpm)	$Q$ (kg/h)							
M1	neat PET	200	3.0	W1	neat PET	200	3.0							
M2	3%C30B	150	3.0	W2	3%C30B	150	3.0							
M3	3%C30B	200	3.0	W3	3%C30B	200	3.0							
M4	3%C30B	250	3.0	W4	3%C30B	250	3.0							
M5	3%C30B	200	1.5	W5	3%C30B	200	1.5							
M6	3%C30B	200	4.0	W6	3%C30B	200	4.0							

A 20 cm wide slit die with a 300  $\mu\text{m}$  die gap was used to prepare films, and an air knife was mounted on both sides of the die to supply air onto the surface of the film. A medium air flow rate (40% of maximum flow rate), corresponding to an air velocity of 5.2 m/s was chosen. Chill rolls ( $20^\circ\text{C}$ ) were employed to stretch the extrudate, and the distance between the die and chill rolls was ca. 10 cm. Under these conditions, the average neck-in was ca. 21%, which means the width of the films was 16 cm and their thickness was in the range of 60-80  $\mu\text{m}$ . The extrusion

was conducted at different screw speeds ( $N$ ) and feeding rates ( $Q$ ). The processing conditions and temperature profile are summarized in Table 7.1. Measurement of the ash content indicated that all PCN samples had only 1.8 wt% silicate content. The nominal ash content should be 2.1 wt%, since C30B per se has 30 wt% organomodifier, but some quantity of clay could have been lost during processing.

Since PET is sensitive to humidity, which has strong influence on the processing and performance properties of the products, the mixture of ground PET and clay were dried in a vacuum oven at 90 °C for 24 h before processing.

### 7.2.3 Characterization

The quality of the clay dispersion was evaluated using transmission electron microscopy, TEM (JEOL JEM-2100F, Japan), operating at 200 kV. In order to study the orientation of platelets and tactoids, microtoming was done along the machine direction. To cut the specimens into approximately 50-80 nm thick slices, they were first embedded in epoxy resin and microtomed using an Ultracut FC microtome (Leica, Germany) with a diamond knife at room temperature.

Wide angle X-ray diffraction, WAXD (Philips X'pert) with  $\text{CuK}\alpha$  radiation ( $\lambda=1.54056 \text{ \AA}$ ) was used to estimate the basal spacing ( $d_{001}$ ) between silicate layers. The generator was operated at 50 kV and 40 mA. The samples were scanned from 1-10° at 0.01 °/s.

X-ray diffraction (XRD) measurements were also carried out using a Bruker AXS X-ray goniometer (USA) equipped with a Hi-STAR two-dimensional area detector. The generator was set at 40 kV and 40 mA and copper Cu K $\alpha$  radiation ( $\lambda=1.542 \text{ \AA}$ ) was selected, using a graphite crystal monochromator. The sample to detector distance was fixed at 12 cm for wide angle X-ray diffraction. Several cast film layers were stacked together to obtain a total thickness of about 2 mm, in order to obtain the maximum diffraction intensity.

The crystallization and melting behavior of the PCN films were studied, using differential scanning calorimetry (DSC) (DSCQ1000 TA instruments, USA) under helium atmosphere, by scanning at 10 °C/min from 50 to 280 °C.

An Instron 5548 micro tester (USA) was used to measure tensile properties. Rectangular samples, 13 mm wide and 35 mm long, were stretched at 25 mm/min at room temperature.

Oxygen transmission rates (OTRs) were determined using an Ox-Tran Model 2/21 oxygen permeability MD Module from Mocon (USA) at 23 °C. 100% dry oxygen was used and all the tests were done under a pressure of 93.3 kPa (700 mmHg). To obtain the permeability coefficient, all measured OTR values were normalized (multiplied) by the films thickness. For each sample, the measurement was repeated three times.

## **7.3 Results and discussion**

### **7.3.1 Morphology**

XRD results obtained in the reflection mode were employed to investigate the effect of processing conditions on the state of intercalation of PCN films the results are presented in Figure 7.4. Two distinct peaks are observed for the PCN films incorporating C30B. The first (*d*-spacing~3.6 nm) reflects intercalation of the clay layers and the second (*d*-spacing~1.6 nm) implies the degradation or the exuding of the modifier. In all cases (Figure 7.4a and b), the interlayer distance of clay platelets appears around 3.6 nm. Intercalation occurs when polymer chains can diffuse into clay galleries, and it takes place rapidly in the melting zone of the barrel (Dennis et al., 2001). Thus, the level of intercalation is somehow independent of the processing conditions and screw profile (Lertwimolnun and Vergnes, 2007).

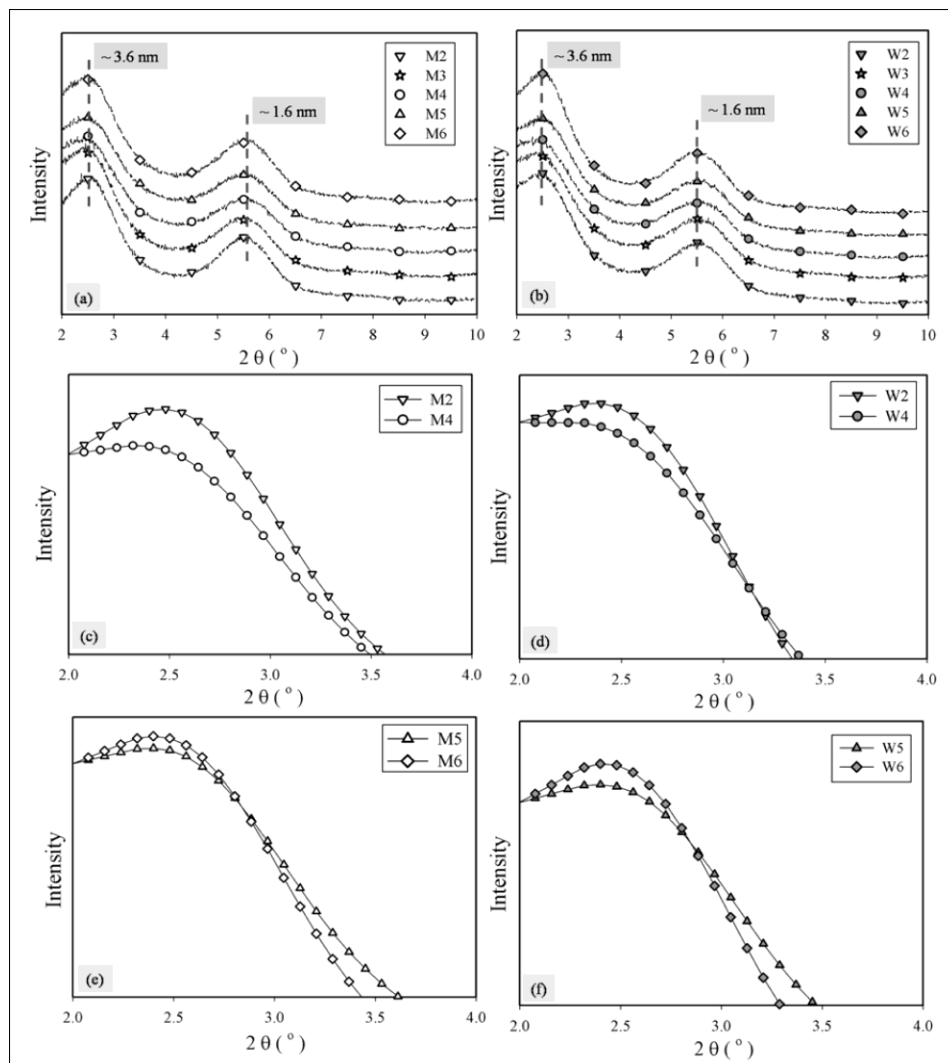


Figure 7.4: WAXD spectra of: a) PCN films prepared using the first screw profile (M series); b) PCN films prepared using the second screw configuration (W series); c): samples M2 and M4 (constant feeding rate, first screw profile); d) samples W2 and W4 (constant feeding rate, second screw profile); e) samples M5 and M6 (constant screw speed, first screw profile); and f) samples W5 and W6 (constant screw speed, second screw profile)

The development of morphology depends on how intercalated clay bundles break into tactoids during the extrusion process. However, for a given screw profile and at a fixed feeding rate ( $Q = 3$  kg/h), the height of the diffraction peak decreases when screw speed increases

(Figures 7.4c and e). A slight reduction in the intensity can also be observed by reduction of feeding rate at constant screw speed (Figures 7.4d and f). The intensity and broadness of a peak provide information regarding the number and size distribution of scattering domains, respectively (Todorov and Viana, 2007). Hence, it can be concluded that at lower feeding rate and higher screw speed, the degree of delamination is improved, due to longer residence time and applied shear, respectively.

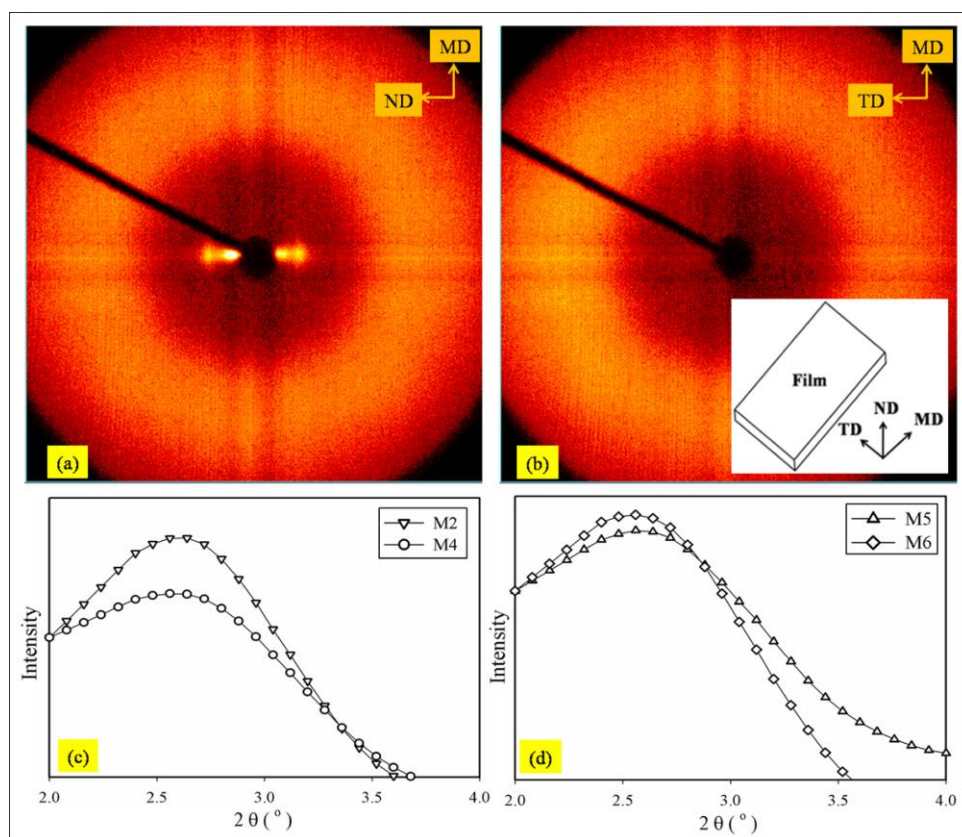


Figure 7.5: Top) Typical 2-D WAXD patterns of PCN films in a) MN; and b) MT plane; Bottom) Diffraction spectrum of PCN films prepared using the first screw profile at c) constant feeding rate; and d) constant screw speed. MD, TD and ND in the insert, represent machine, transverse and normal directions, respectively. Accordingly, the MT plane is defined by the MD and TD axes and the MN plane is specified by the MD and ND axes.

As reported earlier (Ghasemi et al., 2010b), 2D-WAXD patterns reveal that the silicate layers lie in the flow direction (Figures 7.5a and b). After integration through the patterns of MN planes, the diffraction intensity profiles, which pertain to the intensity of scattered light, are reported in Figures 7.5c and d. The results show that the XRD results in the transmission mode are in agreement with those of the reflection mode. The same trend was observed for the samples prepared by the second screw configuration (data not shown).

TEM micrographs of sample W4 (corresponding to the highest screw speed) show a partially exfoliated/intercalated structure with dispersed tactoids (Figure 7.6). The individual delaminated silicate layers, observed at the higher magnification, reflect the effect of the applied strain on the separation of the silicate layers.

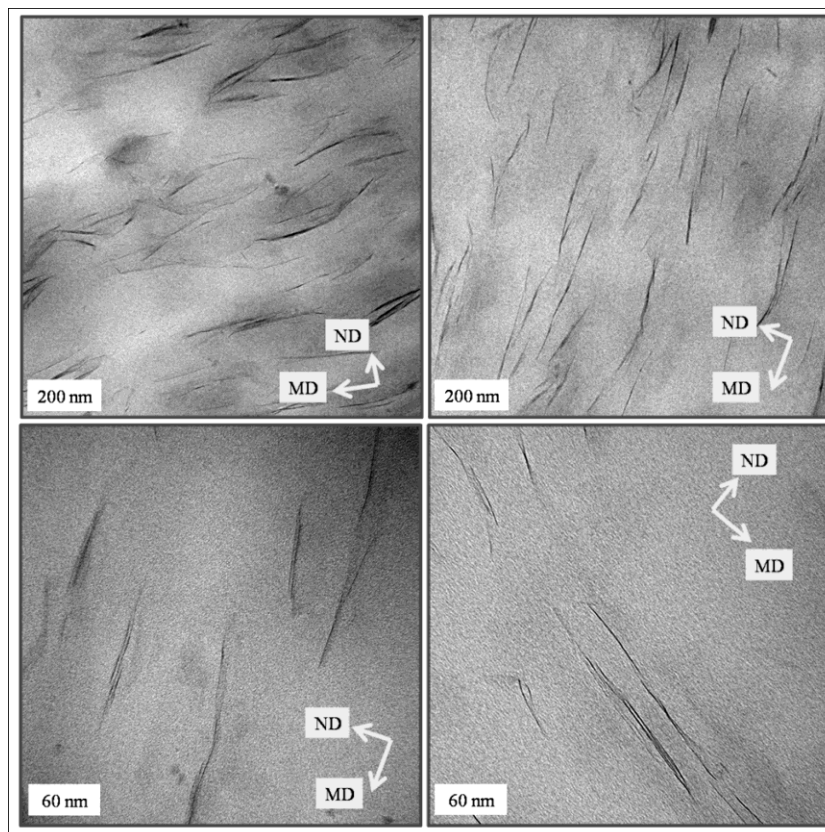


Figure 7.6: TEM micrographs of sample W4 (second screw profile, the highest screw speed) for two magnifications (top and bottom) and two different positions (left and right).

TEM results of sample W5, (the lowest feeding rate) presented in Figure 7.7 display a partially exfoliated/intercalated morphology. Since in direct observation via electron microscopy, only a small surface area is scoped out and considered as representative of the sample, macro-scale characterization was employed to shed more light on the bulk behavior of PCNs and the difference between these samples (discussed later).

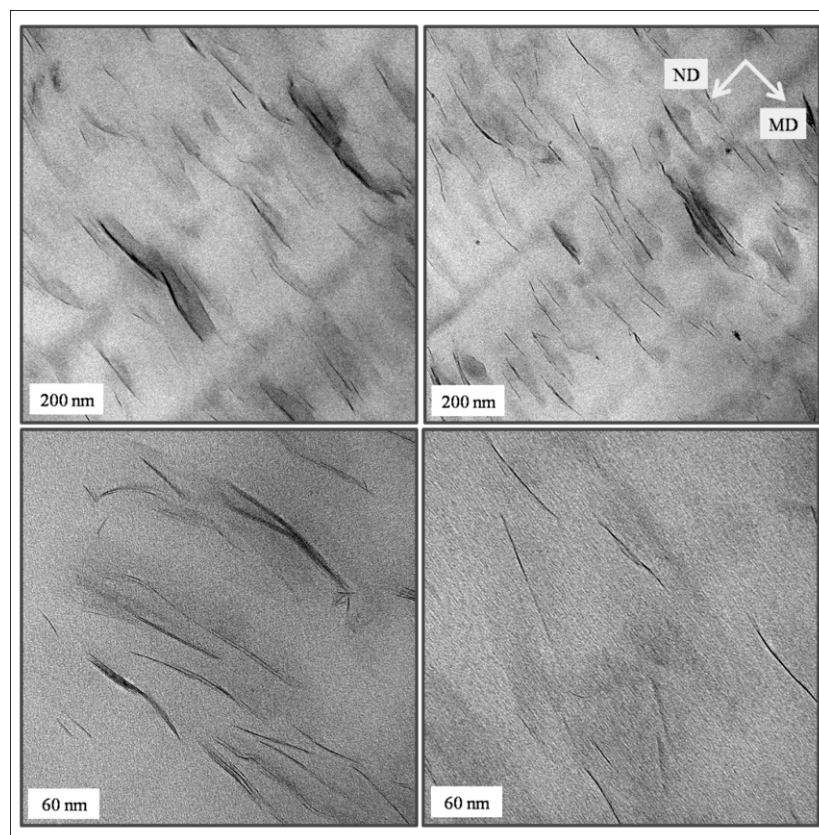


Figure 7.7: TEM micrographs of sample W5 (second screw profile, the lowest feeding rate) for two magnifications (top and bottom) and two different positions (left and right).

As shown in Figure 7.8, a big aggregate of clay can be seen in TEM micrographs of sample W6 (the largest feeding rate). It suggests that higher feeding rates and accordingly shorter residence times in the extruder barrel lead to less delamination and separation of stacks of clay platelets.

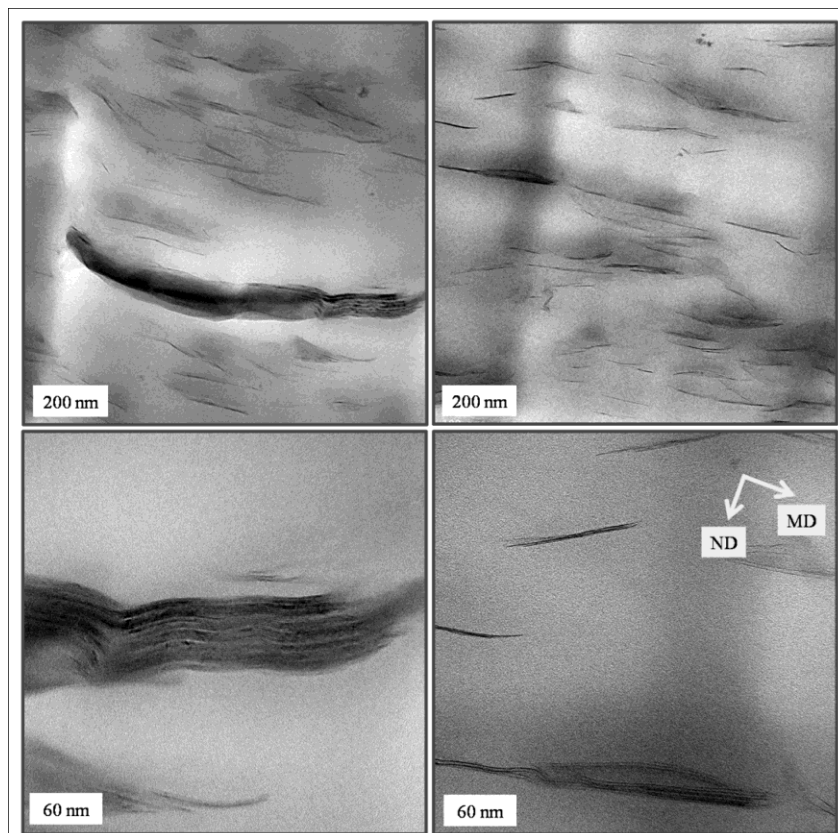


Figure 7.8: TEM micrographs of sample W6 (second screw profile, the highest feeding rate) for two magnifications (top and bottom) and two different positions (left and right).

Regardless of macro-scale characterization and based on direct observation by TEM (Figures 7.6 to 7.8), one may conclude that either higher screw speeds (higher applied strains) or lower feeding rates (longer residence time) produce partially exfoliated/intercalated morphology. More tactoids can be observed in TEM micrographs of Figure 7.9 for sample M4 (first screw profile), in comparison with sample W4 (second screw configuration), both prepared at the highest screw speed ( $N=250$  rpm).

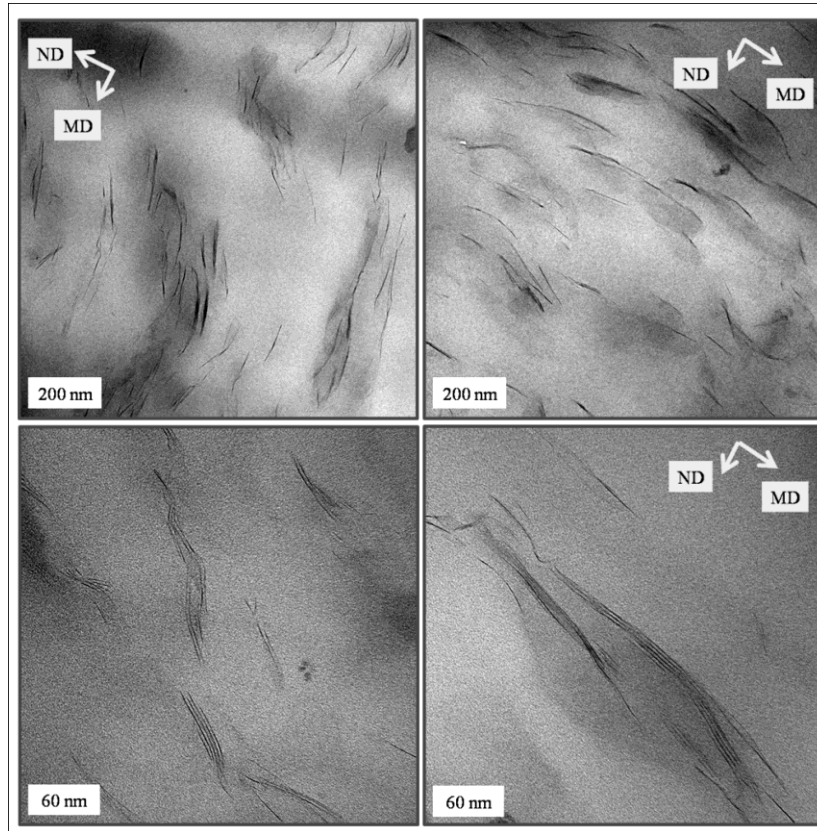


Figure 7.9: TEM micrographs of sample M4 (first screw profile, the highest screw speed) for two magnifications (top and bottom) and two different positions (left and right).

To clarify the effect of screw profile on the dispersion level of silicate layers, the free-path spacing distance (Luo and Koo, 2007; Luo and Koo, 2008) was used to provide a quantitative estimate of the degree of layer dispersion for samples M4 and W4. In this method, a random line (usually vertical or horizontal) is drawn to intercept the clay layers in a TEM micrograph. After measuring the free-path distance,  $x_i$ , between the platelets (more than 100 measurements),  $D_{0.1}$  is defined as the probability of the free-path distance distribution in the range of  $\bar{x} \pm 0.1$  (Luo and Koo, 2007):

$$D_{0.1} = 1.1539 \times 10^{-2} + 7.5933 \times 10^{-2} (\bar{x}/s) + 6.6838 \times 10^{-4} (\bar{x}/s)^2 - 1.9169 \times 10^{-4} (\bar{x}/s)^3 + 3.9201 \times 10^{-6} (\bar{x}/s)^4 \quad (1)$$

where  $\bar{x}$  and  $s$  are, respectively, the mean and standard deviation values of a set of free-path data. Values of  $D_{0.1}$  over 8% indicate an exfoliated structure, and values between 4 and 8 % indicate intercalation, while values lower than 4 % suggest an immiscible morphology (Luo and Koo, 2008). After ca. 500 measurements over 10 TEM micrographs, the value of 7.5% and 6.9% were obtained for  $D_{0.1}$  of sample W4 and M4, respectively. It seems that the incorporation of wider kneading elements followed by narrower ones in the mixing sections of the second screw profile (Figure 7.3) yields a better state of delamination of clay layers, which is supported by the enhanced mechanical properties discussed later. It is noteworthy to mention that at the highest screw speed ( $N=250$  rpm), the measured torque value of second screw was about 10% larger than the first one.

### 7.3.2 Crystallization Behavior

DSC measurements were carried out by scanning at 10 °C/min from 50 to 280 °C. At the same processing conditions (first screw profile,  $N=200$  rpm and  $Q = 3$  kg/h), the PCN films exhibit a lower cold crystallization temperature,  $T_c$ , (ca. 9 °C) than the films obtained from neat resin (Figure 7.10a). When crystallization takes place further below the melting region, it is controlled by growth from a kinetic point of view (Lauritzen, and J.D. Hoffman, 1973). Thus, generally speaking, the presence of more nuclei in the system leads to a reduction in  $T_c$ . As illustrated in Figure 7.10b,  $T_c$  for M2 is slightly higher than that of M4, which is in agreement with the WAXD results (see Figure 7.4c). The difference is clearer in the case of constant screw speed (Figure 7.10c), i.e. M5 exhibits lower  $T_c$  than M6 (2-3 °C). One may conclude that M5 (sample obtained at the lowest feeding rate) has more nuclei than other samples. On the other hand, degradation of PET in the presence of C30B is highly probable (Xu et al., 2009) and a reduction of molecular weight may contribute to a reduction in  $T_c$  (Chen et al., 2007).

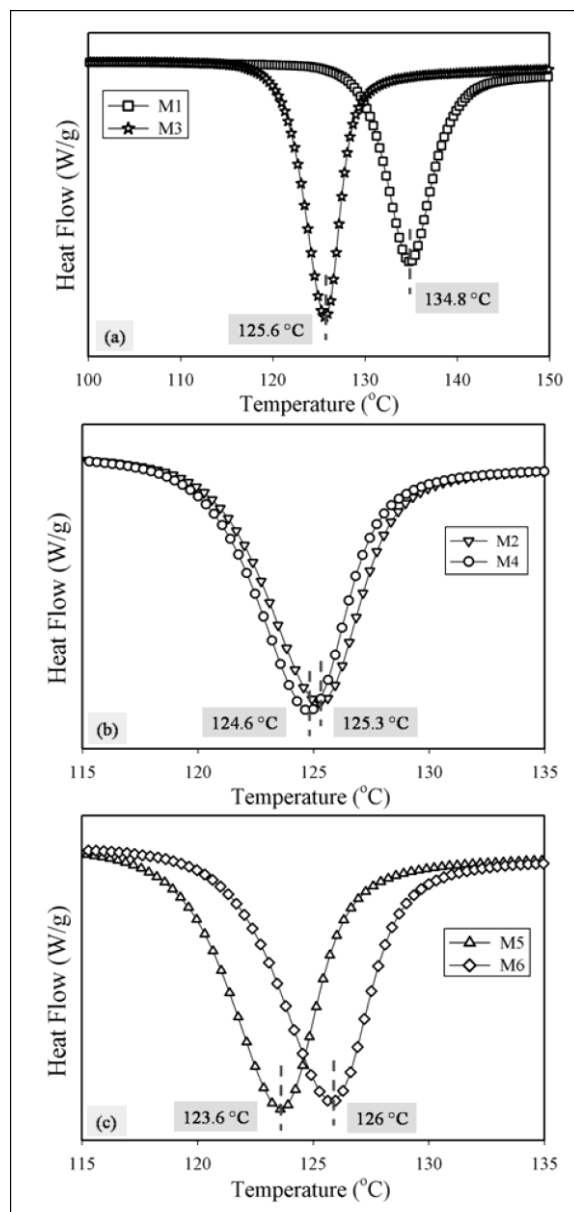


Figure 7.10: DSC results of PCN films produced using the first screw profile: a) Neat resin and PCN films prepared at  $N=200$  rpm and  $Q = 3$  kg/g; b) PCN films prepared at constant feeding rate ( $Q = 3$  kg/h). M2 and M4 are the samples prepared at 150 and 250 rpm, respectively. c) PCN films prepared at constant screw speed ( $N=200$  rpm). M5 and M6 are the samples prepared at 1.5 and 4 kg/h, respectively. The reported temperatures are the average of two experiments with the error range of  $\pm 0.2$  °C.

Hence, the lower  $T_c$  could be either related to the better state of delamination of clay platelets or to degradation of the matrix and, consequently, presence of shorter polymer chains, due to longer residence time at the lowest feeding rate. As discussed later, the mechanical properties support the latter explanation. The same trend was observed for the W series samples prepared by the second screw profile (data not shown) and the  $T_c$  values were very close to those reported above.

For both screw profiles (M and W series samples), the average crystallinity of the PCN films were 13-14%, which are ca. two times that of the neat resin (M1 and W1) and are in agreement with our previous results (Ghasemi et al., 2010b). The haze and clarity values (le Roy, 1993) of all samples were less than 5% and more than 90%, respectively, which are in the acceptable range of transparency (ASTM D1003).

### **7.3.3 Oxygen Permeability**

The measured oxygen permeability values of the PCN films are shown in Figure 7.11. As seen, the relative permeabilities are somehow independent of the screw profile. The  $K$  values ( $K=P/P_0$ ) represent the relative permeability of the samples where  $P$  and  $P_0$  are the permeabilities of the sample with and without clay, respectively. At a given screw speed and feeding rate, the  $K$  values are quite close, e.g. M3 and W3 samples show 23 and 24% reduction in oxygen permeability, respectively, which are the same as our previous findings (Ghasemi et al., 2010b). For a fixed screw profile, the lowest  $K$  (0.73) corresponds to 27% improvement of oxygen barrier properties. This result pertains to the sample prepared at the highest screw speed (M4 and W4). A comparison between the  $K$  values of the samples prepared at constant feeding rate (samples 2 and 4 in both M and W series) and constant screw speed (samples 5 and 6 in both M and W series) shows that the screw speed has a stronger effect than the feeding rate on the barrier properties.

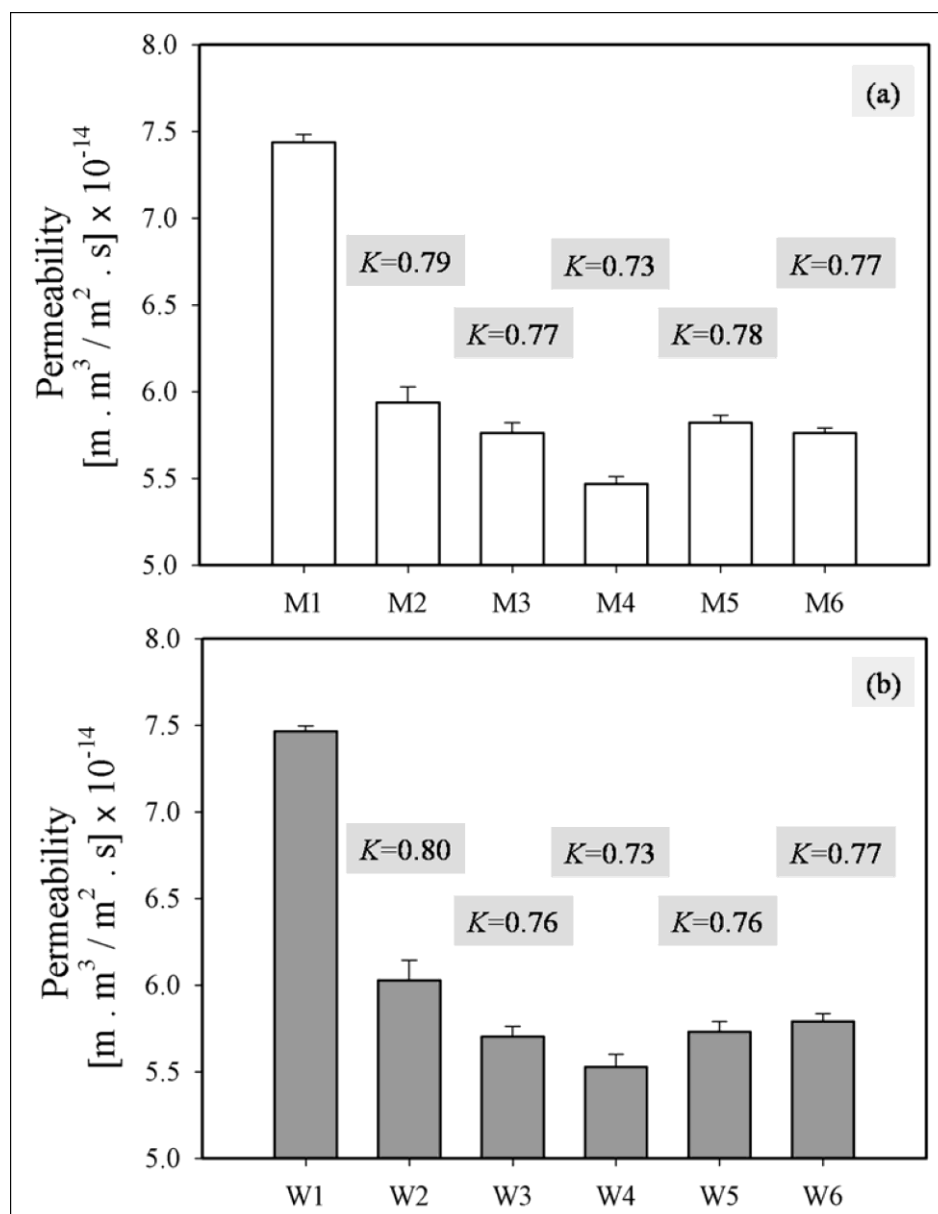


Figure 7.11: Oxygen permeability of PCN films prepared by: a) first screw profile; and b) second screw configuration. The K values ( $K=P/P_0$ ) represent the relative permeability of the samples. ( $P$  and  $P_0$  are the permeabilities of the sample with and without clay, respectively.)

C30B per se has 30% organic surfactant, which means for the PCN with 3 (nominal) wt% C30B, the expected ash content should be 2.1%. However, the measured ash content was 1.8%, probably due to loss of clay during feeding in the extruder hopper. This corresponds to a volume

fraction of the silicate layers of  $\phi=0.009$  in the PCN. Based on the experimental reported percolation threshold for permeability of PCNs (Yano et al., 1997; Ray et al., 2003), and predicted value obtained by renormalization group model (Lu and Mai, 2005), the aspect ratio ( $\alpha$ ) of the silicate layers was assumed to be 150. A comparison between the experimental data and the predictions of models were discussed earlier (Ghasemi et al., 2010b), and it was shown that the maximum achievable reduction in oxygen permeability for fully exfoliated and well-aligned silicate layers in the flow direction is ca. 40% (at 1.8 wt% silicate layer content corresponding to a volume fraction of 0.009).

### 7.3.4 Mechanical Properties

Tensile modulus data in the machine direction of the PCN films are reported in Figure 7.12. Clay incorporation leads to an increase of the tensile modulus, in comparison to the neat PET films. For all processing conditions, PCN films prepared by the second screw profile (W series) exhibit a slightly larger increase (3-4%) in tensile modulus. It might be attributed to a better dispersion of clay layers in the matrix, which was discussed above by direct observation (Figures 7.6 and 7.9) and by using  $D_{0.1}$  values. For a fixed screw profile, the largest increment is observed for the highest screw speed (sample 4), which is 26 and 30% for M4 and W4, respectively. It seems that at the lowest feeding rate (sample 5), despite the fact that the modulus increases, the longer residence time in the barrel results into more degradation of the matrix. At a constant feeding rate (samples 2-4), the tensile modulus increases gradually with screw speed, e.g. W2, W3 and W4 exhibit 23, 25 and 30% increments in modulus, respectively.

The maximum allowable displacement of the instrument gauge was 110 mm (ca. 200% tensile strain). The neat resin samples (W1 & M1) could be stretched easily after yielding up to 200%. As mentioned above, W4 shows the best results of the macro-scale characterization with

respect to barrier and mechanical properties. Figure 7.13 shows the load vs. strain curves for W1 and W4. As illustrated, the incorporation of 3 wt% C30B leads to a 75% reduction in elongation at break for sample W4.

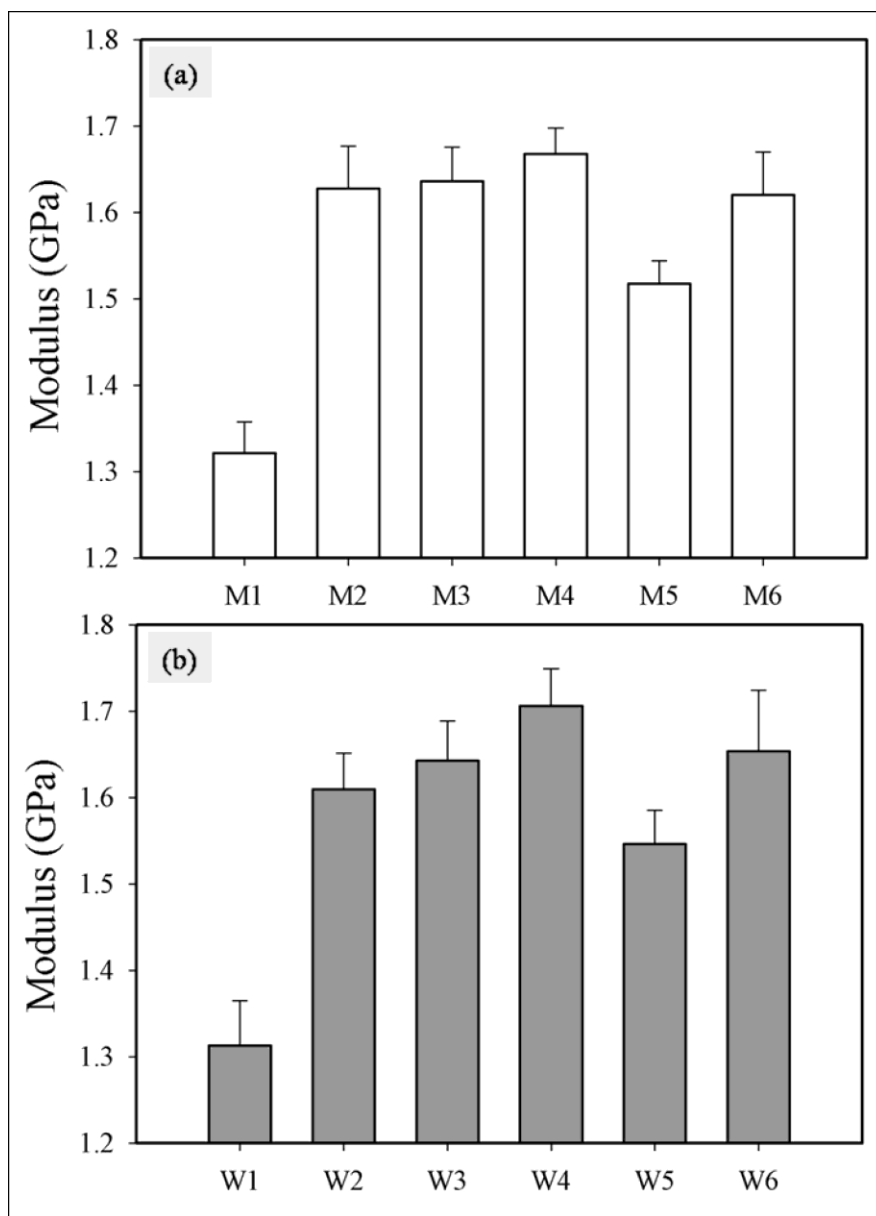


Figure 7.12: Tensile modulus of PCN films in machine direction, prepared using: a) the first screw profile; and b) the second screw configuration.

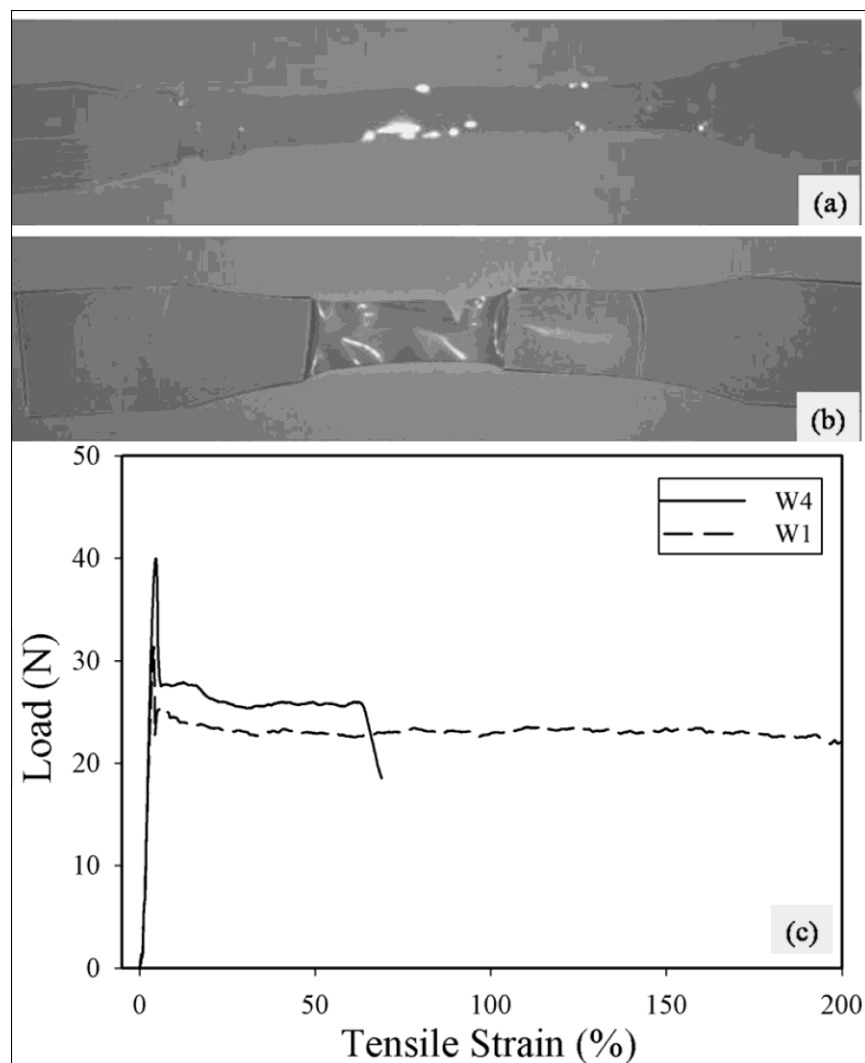


Figure 7.13: a) W1 after elongation at 200 %; b) W4 after elongation at break; and c) load vs. tensile strain for both W1 and W4. Both samples were 68  $\mu\text{m}$  thick.

## 7.4 Conclusion

PET nanocomposite films based on Cloisite 30B clay were prepared by cast extrusion followed by stretching, using chill rolls. TEM and WAXD were used to characterize the morphology and the states of delamination and dispersion. The PCNs containing C30B showed a partially exfoliated/intercalated structure. WAXD patterns showed that the silicate layers were oriented in

the MD (machine direction), which is in agreement with the TEM analysis. DSC data showed that cold crystallization of PCN films containing C30B occurred at a lower temperature and the crystallinity increased from 6-7% for the neat polymer to about 12-13 % for the PNCs. XRD results showed that the interlayer distance of clay platelets, i.e. the state of intercalation, was independent of the processing conditions. However, TEM analysis showed that the level of clay delamination was influenced by an increment of screw speed (higher applied strain at 250 rpm), a reduction in feeding rate (longer residence time at 1.5 kg/h) and inserting severe mixing elements in the screw (second screw configuration). The results of morphological studies and barrier properties suggest that both higher screw speeds and longer residence times have a beneficial influence on the level of delamination and dispersion of the silicate layers. The mechanical results suggest that PET chains might undergo degradation for the longer residence time. The results also reveal that the applied strain has a stronger effect than the residence time on the barrier and mechanical properties. At the highest screw speed ( $N=250$  rpm), 27% reduction in oxygen permeability and 30% improvement in tensile modulus were obtained upon using the screw profile designed for more intensive mixing.

## **7.5 Acknowledgments**

The authors would like to gratefully thank CREPEC member, Ms. Leelapornpisit, who prepared the TEM micrographs. We are also thankful for the assistance of Mr. Yves Simard and Mr. Abbas Ghanbari for the cast extrusion process. We also appreciate the generosity of DuPont Canada for supplying one of the PET resins. This project was jointly funded by NRC-NSERC-BDC.

## 7.6 References

- Barber, G.D., Calhoun, B.H., Moore R.B., “Poly(ethylene terephthalate) ionomer based clay nanocomposites produced via melt extrusion”, *Polymer*, **46**, 6706-6714 (2005)
- Barker, C.P., Kochem, K.H., Revell, K.M., Kelly, R.S.A., Badyal, J.P.S., “Atomic force microscopy and permeability study of stretching-induced gas barrier loss of AlO<sub>x</sub> layers”, *Thin Solid Films*, **259**, 46-52 (1995)
- Bikiaris, D., Karavelidis, V., Karayannidis, G., “A new approach to prepare poly(ethylene terephthalate)/silica nanocomposites with increased molecular weight and fully adjustable branching or crosslinking by SSP”, *Macromol. Rapid Commun.*, **27**, 1199-1205 (2006)
- Brandao L.S., Mendes, L.C., Medeiros, M.E., Sirelli, L., Dias, M.L., “Thermal and mechanical properties of poly(ethylene terephthalate)/lamellar zirconium phosphate nanocomposites”, *J. Appl. Polym. Sci.*, **102**, 3868-3876 (2006)
- Chen X., Gong, H., Yujun, C., Kun, Y., Yeping, D., Hui, Z., “Effect of molecular weight on crystallization, melting behavior and morphology of poly(trimethylene terephthalate)”, *Polym. Test.*, **26**, 144-153 (2007)
- Cho, J.W., Paul, D.R., “Nylon 6 nanocomposites by melt compounding”, *Polymer*, **42**, 1083-1094 (2001)
- Chung, J.W., Son, S.B., Chun, S.W., Kang, T.J., Kwak, S.Y., “Thermally stable exfoliated poly(ethylene terephthalate) (PET) nanocomposites as prepared by selective removal of organic modifiers of layered silicate”, *Polym. Degrad. Stabil.*, **93**, 252-259 (2008).
- Costache, M.C., Heidecker, M.J., Manias, E., Wilkie, C.A., “Preparation and characterization of poly(ethylene terephthalate)/clay nanocomposites by melt blending using thermally stable surfactants”, *Polym. Advan. Technol.*, **17**, 764-771 (2006)

- Davis, C.H., Mathias, L.J., Gilman, J.W., Schiraldi, D.A., Shields, J.R., Trulove, P., Sutto, T.E., Delong, H.C., “Effects of melt-processing conditions on the quality of poly(ethylene terephthalate) montmorillonite clay nanocomposites”, *J. Polym. Sci. Pol. Phys.*, **40**, 2661-2666 (2002)
- Dennis, H.R., Hunter, D.L., Chang, D., Kim, S., White, J.L., Cho, J.W., Paul, D.R., “Effect of melt processing conditions on the extent of exfoliation in organoclay-based nanocomposites” *Polymer*, **42**, 9513-9522 (2001)
- Fasulo P. D., Rodgers, W. R., Ottaviani, R. A., Hunter, D. L., “Extrusion processing of TPO nanocomposites”, *Polym. Eng. Sci.*, **44**, 1036-1045 (2004)
- Fornes, T.D., Yoon, P.J., Keskkula, H., Paul, D.R., “Nylon 6 nanocomposites: The effect of matrix molecular weight”, *Polymer*, **42**, 9929-9940 (2002a)
- Fornes, T.D., Yoon, P.J., Hunter, D.L., Keskkula, H., Paul, D.R., “Effect of organoclay structure on nylon 6 nanocomposite morphology and properties”, *Polymer*, **43**, 5915-5933 (2002b)
- Fornes, T.D., Hunter, D. L., Paul, D. R., “Effect of sodium montmorillonite source on nylon 6/clay nanocomposites”, *Polymer*, **45**, 2321-2331 (2004)
- Ghasemi, H., Carreau, P.J., Kamal, M.R., Calderon, J.U., “Preparation and characterization of PET/Clay nanocomposites by melt compounding”; Accepted in *Polym. Eng. Sci.* (2010a)
- Ghasemi, H., Carreau, P.J., Kamal, M.R., Tabatabaei, S.H., “*Properties of PET nanocomposite films*”, Submitted to *Polym. Eng. Sci.* (2010b)
- Gurmendi, U., Eguiazabal, J.I., Nazabal, J., “Structure and Properties of Nanocomposites with a Poly(ethylene terephthalate) Matrix”, *Macromol. Mater. Eng.*, **292**, 169-175 (2007)
- Hartley, P.A., Parfitt, G.D., “Dispersion of powders in liquids. 1. The contribution of the van der Waals force to the cohesiveness of carbon black powders”, *Langmuir*, **1**, 651-657 (1985)
- Hotta, S., Paul, D.R., “Nanocomposites formed from linear low density polyethylene and

- organoclays” *Polymer*, **45**, 7639-7654 (2004)
- Ke, Z., Yongping, B., “Improve the gas barrier property of PET film with montmorillonite by in situ interlayer polymerization”, *Mater. Lett.*, **59**, 3348-3351 (2005)
- Kim, D., Lee, J. S., Barry, C. F., Mead, J. L., “Evaluation and prediction of the effects of melt-processing conditions on the degree of mixing in alumina/poly(ethylene terephthalate) nanocomposites”, *J. Appl. Polym. Sci.*, **109**, 2924-2934 (2008)
- Lauritzen, J.I., Hoffman, J.D., “Extension of Theory of Growth of Chain-Folded Polymer Crystals to Large Undercooling”, *J. Appl. Phys.*, **44**, 4340 (1973)
- Lertwimolnun, W., Vergnes, B., “Influence of compatibilizer and processing conditions on the dispersion of nanoclay in a polypropylene matrix”, *Polymer*, **46**, 3462-3471 (2005)
- Lertwimolnun, W., Vergnes, B., “Effect of processing conditions on the formation of polypropylene/organoclay nanocomposites in a twin screw extruder”, *Polym. Eng. Sci.*, **46**, 314-323 (2006)
- Lertwimolnun, W., Vergnes, B., “Influence of screw profile and extrusion conditions on the microstructure of polypropylene/organoclay nanocomposites”, *Polym. Eng. Sci.*, **47**, 2100-2109 (2007)
- Li, X., Park, H.M., Lee, J.O., Ha, C.S., “Effect of blending sequence on the microstructure and properties of PBT/EVA-g-MAH/organoclay ternary nanocomposites”, *Polym. Eng. Sci.*, **42**, 2156-2164 (2002)
- Lin, B., Thumen, A., Heim, H.P., Scheel, G., Sundararaj, U., “Nylon 66/clay nanocomposite structure development in a twin screw extruder”, *Polym. Eng. Sci.*, **49**, 824-834 (2009)
- Lu, C., Mai, Y.W., “Influence of Aspect Ratio on Barrier Properties of Polymer-Clay Nanocomposites”, *Phys. Rev. Lett.*, **95**, 088303 (2005)
- Luo, Z.P., Koo, J.H., “Quantifying the dispersion of mixture microstructures”, *J. Microsc.*, **225**,

118-125 (2007)

Luo, Z.P., Koo, J.H., “Quantification of the layer dispersion degree in polymer layered silicate nanocomposites by transmission electron microscopy”, *Polymer*, **49**, 1841-1852 (2008)

Manas-Zloczower, I., “Mixing and Compounding of Polymers”, Hanser Publications, Ohio (2009)

McKelvey, J. M., “*Polymer Processing*”, Wiley-Interscience, New York (1962)

Modesti, M., Lorenzetti, A., Bon, D., Besco, S., “Effect of processing conditions on morphology and mechanical properties of compatibilized polypropylene nanocomposites”, *Polymer*, **46**, 10237-10245 (2005)

Peltola, P., Valipakka, E., Vuorinen, J., Syrjala, S., Hanhi, K., “Effect of rotational speed of twin screw extruder on the microstructure and rheological and mechanical properties of nanoclay-reinforced polypropylene nanocomposites”, *Polym. Eng. Sci.*, **46**, 995-1000 (2006)

Ramirez-Vargas, E., Valera-Zaragoza, M., Sanchez-Valdes, S., Hernandez-Valdez, J. S., Ibarra-Castillo, F. F., “Effect of processing conditions on the structural morphology of PP-EP/EVA/organoclay ternary nanocomposites” *Polym. Bull.*, **62**, 391-403 (2009)

Ray, S.S., Okamoto, K., Okamoto, M., “Structure-property relationship in biodegradable poly(butylene succinate)/layered silicate nanocomposites”, *Macromolecules*, **36**, 2355-2367 (2003)

Schmachtenberg, E., Costa, F.R., Gobel, S., “Microwave assisted HMDSO/oxygen plasma coated polyethylene terephthalate films: Effects of process parameters and uniaxial strain on gas barrier properties, surface morphology, and chemical composition”, *J. Appl. Polym. Sci.*, **99**, 1485-1495 (2006)

Spencer, R.S., Wiley R.M., “The mixing of very viscous liquids”, *J. Colloid Sci.*, **6**, 133-145 (1951)

- Roy P., "Optical Properties of Packaging Materials", *Journal of Plastic Film and Sheeting*, **9**, 173-180 (1993)
- Tanoue, S., Hasook, A., Itoh, T., Yanou, M., Iemoto, Y., Unryu, T., "Effect of screw rotation speed on the properties of polystyrene/organoclay nanocomposites prepared by a twin-screw extruder", *J. Appl. Polym. Sci.*, **101**, 1165-1173 (2006)
- Tarapow, J.A., Bernal, C. ., Alvarez, V.A., "Mechanical properties of polypropylene/clay nanocomposites: Effect of clay content, polymer/clay compatibility, and processing conditions", *J. Appl. Polym. Sci.*, **111**, 768-778 (2009)
- Todorov, L.V., Viana, J.C., "Characterization of PET nanocomposites produced by different melt-based production methods", *J. Appl. Polym. Sci.*, **106**, 1659-1669 (2007)
- Xu X., Ding, Y., Qian, Z., Wang, F., Wen, B., Zhou, H., Zhang, S., Yang, M., "Degradation of poly(ethylene terephthalate)/clay nanocomposites during melt extrusion: Effect of clay catalysis and chain extension", *Polym. Degrad. Stabil.*, **94**, 113-123 (2009)
- Yano, K., Usuki, A., Okada, A., "Synthesis and properties of polyimide-clay hybrid films", *J. Polym. Sci. A1*, **35**, 2289-2294 (1997)
- Zhao, Z., Tang, T., Qin, Y., Huang, B., "Effects of Surfactant Loadings on the Dispersion of Clays in Maleated Polypropylene", *Langmuir*, **19**, 7157-7159 (2003)
- Zhu, L., Xanthos, M., "Effects of process conditions and mixing protocols on structure of extruded polypropylene nanocomposites", *J. Appl. Polym. Sci.*, **93**, 1891-1899 (2004)

## CHAPTER 8

### GENERAL DISCUSSION

Various issues arise in the processing of PET at high temperature to produce polymer/clay nanocomposites (PCNs). These include thermal stability of the organically modified clay, thermal stability of PET and compatibility between PET and the organic modifier. Different types of organomodified clay were used in the first step of this study, including ammonium, phosphonium and imidazolium surfactants. Our findings showed that an ammonium based commercial clay, Cloisite 30B (C30B), displays the best morphology according to delamination state of clay layers in the PET. Direct observation by SEM revealed that the quality of the distributive mixing of the tactoids appears to be good and both individual platelets and tactoid aggregates are seen in TEM micrographs. On the other hand, C30B has lower thermal stability than other types of used organomodified clay. In fact, the presence of two hydroxyl groups in C30B could bring about good compatibility between PET chains and the organoclay, but they are suspected of causing thermal degradation of the modifier at the processing temperature of PET. The observed clay aggregates in C30B PCN are probably due to poor mixing and, in part, to the collapse of silicate layers as a result of degradation of the modifier at the processing temperature. Lack of compatibility between PET chains and imidazolium surfactants could be an explanation for presence of tactoids in the system. Regardless of improvement in thermal stability, compared to C30B, the poor dispersion level of clay layers is an important issue in this type of organomodified clay.

In view of the low thermal stability of ammonium surfactants, a number of phosphonium surfactants were examined in this study. These compounds and corresponding organoclays have

shown improved resistance to thermal degradation at the processing temperature of PET, but compatibility between these surfactants and PET still remains as a critical issue. The corresponding nanocomposites have more tactoids and a clustered structure. Various factors might explain the larger quantity of tactoids in the phosphonium based nanocomposites. These include lower diffusivity of PET into the gallery spacing of the silicate layers and possibly the need for employing a more intensive mixing for the case of phosphonium systems. The interlayer population density influences the degree of intercalation in the system. Although, the organophilicity of the clay is enhanced by a higher interlayer population density, the PET chains would penetrate with difficulty into the galleries due to saturation by surfactant molecules or high organic content.

To form a nanocomposite in melt extrusion, the stacks of clay platelets must be broken into smaller tactoids. Then, the polymer chains should penetrate the gallery space. The high molecular weight and long polymeric chains can provide more shear viscous forces in the mixing process. On the other hand, low molecular weight and shorter polymer chains can penetrate more easily into the gallery spaces of clay. In the second phase of this thesis and in order to improve the processability, an experimental grade high viscosity and a low viscosity general purpose grade of PET were blended at a ratio of 4:1 (low: high viscosity). Since C30B showed the best morphological results among the used organmodified clay, PET nanocomposite films containing 3 wt% C30B were prepared by cast extrusion followed by stretching, using chill rolls. Morphological studies including direct observation by TEM and 2-D WAXD revealed that the silicate layers were laid in the flow direction. The full width at half maximum (FWHM) obtained from the azimuthal intensity profiles showed that in cast film extrusion, owing to the stretching at the exit of the slit die, most of the silicate layers were in the machine direction (MD). Increasing the draw ratio did not have a significant effect on the state of orientation of the clays.

DSC results showed lower crystallization temperature for PCN films, indicating that the clay acts as a nucleating agent during cold crystallization. When crystallization takes place farther below the melting region, it is controlled by growth from a kinetic point of view. Thus, the presence of more nuclei in the system leads to faster rate of crystallization. The crystallinity increases by a factor larger than 2 for the PCN incorporating 3 wt% C30B, which represents the amount of crystallinity induced during the cast extrusion process due to the presence of clay. The degree of crystallinity is also enhanced by ca. 4 times for the PCN 3 wt% C30B, annealed at 150°C. The presence of silicate layers reduces the clarity and increases haze, as expected for the case of incomplete exfoliation. Since the haze and clarity values for the PCNs are less than 6% and more than 85%, respectively, the transparency of the PCN films could be considered acceptable, according to ASTM D1003.

The measured oxygen permeability values showed that the draw ratio does not have a significant effect on the barrier properties of the products. At a 3 nominal wt% C30B, 23 % reduction in oxygen permeability was obtained. The oxygen permeability of the neat PET and the PCN films decreased by ca. 40 and 46%, respectively, for annealed samples. It suggests that, besides the tortuosity, chain segment immobility due to confined environmental geometry should be taken into account. After annealing, crystal lamellas introduce more confinement and entropic penalty into the matrix, which leads to less chain mobility and reduction of permeation. In other words, along with the effect of silicate layers, the low permeability of the crystalline phase compared to the amorphous phase indicates a complementary approach for reducing gas permeation.

The tear resistance decreases with clay content, in both machine and transverse directions. The resistance to tear propagation in TD is slightly larger than in MD. This might be due to the partial orientation of the PET chains in the flow direction. Clay incorporation leads to an increase

of the tensile modulus and more brittleness, in comparison with the neat PET films. At 3 wt% C30B, the tensile modulus increases by about 20%. Since PCNs exhibited a mix of intercalated structure and dispersed tactoids, this morphology has a significant effect on the reinforcement efficiency. A stack of platelets including an organomodifier or polymer chains between clay layers can be considered as a pseudoparticle, which has a lower effective aspect ratio and higher volume fraction.

To study the effect of processing conditions on properties of the final products, two screw profiles with different mixing elements under different screw speeds ( $N$ ) and feeding rates ( $Q$ ) were used to prepare PET/clay nanocomposite (PCN) films containing 3 wt% C30B. XRD patterns indicated that the interlayer distance of clay platelets in the state of intercalation was somehow independent of the processing conditions, but the macro-scale characterization, including barrier and mechanical properties showed that the level of clay layer delamination was affected by processing conditions. The results reveal that the applied shear has stronger effect than residence time on the barrier and mechanical properties. The longer residence time in the barrel may result in more degradation of the matrix. At the highest screw speed ( $N=250$  rpm), 27% reduction in oxygen permeability and 30% improvement in tensile modulus were obtained for the more severe screw profile.

In view of our finding about the effect of annealing on barrier properties of PCN films and the effect of clay on crystallinity of polymer, isothermal and non-isothermal crystallization kinetics of PCN was also studied. To evaluate the kinetic parameters of crystallization, our efforts in this part were focused on the PCN containing only 1 wt.% C30B. However, the Avrami's theory shows that, overall, isothermal crystallization of PCNs takes place faster, but further analysis using the Lauritzen-Hoffman treatment revealed that the presence of clay leads to less perfect crystalline structure. In other words, the equilibrium melting point of PCNs appeared at

higher temperature and the required work for chain folding in the presence of clay is a bit higher than neat PET. Temperature modulated DSC (MDSC) was employed to shed more light on the multiple melting endotherms phenomenon observed during the heating of isothermally crystallized samples. It revealed that the third endotherm may be attributed to the recrystallization and melting of the crystals reorganized during heating, whereas the first and second peaks are associated with melting of secondary and primary crystals, respectively. The modified Avrami equation and the combined Avrami-Ozawa method were also applied to describe the non-isothermal crystallization process. The calculated effective barrier energy for PCNs was higher than for the neat PET, which indicates a less perfect crystalline structure for PCNs during non-isothermal crystallization.

## CHAPTER 9

### CONCLUSIONS AND RECOMMENDATIONS

#### 9.1 Conclusions

In this dissertation, first, PCNs were prepared in the twin-screw extruder by melt compounding of PET with different types of clay, including a commercial ammonium-based surfactant (C30B), experimental thermally stable phosphonium surfactants (P00 series) and experimental thermally stable imidazolium surfactants. The properties of the PCNs containing these new modifiers were compared in terms of thermal stability and various factors contributing to the quality of dispersion. The phosphonium based nanocomposites exhibited better thermal stability, but they showed a lower degree of intercalation than the ammonium and imidazolium-based nanocomposites. Statistical analysis demonstrates higher dispersion parameter,  $D_{0.1}$ , for PCNs with C30B than PCNs incorporating P00208.

After characterizing the prepared PCN in the first step, C30B and P00208 organomodified clay were selected to produce PCN films. PCN films were prepared successfully, by cast extrusion followed by stretching, using chill rolls. TEM and WAXD were used to study the morphology and state of delamination. However PCN with C30B showed partially exfoliated/intercalated structure, but PCN films with P00208 only depicted dispersed tactoids and stacked platelets. This can be explained according to coarser particle size and lower compatibility of lab-made phosphonium modified clay. WAXD patterns displayed the orientation of silicate layers in MT plane which is in agreement with direct observation by TEM. Thermal studies demonstrated the effective role of silicate layers on crystallization behavior of PCN films. Cold

crystallization of PCN films with C30B took place at lower temperature due to existence of more potential nuclei in the system. Although adding clay begot more scattering of striking light beam and consequently hazier films, but the products were still in the acceptable range of transparency. Adding only 3 nominal wt.% C30B led to 23% oxygen permeability reduction. Comparison between the proposed models and experimental results showed that most of the available models predict 40-50% improvement of barrier properties. Regarding the imperfect exfoliated morphology of the obtained PCN films, the difference between the experiments and the models could be explicable. However silicate layers brought about 20% increment of Young's modulus, the puncture and tear propagation resistance reduced due to brittleness of PCN films. The measured modulus was also compared with Halpin-Tsai and Pseudo-inclusion models.

To study the effect of processing conditions of performance of the final products, PET nanocomposite films based on Cloisite 30B clay were prepared by cast extrusion followed by stretching, using chill rolls. TEM and WAXD were used to characterize the morphology, the state of delamination and the dispersion. The PCNs containing C30B showed a partially exfoliated/intercalated structure. WAXD patterns showed that the silicate layers were oriented in MD (machine direction), which is in agreement with the TEM analysis. DSC data showed that cold crystallization of PCN films with C30B occurred at a lower temperature and the crystallinity increased from 6-7% for the neat polymer to about 12-13 % for the PNCs. XRD results showed that the interlayer distance of clay platelets in the state of intercalation is somehow independent of the processing conditions. However, from the TEM analysis and the mechanical properties the level of clay layers delamination was shown to be affected by the processing conditions. The results of morphological studies and barrier properties suggest that both higher screw speed and shorter residence time have a beneficial influence on the level of delamination and dispersion of the silicate layers. The results for the longer residence time suggest that PET chains might be

degraded. The results also reveal that the applied shear has stronger effect than residence time on the barrier and mechanical properties. At the highest screw speed ( $N=250$  rpm), 27% reduction in oxygen permeability and 30% improvement in tensile modulus were obtained for the more severe screw profile.

In order to the importance of crystallinity in post-process solidification and influence of clay on the crystallinity and consequently final properties of PCN, both non-isothermal and isothermal crystallization kinetics of PCN were investigated, using thermoanalytical tools DSC and DTA. To clarify the effect of clay layer on the crystallization kinetic parameters, our investigation was concentrated on the partially intercalated nanocomposite incorporated with only 1 wt.% C30B. The multiple melting behavior of isothermally crystallized samples were interpreted by employing temperature modulated DSC (MDSC). It was shown that the first and second endotherms were attributed to the melting of secondary and primary crystals, respectively. The significant amount of nuclei left during the first two endotherms, begot reorganization and recrystallization of PET and PCN which demonstrates at the third melting peak. However, Avrami theory showed that overall, isothermal crystallization of PCN takes place faster, but further analysis using Lauritzen-Hoffman secondary nucleation theory depicted that the presence of clay leads to less perfect crystalline structure. In other words, the equilibrium melting point of PCN appears at higher temperature and the required work for chain folding in the presence of clay is a bit higher than neat PET. POM micrographs also proved that smaller crystals ere existed in isothermally crystallized PCN in comparison with PET. The modified Avrami equation and the combined Avrami-Ozawa method were also applied to describe the non-isothermal crystallization process. The calculated effective barrier energy for PCN was higher than PET, which indicates less perfect crystalline structure for PCN during non-isothermal crystallization which confirmed qualitatively by POM results. Both isothermal and non-isothermal kinetic studies showed that

incorporated nanoclay acts as nucleating agents and bring about the faster overall rate of crystallization. However, smaller size and imperfect crystal prevailed in nanocomposites, which concluded by higher equilibrium melting point, more work required for chain folding and higher activation energy.

## **9.2 Originality of the work**

As mentioned in the chapter 2, most of the relevant studies focused on preparation of PCNs with a PET matrix. Due to the required high processing temperature, thermal stability of organomodified clay presents a major challenge. Recently, phosphonium surfactants were introduced as thermally stable modifiers. To clarify the chemical structure of organomodifier on the final morphology of PCNs, substituted groups in phosphonium surfactants were altered from short and rigid groups to long alkyl chains. Moreover, an integrated qualitative and quantitative comparison between phosphonium and ammonium modifiers revealed that the compatibility between PET chains and the organomodifier has stronger effects than thermal stability, per se.

To our knowledge, no study has been conducted on properties of PET nanocomposite films. To fill this gap, optical, thermal, mechanical and barrier properties of the PET nanocomposite films were studied in this dissertation. Macro-scale characterizations including barrier and mechanical properties have been rarely reported. Thus, it has been difficult to assess the influence of the processing conditions on dispersion quality of clay in the final products. In view of the experimental results presented in this work, the applied strain has a stronger effect than the residence time on the barrier and mechanical properties of PCN films.

Finally, there is no consensus in the literature about the effect of clay on the crystallization kinetics of PET. For instance, a reduction [101] and an increase [102] in the equilibrium melting

point were reported for PET incorporating nanoparticles. Moreover, the calculated activation energies were reported as either absolute [103] or negative [104] values. Considering the importance of crystallinity in post-process solidification and influence of clay on the crystallinity and consequently final properties of PCN, both non-isothermal and isothermal crystallization kinetics of PCN were investigated to understand the effect of clay on crystalline structure of PCNs. Both isothermal and non-isothermal kinetic studies showed that nanoclay acts as a nucleating agent and yields a faster overall rate of crystallization. However, in the presence of clay, more work is required for chain folding and the activation energy for crystalline growth is higher. This suggests that smaller size and imperfect crystals are more prevalent in nanocomposites.

### **9.3 Recommendations**

The following unexplored topics are recommended for future research:

- 1) As discussed in chapter 5, compatibility and thermal stability of surfactants are crucial factors in preparation of PCNs and they should be satisfied together. Thus, the chemistry of organomodified clay is one aspect that needs to be explored, to fulfill both compatibility and thermal stability criteria.
- 2) In order to select melt compounding as the preferred method to prepare PCNs, the configuration of screw in the extruder and the geometry of mixing elements should be optimized. This means that the cohesion force between clays particles (electrostatic and van der Waals forces) should be calculated, first. Then the amount of forces provided by mixing elements should be estimated, based on the melt characteristic of polymer and shear/elongational fields of mixing pools between the barrel and screw. Moreover, the geometry of mixing elements

(staggering angle, forward/backward flow, width of kneading blocks) should be taken into account. Modeling and simulation approaches can be used to fulfill these objectives.

3) As pointed out earlier, PCN films were prepared by cast extrusion in this project. Injection blow molding could also be applied to produce PCNs with bottle grade PET. Then, the effect of water permeation on barrier and mechanical properties of the final product could be studied.

## REFERENCES

1. Yoshida M., Tanaka T., Watanabe S., Shinohara M., Lee J.W., Takagi T.; “*Improvement of oxygen barrier of PET film with diamond-like carbon film by plasma source ion implantation*”; Surface and Coating Technology; **174-175**; 1033 (2003)
2. Zhu P., Teranishi M., Xiang J., Masuda Y., Seo W.S., Koumoto K., “*A novel process to form a silica-like thin layer on polyethylene terephthalate film and its application for gas barrier*”; Thin Solid Films; **473**; 351 (2005)
3. Barker C.P., Kochem K.H., Revell K.M., Kelly R.S.A., Badyal J.P.S.; “*Atomic force microscopy and permeability study of stretching –induced gas barrier loss of AlO<sub>x</sub> layers*”; Thin Solid Films; **259**; 46 (1995)
4. Schmachtenberg E., Costa F.R.; Gobel S.; “*Microwave assisted HMDSO/oxygen plasma coated polyethylene terephthalate films: Effects of process parameters and uniaxial strain on gas barrier properties, surface morphology, and chemical composition*”; Journal of Applied Polymer Science; **99**; 1485 (2006)
5. Perkins W.; “*Effect of molecular weight and annealing temperature on the oxygen barrier properties of oriented PET film*”; Polymer Bulletin; **19**; 397 (1988)
6. Sekelik D.J., Stepanov E.V., Nazarenko S., Schiraldi D., Hiltner A., Baer E.; “*Oxygen barrier properties of crystallized and talc-filled polyethylene terephthalate*”; Journal of Polymer Science: Part B: Polymer Physics; **37**; 847 (1999)
7. Qureshi N., Stepanov E.V., Schiraldi D., Hiltner A., Baer E.; “*Oxygen barrier properties of oriented and heat set polyethylene terephthalate*”; Journal of Polymer Science: Part B: Polymer Physics; **38**; 1679 (2000)
8. Lewis E.L.V., Duckett R.A., Ward I.M., Fairclough J.P.A., Ryan, A.J.; “*The barrier properties of*

- polyethylene terephthalate to mixtures of oxygen, carbon dioxide and nitrogen*"; Polymer; **44**; 1631 (2003)
9. Motta O., Di Maio L., Incarnato L., Acierno D.; "*Transport and mechanical properties of PET/Rodrun 3000 blown films*" Polymer; **37**; 2373 (1996)
10. Prattipati V., Hu Y. S., Bandi S., Schiraldi D. A., Hiltner A., Baer E., Mehta S.; "*Effect of compatibilization on the oxygen barrier properties of polyethylene terephthalate/poly(m-xylylene adipamide) blends*"; Journal of Applied Polymer Science; **97**; 1361 (2005)
11. Wu W., Wagner M.H., Qi Q., Weiguang P., Kheirandish S.; "*Morphology and barrier mechanism of biaxially oriented polyethylene terephthalate/ polyethylene 2,6 naphthalate blends*"; Journal of Applied Polymer Science; **101**; 1309 (2006)
12. Chaiko D.J., Leyva A.A.; "*Thermal transition and barrier properties of olefinic nanocomposites*"; Chemistry of Materials; **17**; 13 (2005)
13. Frounchi M., Dadbin S., Salehpour Z., Noferesti M.; "*Gas barrier properties of PP/EPDM blend nanocomposites*"; Journal of Membrane Science; **282**; 142 (2006)
14. Jacquelot E., Espuche E., Gérard J.-F., Duchet J., Mazabraud P.; Journal of Polymer Science, Part B: Polymer Physics; **44**; 431 (2006)
15. Vladimirov V., Betchev C., Vassiliou A., Papageorgiou G., Bikiaris D.; "*Morphology and Gas Barrier Properties of Polyethylene-Based Nanocomposites*"; Composites Science and Technology; **66**; 2935 (2006)
16. Nah C., Ryu H.J., Kim W.D., Choi S.S.; "*Barrier property of clay/acrylonitrile-butadiene copolymer nanocomposite*"; Polymers for Advanced Technologies; **13**; 649 (2002)
17. Park H.M., Lee W.K., Park C.Y., Cho W.J., Ha C.S.; "*Environmentally friendly polymer hybrids: Part I. Mechanical, thermal, and barrier properties of thermoplastic starch/clay nanocomposites*"; Journal of Materials Science; **38**; 909 (2003)

18. Krook M., Morgan G., Hedenqvist M.S.; “*Barrier and mechanical properties of injection molded montmorillonite/polyesteramide nanocomposites*”; Polymer Engineering and Science; **45**; 135 (2005)
19. Krook M., Albertsson A.C., Gedde U.W., Hedenqvist M.S.; “*Barrier and mechanical properties of montmorillonite/ polyesteramide nanocomposites*”; Polymer Engineering and Science; **42**; 1238 (2002)
20. Hwang W.G., Wei K.H., Wu C.M.; “*Mechanical, thermal, and barrier properties of NBR/organosilicate nanocomposites*”; Polymer Engineering and Science; **44**; 1238 (2004)
21. Kim J.T., Oh T.S., Lee D.H.; “*Curing and barrier properties of NBR/organoclay nanocomposite*”; Polymer International; **53**; 406 (2004)
22. Gorrasi G., Tortora M., Vittoria V., Pollet E., Lepoittevin B., Alexandre M., Dubois P.; “*Vapor barrier properties of polycaprolactone montmorillonite nanocomposites: effect of clay dispersion*”; Polymer; **44**; 2271 (2003)
23. Gain O., Espuche E., Pollet E., Alexandre M., Dubois P.; “*Gas barrier properties of poly( $\epsilon$ -caprolactone)/clay nanocomposites: influence of the morphology and polymer/clay interactions*”; Journal of Polymer Science: Part B: Polymer Physics; **43**; 205 (2005)
24. Yingwei D., Iannac S., Sanguigno L., Nicolais L.; “*Barrier and mechanical properties of poly(caprolactone)/ organoclay nanocomposites*”; Macromolecular Symposia; **228**; 115 (2005)
25. Cabedo L., Gimenez E., Lagaron J.M., Gavara R., Saura J.J.; “*Development of EVOH-kaolinite nanocomposites*”; Polymer; **45**; 5233 (2004)
26. Maksimov R.D., Gaidukovs S., Zicans J., Kalnins M., Plume E., Spacek V., Svirglerova P.; “*A nanocomposite based on a styrene-acrylate copolymer and organically modified montmorillonite: I.Mechanical properties*”; Mechanics of Composite Materials; **42**; 263 (2006)
27. Maksimov R.D., Gaidukovs S., Zicans J., Kalnins M., Plume E., Spacek V., Svirglerova P.; “A

- nanocomposite based on a styrene-acrylate copolymer and organically modified montmorillonite: 2. Barrier and thermal properties*"; *Mechanics of Composite Materials*; **42**; 353 (2006)
28. Ke Z., Yongping B.; "*Improve the gas barrier property of PET film with montmorillonite by in situ interlayer polymerization*"; *Materials Letters*; **59**; 3348 (2005)
29. Picard E., Vermogen A., Gerard J.F., Espuche E.; "*Barrier properties of nylon 6-montmorillonite nanocomposite membranes prepared by melt blending: Influence of the clay content and dispersion state: Consequences on modelling*"; *Journal of Membrane Science*; **292**; 133 (2007)
30. Tsai T.Y., Li C.H., Chang C.H., Cheng W.H., Hwang C.L., Wu R.J.; "*Preparation of Exfoliated Polyester/Clay Nanocomposites*"; *Advanced Materials*; **17**; 1769 (2005)
31. Choi W.J., Kim H.J., Yoon K.H., Kwon O.H., Hwang C.I.; "*Preparation and barrier property of polyethylene-terephthalate/clay nanocomposite using clay-supported catalyst*"; *Journal of Applied Polymer Science*; **100**; 4875 (2006)
32. Nielsen L.E.; "*Models for the Permeability of Filled Polymer Systems*" *Journal of Macromolecular Science, Part A Pure and Applied Chemistry*; **1**; 929 (1967)
33. Ou C.F., Ho M.T., Lin J.R.; "*The nucleating effect of montmorillonite on crystallization of PET/montmorillonite nanocomposite*"; *Journal of Polymer Research*; **10**; 127 (2003)
34. Ou C.F., Ho M.T., Lin J.R.; "*Synthesis and characterization of poly(ethylene terephthalate) nanocomposites with organoclay*"; *Journal of Applied Polymer Science*; **91**; 140 (2004)
35. Duangdao A.O., Benjapornthavee H.; "*Preparation of poly(ethylene terephthalate)/montmorillonite nanocomposites films by solution technique*"; *Proceedings of the 2008 International Conference on Nanoscience and Nanotechnology*; 1-4 (2008)
36. Pang K., Kotek R., Tonelli A.; "*Review of conventional and novel polymerization process for polyesters*"; *Progress in Polymer Science*; **31**; 1009 (2006)

37. Liu W., Tian X., Cui P., Li Y., Zheng K., Yang Y.; “*Preparation and characterization of PET/Silica nanocomposites*” *Journal of Applied Polymer Science*; **91**; 1229 (2004)
38. He J.P., Li H.M., Wang X.Y., Gao Y.; “*In situ preparation of poly(ethylene terephthalate)-SiO<sub>2</sub> nanocomposites*”; *European Polymer Journal*; **42**; 1128 (2006)
39. Tian X.Y., Ruan C.J., Cui P., Liu W.T., Zheng J., Zhang X., Yao X.Y., Zheng K., Li Y.; “*Isothermal crystallization and subsequent melting behavior of PET/silica nanocomposites*”; *Chemical Engineering Communications*; **194**, 205 (2007)
40. Yang Y., Xu H., Gu H.; “*Preparation and crystallization of PET/SiO<sub>2</sub> nanocomposites by in-situ polymerization*”; *Journal of Applied Polymer Science*; **102**; 655 (2006)
41. Tian X., Zhang X., Liu W., Zheng J., Ruan C., Cui P.; “*Preparation and properties of poly(ethylene terephthalate)/silica nanocomposites*”; *Journal of Macromolecular Science, Part B: Physics*; **45**; 507 (2006)
42. Hao J., Lu X., Lau S.K., Liu S., Chua Y.C.; “*Poly(ethylene terephthalate)/Clay nanocomposites based on aminododecanoic acid-modified clay: Effect of compatibilizer reactivity on clay dispersion*”; *Journal of Nanoscience and Nanotechnology*; **6**; 3981 (2006)
43. Hong L., Hailun W., Anna Z., Huining X.; “*Hybrid poly(ethylene terephthalate)/silica nanocomposites prepared by in-situ polymerization*”; *Polymer Composites*, **28**; 42 (2007)
44. Zhu X., Wang B., Chen S., Wang C., Zhang Y., Wang H.; “*Synthesis and Non-isothermal Crystallization Behavior of PET/Surface-treated TiO<sub>2</sub> Nanocomposites*”; *Journal of Macromolecular Science, Part B: Physics*; **47**; 1117 (2008)
45. Imai Y., Inukai Y., Tateyama H.; “*Properties of poly(ethylene terephthalate)/layered silicate nanocomposites prepared by two-step polymerization procedure*”; *Polymer Journal*; **35**; 230 (2003)
46. Ke Y., Long C., Qi Z.; “*Crystallization, properties, and crystal and nanoscale morphology of*

- PET-clay nanocomposites*"; Journal of Applied Polymer Science; **71**; 1139 (1999)
47. Saujanya C., Imai Y., Tateyama H., "Structure and thermal properties of compatibilized *pet/expandable fluorine mica nanocomposites*"; Polymer Bulletin; **49**; 65 (2002)
48. Wan T., Chen L., Chua Y.C., Lu X.; "Crystalline morphology and isothermal crystallization kinetics of *poly(ethylene terephthalate)/clay nanocomposites*"; Journal of Applied Polymer Science; **94**; 1381 (2004)
49. Kim S.H., Kim S.C.; "Synthesis and properties of *poly(ethylene terephthalate)/ clay nanocomposites by in situ polymerization*"; Journal of Applied Polymer Science; **103**; 1262 (2007)
50. Hwang S.Y., Lee W.D., Lim J.S., Park K.H., Im S.S.; "Dispersibility of clay and crystallization kinetics for *in situ polymerized PET/pristine and modified montmorillonite nanocomposites*"; Journal of Polymer Science, Part B: Polymer Physics; **46**; 1022 (2008)
51. Monemian, S.A., Goodarzi V., Zahedi P., Angaji M.T.; "PET/imidazolium-based OMMT nanocomposites via *in situ polymerization: Morphological, thermal, and nonisothermal crystallization studies*"; Advances in Polymer Technology; **26**; 247 (2007)
52. Xuepei Y., Chuncheng L., Guohu G., Xiaoqing L., Yaonan X., Dong Z.; "Synthesis and characterization of *poly(ethylene terephthalate)/attapulgite nanocomposites*"; Journal of Applied Polymer Science; **103**; 1279 (2007)
53. Yao X., Tian X., Zhang X., Zheng K., Zheng J., Zhang H., Chen L., Li Y., Cui P.; "Poly(ethylene terephthalate)/attapulgite nanocomposites: Preparation, structure, and properties"; Journal of Applied Polymer Science; **110**; 140 (2008)
54. Lee S.S., Ma Y.T., Rhee H.W., Kim J.; "Exfoliation of layered silicate facilitated by ring-opening reaction of cyclic oligomers in *PET-clay nanocomposites*"; Polymer; **46**; 2201 (2005)
55. Zhang G., Yui T., Shichi T., Takagi K.; "The preparation of clay nanosheets-poly(ethylene

- terephthalate*) hybrid materials”; Composite Interfaces; **11**; 307 (2004)
56. Lai M.C., Kung-Chin Chang K.C., Huang W.C., Hsu S.C., Yeh J.M.; “*Effect of swelling agent on the physical properties of PET–clay nanocomposite materials prepared from melt intercalation approach*”; Journal of Physics and Chemistry of Solids; **69**; 1371 (2008)
57. Wang G., Chen Y., Wang Q.; “*Structure and properties of poly(ethylene terephthalate)/Na<sup>+</sup>-montmorillonite nanocomposites prepared by solid state shear milling (S<sup>3</sup>M) method*”; Journal of Polymer Science, Part B: Polymer Physics; **46**; 807 (2008)
58. Boesel L.F., Pessan L.A.; “*PET organoclay nanocomposites: Morphological characterization*”; Materials Science Forum; **403**; 89 (2002)
59. Andrade M.L.Q., Manrich S., Pessan L.A.; “*Transport properties and solvent induced-crystallization in PET and PET-clay nanocomposite films*”; Journal of Metastable and Nanocrystalline Materials; **22**; 51 (2004)
60. Yuan M., Pan X., Wan C.; “*Investigation of melt-intercalated PET-clay nanocomposites*”; Polymers and Polymer Composites; **12**; 619 (2004)
61. Araujo P.E.R., Araujo SS, Raposo C.M.O., Silva S.M.L.; “*Poly(ethylene terephthalate)(PET)/layered silicate nanocomposites. Effect of Bentonite purification on morpholog/behavior relationship*”; 23<sup>rd</sup> Annual Meeting of Polymer Processing Society (2007)
62. Davis C.H., Mathias L.J., Gilman J.W., Schiraldi D.A., Shields J.R., Trulove P., Sutto T.E., Delong H.C; “*Effects of melt-processing conditions on the quality of poly(ethylene terephthalate) montmorillonite clay nanocomposites*”; Journal of Polymer Science, Part B: Polymer Physics, **40**; 2661 (2002)
63. Pendse, S., Ranade A., D'Souza N., Ratto J.A.; “*Effect of montmorillonite layered silicate (MLS) on crystallization growth rate in semi-crystalline PET nanocomposites*”; Annual Technical Conference (ANTEC); 2343 (2004)

64. Pendse S., Ranade A., D'Souza N., Ratto J.A.; "*Deformation of PET nanocomposites*"; Annual Technical Conference; 3492 (2005)
65. Gurmendi U., Eguiazabal J.I., Nazabal J.; "*Structure and properties of nanocomposites with a poly(ethylene terephthalate) matrix*"; Macromolecular Materials and Engineering; **292**; 169 (2006)
66. Lee W.D., Im S.S., Lim H.M., Kim K.J.; "*Preparation and properties of layered double hydroxide/poly(ethylene terephthalate) nanocomposites by direct melt compounding*"; Polymer; **47**; 1364 (2006)
67. Wang Y., Gao J., Ma Y., Agarwal U.S.; "*Study on mechanical properties, thermal stability and crystallization behavior of PET/MMT nanocomposites*"; Composites: Part B: Engineering; **37**; 399 (2006)
68. Thellen C., Orroth C., Froio D., Lucciarini J., Ratto J., Ranade A., D'Souza N.; "*The effect of maleic anhydride coupling agent on melt processed semi-crystalline PET nanocomposite films*"; Annual Technical Conference (ANTEC); 2130 (2004)
69. Sanchez-Solis A.A., Garcia-Rejon A., Manero O.; "*Production of nanocomposites of PET/montmorillonite clay by an extrusion process*"; Macromolecular Symposia, **192**; 281 (2003)
70. Sanchez-Solis A.A., Romero-Ibarra I., Estrada M.R., Calderas F., Manero O.; "*Mechanical and rheological studies on polyethylene terephthalate-montmorillonite nanocomposites*"; Polymer Engineering and Science; **44**; 1094 (2004)
71. Barber G.D., Calhoun B.H., Moore R.B.; "*Poly(ethylene terephthalate) ionomer based clay nanocomposites produced via melt extrusion*"; Polymer; **46**; 6706 (2005)
72. Wang M., Zhu M., Sun B.; "*A new nano-structured flame-retardant poly(ethylene terephthalate)*"; Journal of Macromolecular Science: Part A: Pure and Applied Chemistry; **43**; 1867 (2006)

73. Boesel L.F., Pessan L.A.; “*PET organoclay nanocomposites: Morphological characterization*”; Materials Science Forum; **403**; 89 (2002)
74. Costache M.C., Heidecker M.J., Manias E., Wilkie C.A.; “*Preparation and characterization of PET/clay nanocomposites by melt blending using thermally stable surfactants*”; Polymers for Advanced Technologies; **17**; 764 (2006)
75. Brandao L.S., Mendes L.C., Medeiros M.E., Sirelli L., Dias M.L.; “*Thermal and mechanical properties of poly(ethylene terephthalate)/lamellar zirconium phosphate nanocomposites*”; Journal of Applied Polymer Science; **102**; 3868 (2006)
76. Patro T.U., Khakhar D.V., Misra A.; “*Phosphonium-based layered silicate—Poly(ethylene terephthalate) nanocomposites: Stability, thermal and mechanical properties*”; Journal of Applied Polymer Science; **113**; 1720 (2009)
77. Chung J.W., Son S.B., Chun S.W., Kang T.J., Kwak S.Y.; “*Thermally stable exfoliated poly(ethylene terephthalate) (PET) nanocomposites as prepared by selective removal of organic modifiers of layered silicate*”; Polymer Degradation and Stability; **93**; 252 (2008)
78. Xinfeng X., Yanfen D., Zhongzhong Q., Feng W., Bin W., Hu Z., Shimin Z., Mingshu Y.; “*Degradation of poly(ethylene terephthalate)/clay nanocomposites during melt extrusion: Effect of clay catalysis and chain extension*”; Polymer Degradation and Stability; **94**; 113 (2009)
79. Stoeffler K., Lafleur P.G., Denault J.; “*Thermal decomposition of various alkyl onium organoclays: Effect on polyethylene terephthalate nanocomposites' properties*”; Polymer Degradation and Stability; **93** 1332 (2008)
80. Chang J.H.; “*Comparison of Thermomechanical Properties and Morphologies of Polyester Nanocomposite Fibers: PBT, PET, and PTT*”; Polymer-Plastics Technology and Engineering; **47**; 791 (2008)
81. Litchfield D.W., Baird D.G.; “*The role of nanoclay in the generation of poly(ethylene*

- terephthalate*) fibers with improved modulus and tenacity”; *Polymer*; **49**; 5027 (2008)
82. Rajeev R.S., Harkin J.E., Soon K., McNally T., Menary G., Armstrong C.G., Martin P.J.; “*Studies on the effect of equi-biaxial stretching on the exfoliation of nanoclays in polyethylene terephthalate*”; *European Polymer Journal*; **45**; 332 (2009)
83. Sanchez-Garcia M.D., Gimenez E., Lagaron J.M.; “*Novel PET Nanocomposites of Interest in Food Packaging Applications and Comparative Barrier Performance With Biopolyester Nanocomposites*”; *Journal of Plastic Film and Sheeting*; **23**; 133 (2007)
84. Frounchi M., Dourbash A.; “*Oxygen Barrier Properties of Poly(ethylene terephthalate) Nanocomposite Films*”; *Macromolecular Materials and Engineering*; **294**, 68 (2009)
85. Tan S., Su A., Li W., Zhou E.; “*New insight into melting and crystallization behavior in semicrystalline poly(ethylene terephthalate)*”; *Journal of Polymer Science, Part B: Polymer Physics*; **38**; 53 (2000)
86. Lu. X.F., Hay J.N.; “*Isothermal crystallization kinetics and melting behaviour of poly(ethylene terephthalate)*”; *Polymer*; **42**; 9423 (2001)
87. Li L., Huang R., Zhang L., Hong S.; “*A new mechanism in the formation of PET extended-chain crystal*”; *Polymer*; **42**; 2085 (2001)
88. Hanley T.L., Forsythe J.S., Sutton D., Moad G., Burford R.P., Knott R.B.; “*Crystallisation kinetics of novel branched poly(ethylene terephthalate): a small-angle X-ray scattering study*”; *Polymer International*; **55**; 1435 (2006)
89. Hee S.M., Won J.Y., Eui S.Y., Byoung C.K., Seung S.I.; “*Effect of shearing on crystallization behavior of poly(ethylene terephthalate)*”; *Journal of Applied Polymer Science*; **80**; 2640 (2001)
90. Chaari F., Chaouche M., Doucet J.; “*Crystallization of poly(ethylene terephthalate) under tensile strain: crystalline development versus mechanical behaviour*”; *Polymer*; **44**; 473 (2002)
91. Chae D.W., Kim B.C.; “*Effects of introducing silica particles on the rheological properties and*

- crystallization behavior of poly(ethylene terephthalate)*"; Journal of Materials Science; **42**; 1238 (2007)
92. Saujanya C., Imai Y., Tateyama H.; "*Structure development and isothermal crystallization behaviour of compatibilized PET/expandable fluorine mica hybrid nanocomposite*"; Polymer Bulletin; **51**; 85 (2003)
93. Wang Y., Gao J., Ma Y., Agarwal U.S.; "*Study on mechanical properties, thermal stability and crystallization behavior of PET/MMT nanocomposites*"; Composites Part B: Engineering; **37**; 399 (2006)
94. Zheng H., Wu J.; "*Preparation, crystallization, and spinnability of poly(ethylene terephthalate)/silica nanocomposites*"; Journal of Applied Polymer Science; **103**; 2564 (2007)
95. Wu T., Ke Y.; "*Melting, crystallization and optical behaviors of poly (ethylene terephthalate)-silica/polystyrene nanocomposite films*"; Thin Solid Films; **515**; 5220 (2007)
96. Lee S.J., Hahm W.G., Kikutani T., Kim B.C.; "*Effects of clay and POSS nanoparticles on the quiescent and shear-induced crystallization behavior of high molecular weight poly(ethylene terephthalate)*"; Polymer Engineering and Science; **49**; 317 (2009)
97. Guan G., Li C., Yuan X., Xiao Y., Liu X., Zhang D.; "*New insight into the crystallization behavior of poly(ethylene terephthalate)/clay nanocomposites*"; Journal of Polymer Science, Part B: Polymer Physics; **46**; 2380 (2008)
98. Chung J.W., Son S.B., Chun S.W., Kang T.J., Kwak S.Y.; "*Nonisothermal crystallization behavior of exfoliated poly(ethylene terephthalate)-layered silicate nanocomposites in the presence and absence of organic modifier*"; Journal of Polymer Science, Part B: Polymer Physics; **46**; 989 (2008)
99. Calderon J.U., Lennox B., Kamal M.R.; "*Thermally stable phosphonium-montmorillonite organoclays*"; Applied Clay Science; **40**; 90 (2008)

100. Stoeffler K., Lafleur P.G., Denault J.; “*Effect of intercalating agents on clay dispersion and thermal properties in polyethylene/montmorillonite nanocomposites*”; Polymer Engineering and Science; **48**; 1449 (2008)
101. Wang Z.G., Hsiao B.S., Fu B.X., Liu L., Yeh F., Sauer B.B., Chang H., Schultz J.M.; “*Correct determination of crystal lamellar thickness in semicrystalline poly(ethylene terephthalate) by small-angle X-ray scattering*”; Polymer; **41**; 1791 (2000)
102. Wan T., Chen L., Chua Y.C., Lu X.; “*Crystalline morphology and isothermal crystallization kinetics of poly(ethylene terephthalate)/clay nanocomposites*”; Journal of Applied Polymer Science; **94**; 1381 (2004)
103. Tan S., Su A., Li W., Zhou E.; “*New insight into melting and crystallization behavior in semicrystalline poly(ethylene terephthalate)*”; Journal of Polymer Science, Part B: Polymer Physics; **38**; 53 (2000)
104. Ke Y., Long C., Qi Z.; “*Crystallization, properties, and crystal and nanoscale morphology of PET–clay nanocomposites*”; Journal of Applied Polymer Science; **71**; 1139 (1999)

## Appendix A

# Isothermal and Non-Isothermal crystallization behavior of PET nanocomposite<sup>1</sup>

Ghasemi Hesam<sup>1</sup>, Carreau Pierre J.<sup>1</sup>, Kamal Musa R.<sup>2</sup>

1) CREPEC, Chemical Engineering Department, Ecole Polytechnique  
C.P. 6079 SUC. CENTRE-VILLE, H3T 1J4, Montreal, Quebec, Canada

2) CREPEC, Department of Chemical Engineering, McGill University  
3610 University Street, H3A 2B2, Montreal, Quebec, Canada

### Abstract

Isothermal and non-isothermal crystallization kinetics of poly(ethylene terephthalate) (PET)/clay nanocomposites were studied. PET/clay nanocomposites (PCNs) containing 1 wt% Cloisite30B (C30B) were prepared via melt compounding. Temperature modulated DSC (MDSC) for isothermally crystallized samples revealed that the third endotherm at the highest temperature may be attributed to the recrystallization and melting of crystals, reorganized during heating, whereas the first and second endotherms are associated with melting of the secondary and primary crystals, respectively. Application of the Avrami equation to the results showed that the overall isothermal crystallization rate of the PET in PCNs was faster than in the neat resin. However, the Lauritzen-Hoffman growth kinetics revealed that the presence of clay produced more defects in the crystalline structure. In other words, the required work for chain folding and equilibrium melting temperature in the presence of clay were somewhat higher than for the neat PET. PCNs have higher activation energy than neat PET during isothermal crystallization, due to the steric hurdles introduced by clay layers, leading to a reduction in the transport of the PET

---

1. Submitted to *Polymer Engineering and Science*

chains into crystallites. The effective non-isothermal activation energy for the PCNs was higher than for PET, which could lead to less perfect crystalline structure in the PCNs.

## **A.1 Introduction**

PET is a semi-crystalline engineering thermoplastic used widely in packaging applications. The polarity, close chain packing via symmetry, intermolecular bonding and high glass transition temperature should make PET a good candidate for barrier applications. However, gas permeability to oxygen has been a challenge in some applications, such as soft drinks and beer containers.

The manipulation of crystallinity has been used as a method to control the permeability of PET products [1-4]. The crystalline phase acts as an impermeable component, thus acting as geometrical hindrances and increasing the tortuosity of the diffusion path. Annealing increases crystal thickness and repairs crystal defects. Consequently, it reduces gas permeability, but it reduces product transparency and leads to brittleness.

The incorporation of layered silicate clay as an impermeable nanoparticle phase in a PET matrix is another approach to enhance gas barrier properties [5-6]. The relatively impermeable silicate layers create a tortuous path within the polymer matrix, thus reducing gas permeability.

The crystallization behavior of PET alone [7-17] and in the presence of an inorganic phase [18-27] has been studied extensively. These studies have shown that isothermal crystallization of PET occurs in two steps [10-11]. The primary stage includes heterogeneous nucleation and three-dimensional spherulitic growth, and the secondary step occurs when one-dimensional growth between the primary lamellae takes place. The former exhibits stronger temperature dependence than the latter. Generally speaking,  $t_{1/2}$ , which represents the reciprocal overall rate of

crystallization, decreases by adding nanoparticles into the PET matrix [18-25]. This is usually attributed to the role of nanoparticles as nucleating agents. However, the opposite behavior was also reported [25].

Studies of the effect of clay on the crystallinity of PET/clay nanocomposite (PCN) films prepared by extrusion casting and the effect of annealing on the barrier properties of PCN films were reported earlier [28]. The results of those studies highlighted the need to investigate the kinetics of the isothermal and non-isothermal crystallization of PET and PET PCNs. In earlier studies, isothermal [29-30] and non-isothermal [31-33] crystallization of PET nanocomposites were studied separately. Furthermore, there is no consensus in the literature about the effect of clay on the crystallization kinetics of PET. For instance, a reduction [18] and an increase [34] in the equilibrium melting point were reported for PET incorporating nanoparticles. Moreover, the calculated activation energies were as either absolute [20] or negative [29] values.

In this work, we report on both isothermal and non-isothermal crystallization kinetics of PET nanocomposites incorporating 1 wt% Cloisite 30B (C30B).

## **A.2 Experimental**

A blend of an experimental grade high viscosity PET, Sellar PTX295 (DuPont), and a low viscosity general purpose resin, PET9921 (Eastman Chemical Co.), at 4:1 ratio, was melt compounded with Cloisite 30B (C30B) (Southern Clay Co), by cast film extrusion. The mixing was carried out in an intermeshing co-rotating twin screw extruder at 175 rpm and 265 °C (die temperature) [28]. The PCN films (25 µm) were used to study the crystallization behavior under isothermal and non-isothermal conditions. To study the influence of clay on the kinetic parameters, the PCNs containing 1 wt% C30B were used. C30B has 30 wt.% organic content.

The ash content of the PCNs incorporating 1 wt% C30B was 0.60%.

The isothermal crystallization behavior of the PCN films was studied using DSC (Pyris1, Perkin Elmer) equipped with Intracooler 1P, under nitrogen atmosphere. Indium was used as a high purity material to calibrate the instrument. Isothermal crystallization was studied in the temperature range 195-215 °C. The samples, enclosed in aluminum pans, were heated from 50 to 300 °C by scanning at 50 °C/min and kept for 5 min above the melting point to erase the thermal history. Then, the specimens were quenched at 150 °C/min to the desirable temperatures for isothermal crystallization and held for 15 min. After isothermal crystallization, the samples were heated at 10 °C/min until complete melting point was achieved.

The non-isothermal crystallization behavior of the PCN films was investigated using DTA (DSCQ1000 TA instruments) under helium atmosphere. The instrument was calibrated using sapphire. The specimens, encapsulated in aluminum pans, were heated by scanning at 50 °C/min to 300 °C and held for 5 min to erase the thermal history. Then, the samples were cooled at rates ranging from 2.5-30 °C/min. To understand the melting endotherms that appear upon heating after isothermal crystallization, a linear heating rate of 4 °C/min, modulation period of 40 s, and temperature amplitude of  $\pm 0.42$  °C were selected.

Both DSC and DTA have some well-known limitations [35]. Since temperature ranges for transitions in the different materials often overlap, they only measure the sum or average heat flow rate values of the overlapping processes. In a conventional DSC/DTA, a linear heat flow rate is applied and the heat flow is measured. In MDSC, the material is subjected to a linear heat flow rate superimposed by small amplitude sinusoidal temperature profile [36]. After Fourier transform and deconvolution of the results [37], the total heat flow pertaining to the linear or average heating rate and the reversing heat flow or heat capacity signal can be obtained. The difference between these signals is related to the kinetic signal, and it is called non-reversing heat

flow. Reversing and non-reversing are not related to the thermodynamic concept of reversibility. The reversing signal measures the thermal transitions related to the heat capacity changes of the sample, like glass transition and melting temperature. The non-reversing signal represents the kinetic processes, including crystallization, decomposition and chemical reaction [38].

Polarized optical microscope (POM) (Olympus BX50) equipped with a Linkam hot-stage (Scientific instruments, CSS450) was used for visual observation of the isothermal and non-isothermal crystallization behavior of the PCNs in the same thermal sequences and protocols used in DSC and DTA experiments.

## **A.3 Results and discussion**

### **A.3.1 Isothermal Crystallization and Melting Characteristics**

The isothermal crystallization of the PET and PCNs was performed at different temperatures, and the crystallized samples were heated from the crystallization temperature to the temperature of the last trace of crystallinity. As shown in Figure A.1, during heating, three endotherms appear, labeled as I-III. On quenching, as a result of supercooling, small domains of aligned chain segments develop and, during the primary stage of isothermal crystallization, lamellar stacks are produced in conjunction with these potential nuclei. With the passage of time, a subsequent secondary crystallization occurs, and the restrained amorphous regions between primary lamellar stacks start to form secondary crystals. Accordingly, the isothermal crystallization yields two populations of lamellar thickness.

Different interpretations of these triple melting endotherms have been given. For example, the second and third endotherms were assigned to the melting of the secondary and primary crystals, respectively, and the first one was associated with the final stage of secondary

crystallization and melting of the small metastable crystals [39].

As mentioned earlier, DSC only measures the sum or average heat flow rate values of the overlapping processes. Using a linear heat flow rate superimposed by small amplitude sinusoidal temperature profile in MDSC we can distinguish the thermal transitions related to the heat capacity from the kinetic processes, including crystallization.

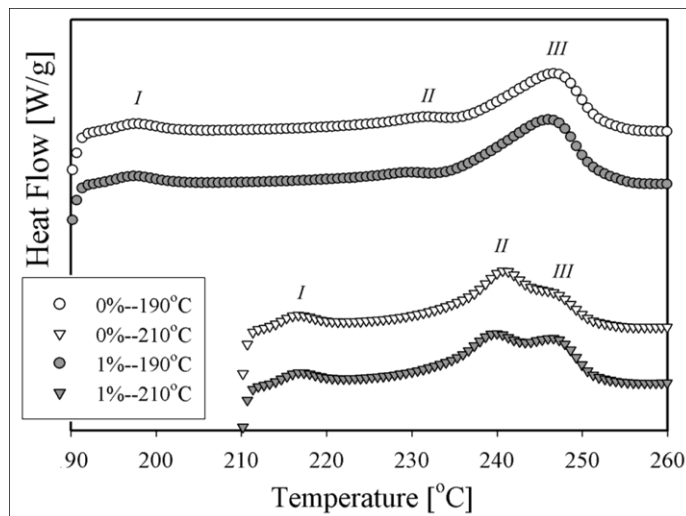


Figure A.1: DSC melting endotherms of isothermally crystallized PET and PCNs at two given temperatures (190 and 210 °C). Samples were heated immediately after isothermal crystallization for duration of 15 min. Open and close symbols are related to the PET and PCNs, respectively.

MDSC traces of the PET resin, after isothermal treatment at an arbitrary temperature (200 °C), are illustrated in Figure A.2. While the reversing endotherm signal magnifies the second and third melting endotherms, the non-reversing signal shows a distinct, exotherm corresponding to the second melting peak. This means that the molten secondary and especially primary crystals provide a substantial number of nuclei, which can undergo recrystallization. The melting of these recrystallized lamellae takes place at a higher temperature, which results in the last endotherm. Thus, the first peak may be attributed to the melting of the less perfect secondary crystals formed

between primary lamellae stacks. The second peak corresponds to the melting of the primary crystals shaped during the first step of crystallization, and the third peak may be associated with the recrystallization and melting of the crystals reorganized during heating [40-41].

Table A.1 shows the triple melting points (identified at the maximum of the endotherms) obtained by DSC for the PET and PCNs, as a result of isothermal crystallization at different temperatures. The third melting point is almost constant, which implies that it pertains to the recrystallization, not crystal dimensions. At the lowest supercooling degree, 215 °C, conventional DSC cannot distinguish the second and third melting points. Owing to high chain mobility, the primary lamellae thickness at this temperature is lower than at the rest of isothermal temperatures. Thus, the melting and recrystallization peaks are merged together, and DSC resolution is not adequate to distinguish between them.

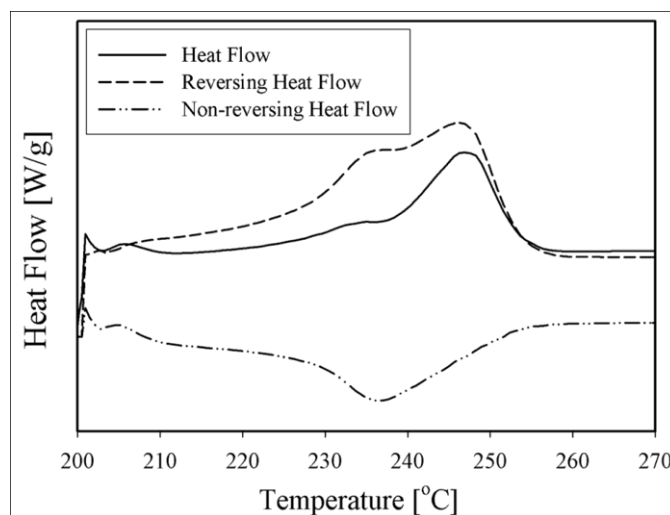


Figure A.2: MDSC melting thermograph of the PET after isothermal crystallization at 200 °C

According to the Hoffman-Weeks equation [42]:

$$T_m = T_m^o \left( 1 - \frac{1}{2\beta} \right) + \frac{T}{2\beta} \quad (1)$$

the equilibrium melting point,  $T_m^o$ , which indicates the melting of a fully extended-chain stack of crystals [43], can be deduced from DSC measurements. The second melting endotherms related to the melting of the primary lamellae were taken as melting points,  $T_m$ , and plotted versus isothermal crystallization temperatures,  $T$ .

Table A.1: Triple melting points of the PET and PCNs versus isothermal crystallization,  $T$ , obtained by DSC.

sample	$T$ (°C)	$T_{m-I}$ (°C)	$T_{m-II}$ (°C)	$T_{m-III}$ (°C)	sample	$T$ (°C)	$T_{m-I}$ (°C)	$T_{m-II}$ (°C)	$T_{m-III}$ (°C)
PET	190	197.7	231.7	246.6	PCNs	190.0	197.3	229.3	246.0
	195	202.3	234.0	246.0		195.0	202.3	232.3	246.0
	200	207.0	236.0	246.0		200.0	207.3	234.6	246.6
	205	212.0	238.6	246.0		205.0	212.0	237.3	246.3
	210	216.7	241.0	246.5		210.0	216.7	239.6	246.6
	215	221.3	243.3	–		215.0	221.7	242.3	–

As demonstrated in Figure A.3, the equilibrium melting point of the PET and PCNs are 267.9 and 270.9 °C, respectively. These are close to the reported values by Chen et al. [34]. According to the Hoffman-Weeks theory, a large assembly of crystals should have an equilibrium degree of perfection consistent with the minimum free energy at  $T_m^o$  [44]. It seems that the presence of clay may delay the formation of a perfect structure with minimum free energy; hence  $T_m^o$  appears at a higher temperature. The lamellar thickening factor,  $\beta$ , obtained from Eq. 1, is 1.07 and 0.97 for the PET and PCNs, respectively. The lower lamellar thickening factor of the PCNs implies that

the crystalline structure of the nanocomposites is less perfect than that of the PET. In other words, the mobility of polymer chains in the vicinity of clay layers is restricted and, as a result, the clay layers impede crystal perfection.

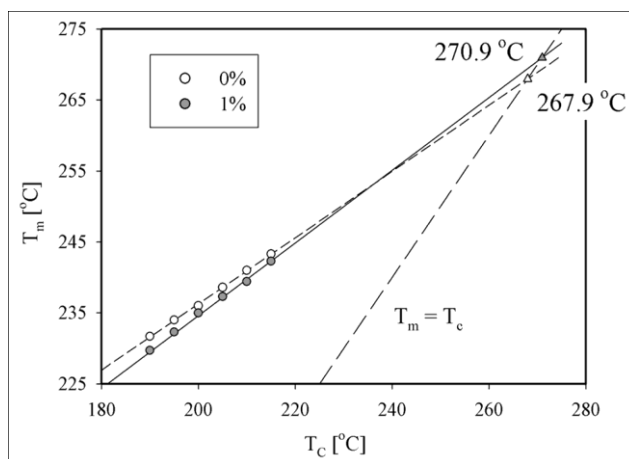


Figure A.3: Application of the Hoffman-Weeks approach to the PET and PCNs. Open and close symbols are related to the PET and PCNs, respectively.

### A.3.2 Isothermal Crystallization Kinetics

DSC traces for isothermal crystallization of the PET and PCNs at various temperatures (Figures A.4a and b) show that crystallization starts earlier at lower temperatures. In this experimental window, 190-215 °C, crystallization is controlled by nucleation. Thus, more nuclei are formed at lower temperatures. When the temperature increases, the characteristic reptation rates of the polymer chains increase. This results in a decrease in the degree of adjacent reentry chain folding during hot crystallization. Since clay layers provide more nuclei, the rate of isothermal crystallization is faster (Table A.2). Assuming that the released heat is linearly proportional to crystallinity, the relative crystallinity can be obtained from the ratio between the area under the thermogram, up to time  $t$ , and the total area under the peak, i.e.:

$$X(t) = \frac{\int_{t_0}^t (dH/dt) dt}{\int_{t_0}^{t_\infty} (dH/dt) dt} \quad (2)$$

where  $t_0$  and  $t_\infty$  are the start and end time of crystallization, respectively, and  $dH/dt$  represents the measured rate of heat flow. Curves depicting the evolution of relative crystallinity with time (Figures A.4c and d) show that slower isothermal crystallization rates are obtained at higher temperatures.

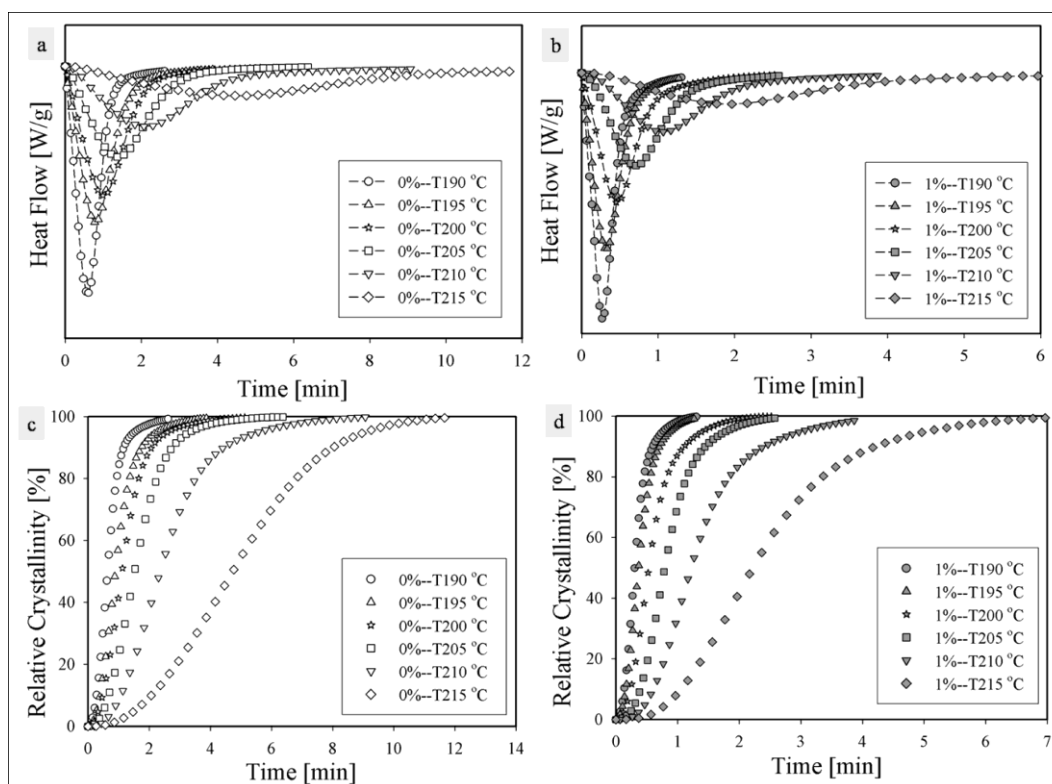


Figure A.4: DSC exotherms of isothermal crystallization at various temperatures of (a) PET; and (b) PCNs and relative crystallinity vs. time during isothermal crystallization at various temperatures of (c) PET; and (d) PCNs

The segments of the sigmoid curves exhibiting the high rate of crystallization represent the primary stage of crystallization, including the formation and growth of spherulites. After most of the crystallization is completed, secondary crystallization takes place. In this stage, the

crystallization rate decreases due to impingement. Also, fibrillar one-dimensional growth between primary lamella occurs. POM micrographs (Figure A.5) show that more rapid morphological changes occur in the PCNs, in qualitative agreement with DSC results. It could also be observed that crystallite size in the PCNs is smaller than in the PET. While crystallite growth in the PET continues for a longer period of time, larger numbers of small crystallites are formed in the PCNs.

Table A.2: Total released heat and results of the Avrami analysis for isothermal crystallization of the PET and PCNs. All tests were done twice and the average values of  $\Delta H$  are reported, here.

samples	$T$ (°C)	$\Delta H$ (J/g PET)	$n$ (-)	$k$ (min <sup>-n</sup> )	$K$ (min <sup>-1</sup> )	$t_{1/2}$ (min)	$t_{\max}$ (min)
PET	190	46.3±0.3	2.18	1.79	1.31	0.65	0.58
	195	46.1±0.2	2.14	0.86	0.93	0.90	0.80
	200	47.3±0.4	2.15	0.55	0.75	1.12	0.99
	205	44.7±0.3	2.34	0.26	0.56	1.53	1.41
	210	45.5±0.1	2.42	0.08	0.36	2.39	2.23
	215	42.9±0.5	2.33	0.02	0.18	4.72	4.34
PCNs	190	50.4±0.1	2.21	9.55	2.77	0.31	0.27
	195	46.5±0.4	2.14	5.83	2.28	0.37	0.33
	200	48.3±0.6	2.21	2.69	1.57	0.54	0.49
	205	46.1±0.3	2.64	1.26	1.09	0.80	0.77
	210	46.1±0.5	2.67	0.39	0.70	1.25	1.20
	215	47.0±0.3	2.56	0.085	0.38	2.27	2.16

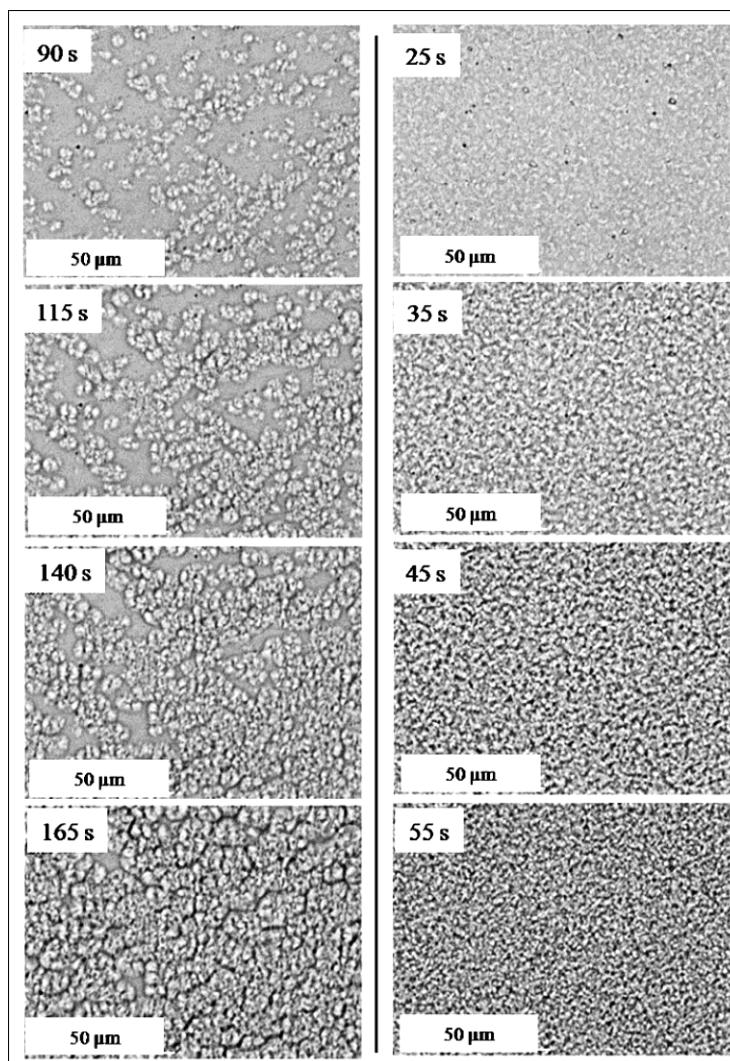


Figure A.5: POM micrographs for isothermal crystallization at 210 °C. Time evolution of crystal growth in left) PET and right) PCN

The total amounts of heat released, per gram of resin, at the different isothermal crystallization temperatures are presented in Table A.2. The measured values of  $\Delta H$  obtained for the PCNs are slightly larger than for the PET, but they do not show strong or systematic variation with the crystallization temperature. The average values of  $\Delta H$  calculated from Table A.2 for the PET and PCNs are 45.5 and 47.4 J/g, respectively. Based on the equilibrium melting enthalpy of PET, 140 J/g [45], the relative crystallinity values estimated for the PET and PCN resins are 32

and 34%, respectively. Thus, incorporating 0.6 wt% clay layers seems to have a small influence on the crystallinity of the matrix, but a significant increase seems to occur at the highest temperature (215 °C).

The double logarithmic form of the Avrami equation [46] is widely used to interpret isothermal crystallization:

$$\log[-\ln(1-X(t))] = n \log t + \log k \quad (3)$$

where the Avrami index,  $n$ , indicates the nucleation type of crystallization, and  $k$  refers to the growth function. The units of  $k$  depend on the value of  $n$ . However, a parameter  $K$  equal  $k^{1/n}$  may be defined to render the units of  $K$  independent of  $n$  [47]. To construct the plot of  $\log [-\ln(1-X)]$  versus  $\log t$ , only the relative crystallinity data up to 80% (the primary stage of crystallization) were used. The straight lines at each temperature ( $R^2 \approx 0.99$ ) allowed the estimation of the Avrami parameters. The Avrami exponent,  $n$ , and Avrami rate constant,  $k$ , were obtained from the slope and intercept of the Avrami plots, respectively. The results are summarized in Table A.2. The values of  $n$  for both PET and PCNs were between 2 and 3, which supports three-dimensional growth. Theoretically, the  $n$  value should be an integer, but in most of the cases, Eq. 3 yielded fractional values. This may be related to the simplifying assumptions made in the Avrami model, such as constant radial growth, complete transformation of the sample, uniqueness of nucleation, constant shape of the growing nuclei and the absence of secondary crystallization [48]. The Avrami exponents are effectively constant and quite similar for both PET and PCNs between 190°C and 200°C. However, the  $n$  values become larger in the temperature range 205 to 215°C, with the PCNs exhibiting significantly larger values of  $n$  than PET. The values of  $K$  for PCNs are approximately twice the values for the PET at the corresponding temperatures (Table A.2). Thus, while the presence of clay does not make an important contribution to crystallinity, it contributes

significantly to increasing the rate of crystallization through its role as a heterogeneous nucleating agent.

The crystallization half-time,  $t_{1/2}$ , is defined as the time at which the crystallinity is half complete.  $t_{\max}$  corresponds to the point at which  $dH/dt$  becomes effectively zero. Both parameters can be obtained from the Avrami equation and are reported in Table A.2:

$$t_{1/2} = \left( \frac{\ln 2}{k} \right)^{1/n} \quad (4)$$

$$t_{\max} = \left( \frac{n-1}{nk} \right)^{1/n} \quad (5)$$

The overall crystallization rate is the reciprocal of  $t_{1/2}$ . As expected, the results in Table A.2 show that the Avrami rate constants,  $k$  or  $K$ , and the overall rate of crystallization decrease as the isothermal crystallization temperature increases, for both PET and PCNs.

To determine the activation energy of crystallization, the Avrami rate constant,  $k$ , was fitted to the Arrhenius equation [49-51]:

$$\frac{1}{n} \ln k = \ln k_0 - \frac{\Delta E}{RT} \quad (6)$$

where  $k_0$  is the temperature independent pre-exponential factor,  $R$  is the gas constant and  $\Delta E$  and  $T$  are total activation energy and crystallization temperature, respectively. The slope of the straight line ( $1/n \ln k$  vs.  $1/T$ ) yields activation energy values of  $140 \pm 1.5$  and  $148 \pm 1.8$  kJ/mol for PET and the PCNs, respectively. In fact,  $\Delta E$  consists of the energy required for the molecules to pass through the phase boundaries to the crystallization surface and also the energy needed to form critical size nuclei. The presence of clay in the matrix provides nucleating sites, thus contributing to the second component of  $\Delta E$ . However, at the same time, clay introduces steric hurdles and might restrict the incorporation ability of the PET chains in the crystal, as will be

shown in the Lauritzen-Hoffman analysis later.

Malkin et al. [52] considered that crystallization consists of two stages: emergence of primary nuclei and subsequent growth of the nucleated crystals. They proposed the following equation to describe the whole range of crystallization experimental data:

$$X = 1 - \frac{C_0 + 1}{C_0 + \exp(C_1 t)} \quad (7)$$

where  $C_0$  and  $C_1$  are constants. His approach leads to the following relation to describe isothermal crystallization:

$$\frac{1}{1-X} \frac{dX}{dt} = A + BX \quad (8)$$

Except for the region at the end of crystallization, Eq. 8 was used to estimate  $A$  and  $B$ , in conjunction with our experimental isothermal crystallization data. The Malkin exponent ( $C_0 = B/A$ ) and the Malkin crystallization rate constant ( $C_1 = A + B$ ) are reported in Table A.3. The pattern exhibited by  $C_1$  is similar to the behavior of  $k$  and  $K$  in the Avrami equation. It decreases with crystallization temperature, and the value of  $C_1$  for the PCNs is ca. 2 times its value for the PET at the same temperature (Table A.3). Apparently the temperature dependency of  $C_0$  coefficient does not follow a monotonic pattern with temperature, which observed by other researchers [53-55]. The macrokinetic Eq. 8 is only valid up to 80% relative crystallinity. Figure A.6 shows a comparison between experimental data and the predictions of the Avrami and Malkin models, at a given temperature. The deviation observed over 80% relative crystallinity is attributed to the secondary crystallization. However, the predictions of the Avrami model for the primary crystallization region are better than those of the Malkin model.

Table A.3: The results of Malkin analysis for isothermal crystallization of the PET and PCNs

sample	$T$ (°C)	$C_0$ (-)	$C_1$ (min <sup>-1</sup> )	sample	$T$ (°C)	$C_0$ (-)	$C_1$ (min <sup>-1</sup> )
PET	190	15.17	4.70	PCNs	190	13.92	9.64
	195	8.83	2.94		195	10.92	7.50
	200	10.47	2.48		200	7.66	4.66
	205	9.43	1.83		205	8.85	3.62
	210	7.08	1.11		210	6.19	2.15
	215	13.95	0.65		215	6.02	1.15

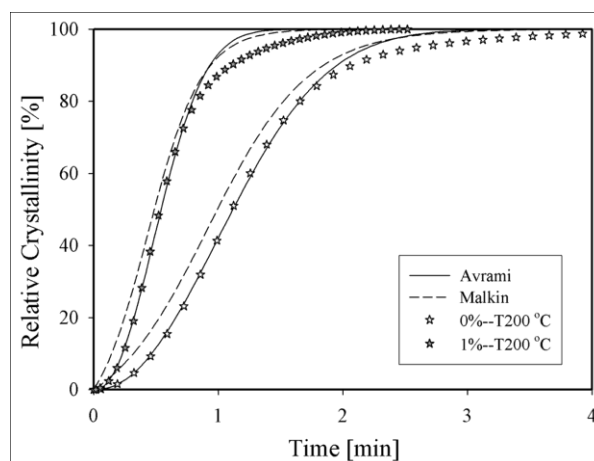


Figure A.6: Comparison between the Avrami and Malkin model predictions with the experimental data at 200 °C. Open and close symbols are related to the PET and PCNs, respectively.

The Lauritzen-Hoffman (LH) regime theory [56] was applied to the experimental data to obtain thermodynamic parameters related to the isothermal crystallization of the PET and the PCNs. According to the LH regime theory of crystal growth, the following equation describes the dependence of crystalline growth rate,  $G$ , on crystallization temperature,  $T$ :

$$G = G_0 \exp\left(-\frac{U^*}{R(T-T_\infty)}\right) \exp\left(-\frac{K_g}{fT\Delta T}\right) \quad (9)$$

where  $G_0$  is the pre-exponential factor. The first and second exponential terms represent the contributions of the growth and nucleation, respectively, to the crystallization process.  $U^*$  is the transport activation energy for diffusion of a polymer segment across a crystal (6284 J/mol) and  $T_\infty$  is a hypothetical temperature below which viscous flow ceases (usually taken as  $T_g - 30$  K) [57]. The glass transition temperature,  $T_g$ , as obtained from the inflection point of the reversing signal in MDSC, is 77.7 for the PET and 77.8°C for the PCNs.  $\Delta T$  denotes the degree of supercooling  $T_m^\circ - T$  and  $K_g$  is a nucleation parameter.  $f = 2T/(T_m^\circ + T)$  is a correction factor that takes the variation of the bulk melting enthalpy with temperature into account. The logarithmic transformation of Eq. 9 leads to:

$$\ln G + \frac{U^*}{R(T-T_\infty)} = \ln G_0 - \frac{K_g}{fT\Delta T} \quad (10)$$

Usually, the reciprocal half time of crystallization,  $1/t_{1/2}$ , is used in place of  $G$ . If the left hand side of the Eq. 10 is plotted against  $(fT\Delta T)^{-1}$ , the nucleation parameter,  $K_g$ , is obtained from the slope of the straight line (Table A.4).

Table A.4: Results of Lauritzen-Hoffman analysis for isothermal crystallization of PET and PCNs

sample	$K_g \times 10^{-5}$ (K <sup>2</sup> )	$G_0 \times 10^{-5}$ (min <sup>-1</sup> )	$\sigma_e \times 10^3$ (J/m <sup>2</sup> )	$q$ (kJ/mol)
PET	2.5	5.5	104	31.7
PCNs	2.9	29.5	120	36.5

To determine the regime of isothermal crystallization, the  $Z$  test [56] is applied to the

calculated  $K_g$  in the experimental window:

$$Z \cong 10^3 \left( \frac{l}{2a_0} \right)^2 \exp\left( -\frac{Y}{T\Delta T} \right) \quad (11)$$

where  $l$  and  $a_0$  are the effective lamellar width and the width of the molecular chains in the crystal, respectively. For PET,  $a_0$  is 0.457 nm [11]. If substitution of  $K_g$  for  $Y$  leads to  $Z \leq 0.01$ , then regime I crystallization kinetics applies. However, if when  $Y$  is replaced with  $2K_g$ ,  $Z$  exceeds 1.0, then regime II kinetics prevails. Using the known value of  $K_g$  and the indicated inequalities for  $Z$ , the effective lamellar width,  $l$ , can be estimated for both regimes [58]. If isothermal crystallization took place in regime I, the effective lamellar width of the PET at 190 °C would be less than 0.09 nm, which is unrealistic. However, regime II crystallization kinetics, at the same temperature, suggests  $l$  greater than 29 nm, which is reasonable. Hence, according to the  $Z$  test, isothermal crystallization occurs in regime II, for both the PET and PCNs.

The nucleation parameter,  $K_g$ , referred to as the secondary nucleation kinetics constant, contains the surface free energy contribution:

$$K_g = \frac{2\sigma\sigma_e b_0 T_m^0}{\Delta H_f k_B} \quad (\text{regime II}) \quad (12)$$

The thickness of a single layer in the crystal,  $b_0$ , for PET is 0.553 nm [26]. The bulk melting enthalpy per unit volume for a 100% crystalline polymer,  $\Delta H_f$ , is  $2.1 \times 10^8$  J/m<sup>3</sup> [45], and  $k_B$  is the Boltzmann constant.  $\sigma$  and  $\sigma_e$  are the lateral and free surface energies, respectively. The lateral surface energy can be estimated from [48]:

$$\sigma = \lambda \Delta H_f (a_0 b_0)^{1/2} \quad (13)$$

where  $\lambda$  is an empirical constant, which is taken as 0.11 [57]. According to Eq. 12, the free surface energy can be determined. The work of chain folding can also be calculated as follows

[57]:

$$q = 2 a_0 b_0 \sigma_e \quad (14)$$

The surface free energy and work of chain folding of the PET and PCNs are presented in Table A.4. The higher values of  $\sigma_e$  and  $q$  corresponding to the PCNs confirm that re-entry of polymeric chains into the crystal is more difficult in the presence of clay layer. Thus, as observed earlier, clay layers act as heterogeneous nucleating agents and facilitate faster crystallization, but spatial hindrance induced by the clay layers restricts the crystallization potential and possibly brings about less crystal perfection.

### **A.3.3 Non-Isothermal Crystallization Kinetics**

Non-isothermal crystallization takes place during the solidification stage of most polymer processing operations, such as injection and blow molding and film blowing and casting. Non-isothermal crystallization of the PET and PCNs was performed at different cooling rates. DTA crystallization exotherms obtained from dynamic crystallization experiments at different cooling rates are presented in Figures A.7a and b. These results show that, as the cooling rate is raised, the crystallization peak occurs at lower temperatures. When the specimens are cooled fast, the characteristic time of reptation is relatively long and the chain mobility lags behind the cooling rate. Thus, polymer molecules have a short time to diffuse into crystallite structures and adjust themselves in a suitable conformation. Thus, crystallization starts later, and the small number of large spherulites yields a broad peak at lower temperatures, compared to behavior at low cooling rates (Figure A.8). Moreover, because the time scale of the experiment is smaller than the characteristic time of crystallization, crystals do not form perfectly, and flawed crystallite units are obtained. Since clay layers provide more nuclei in PCNs, non-isothermal crystallization takes place at higher temperatures and faster rates, as observed in the isothermal studies (Table A.5).

Table A.5: Characteristic data of non-isothermal crystallization of the PET and PCNs. All tests were done twice and the average values of  $\Delta H$  are reported, here.

samples	$\alpha$ (°C/min)	$\Delta H$ (J/g)	$T_0$ (°C)	$T_p$ (°C)	$t_p$ (min)	$T_{1/2}$ (°C)	$t_{1/2}$ (min)
PET	2	42.4±0.2	220	207.8	6.10	207.1	6.46
	5	42.5±0.3	213	198.9	2.82	198.2	2.95
	10	41.0±0.1	207	189.8	1.72	189.3	1.77
	20	37.4±0.4	202	178.7	1.17	178.1	1.19
	30	36.8±0.5	200	174.1	0.86	172.7	0.91
PCNs	2	45.5±0.4	222	212.3	4.85	212.0	4.99
	5	43.4±0.3	216	205.1	2.18	204.9	2.21
	10	44.7±0.6	212	199.8	1.22	199.5	1.25
	20	41.4±0.2	206	190.1	0.80	189.6	0.82
	30	41.7±0.5	203	185.2	0.59	184.5	0.61

The relative crystallinity as a function of temperature can be expressed as:

$$X(t) = \frac{\int_{T_0}^T (dH/dT) dT}{\int_{T_0}^{T_\infty} (dH/dT) dT} \quad (15)$$

where  $T_0$  denotes the initial crystallization temperature,  $T_\infty$  is the temperature after completion of the process and  $dH/dT$  is related to the heat flow rate. The relationship between crystallization temperature,  $T$ , and time,  $t$ , during non-isothermal crystallization experiments is given by:

$$t = \frac{T_0 - T}{\alpha} \quad (16)$$

where  $\alpha$  is the constant cooling rate.

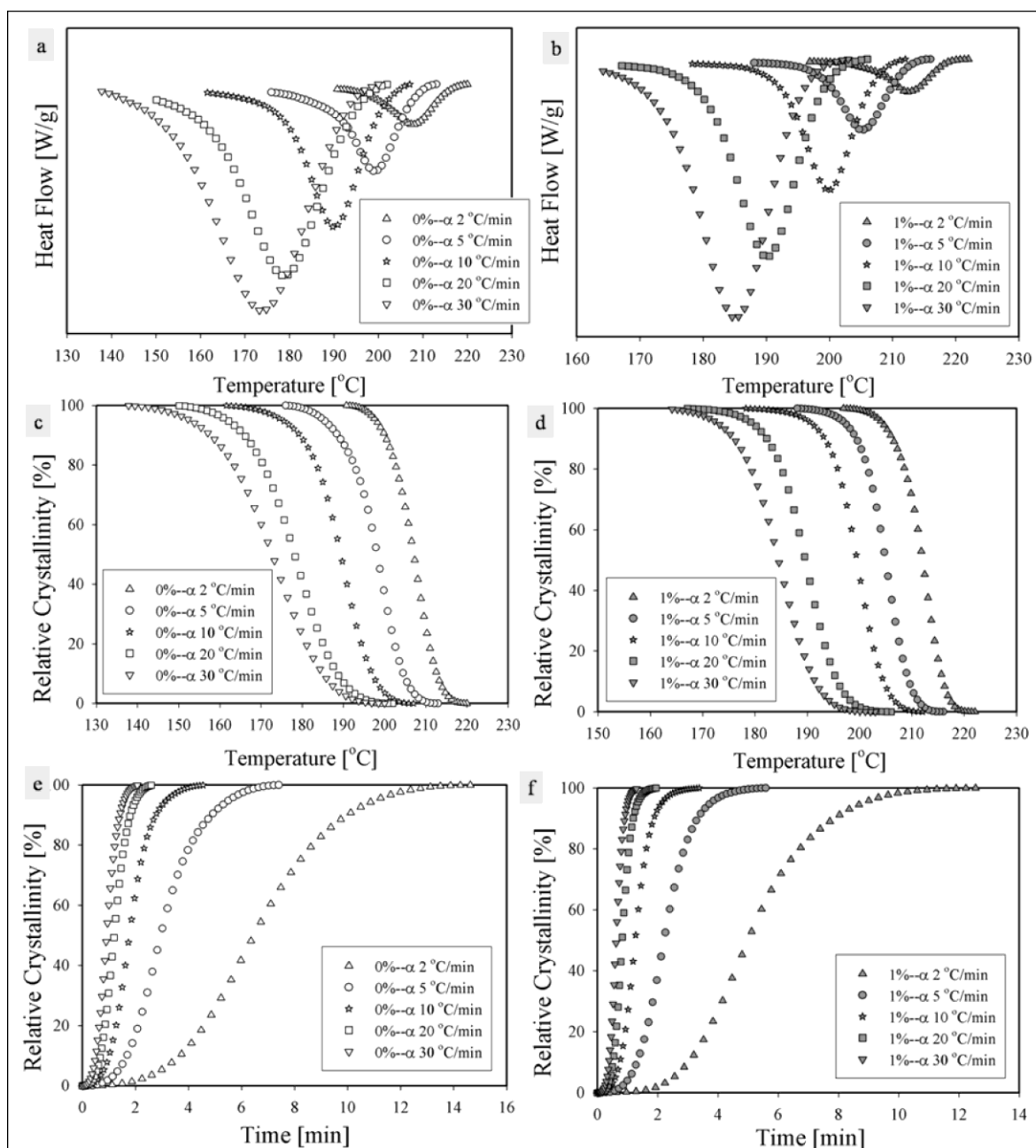


Figure A.7: a & b) DSC exotherms of non-isothermal crystallization of the PET and PCNs at various cooling rates. c & d) Relative crystallinity of the PET and PCNs versus temperatures, at various cooling rates. e & f) Relative crystallinity of the PET and PCNs a function of time, at various cooling rates

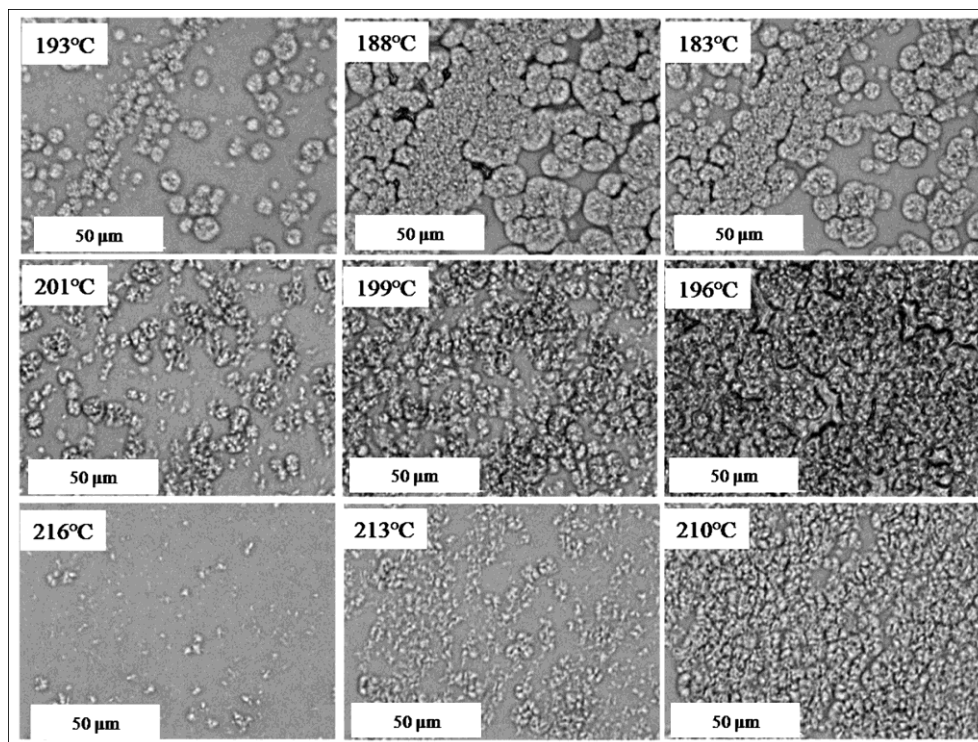


Figure A.8: POM micrographs for non-isothermal crystallization. Time evolution of crystal growth: top) PET at cooling rate 30 °C/min middle) PCNs at cooling rate 30 °C/min bottom) PET at cooling rate 5 °C/min

The evolution of crystallinity with temperature (Figures A.7c and d) and time (Figures A.7e and f) shows that, during non-isothermal crystallization, slower crystallization rates are obtained at lower cooling rates. The reverse S-shaped curves suggest that, at slower cooling rates, the impingement of spherulites occurs at the later stages of crystallization. Characteristic parameters of non-isothermal crystallization for the PET and the PCNs are summarized in Table A.5. The temperature at the maximum crystallization rate,  $T_p$ , the temperature to reach half of the final crystallinity,  $T_{1/2}$ , and their corresponding times,  $t_p$  and  $t_{1/2}$ , decrease with increasing cooling rate, indicating that the crystallization starts and ends later at higher cooling rates. Since clay layers accelerate the nucleation rate, at a chosen cooling rate,  $T_0$ ,  $T_p$  and  $T_{1/2}$  of the PCNs are higher than

for the PET and the corresponding time values are lower.

The total heat released during non-isothermal crystallization decreases with increasing cooling rate. However, the measured values of  $\Delta H$  obtained for the PCNs are slightly larger than for the PET. The average  $\Delta H$  values, calculated from data reported in Table A.5, are 40.0 and 43.3 J/g for the PET and the PCNs, respectively. Using the equilibrium melting enthalpy of PET, 140 J/g [45], the corresponding non-isothermal crystallinity values obtained for the PET and the PCNs are 29 and 31%, respectively. It should be pointed out that the differences at the highest cooling rates (20 and 30°C/min) exceed 10%, in favor of the PCNs.

It has been suggested that the primary stage of non-isothermal crystallization may be described by the Avrami equation, by assuming that it occurs at a fictitious (equivalent) constant crystallization temperature [59]:

$$\log[-\ln(1-X(t))] = n \log t + \log Z_t \quad (17)$$

where  $Z_t$  represents the Avrami growth rate constant. However, the physical meaning of the parameters is not exactly the same as for isothermal crystallization, owing to the variability of temperature. The dependence of non-isothermal crystallization rate on cooling rate dictates a correction of  $Z_t$  to obtain the crystallization kinetic rate constant,  $Z_c$  [60]:

$$\log Z_c = \frac{\log Z_t}{\alpha} \quad (18)$$

Only the relative crystallinity data up to 80%, (the primary stage of crystallization) were used to construct the Avrami plots and the straight lines at each cooling rate ( $R^2 \approx 0.99$ ) allowed the estimation of  $n$ ,  $Z_t$  and  $Z_c$ , which are reported in Table A.6. The values of  $n$  for both PET and PCNs are between 3 and 4, which indicate three-dimensional growth. The non-isothermal crystallization kinetic rate constant,  $Z_c$ , increases substantially with cooling rate, indicating faster crystallization. At a given cooling rate, the PCNs have a greater  $Z_c$  value due to the nucleating

effect of the clay.

Assuming non-isothermal crystallization to consist of infinitesimal steps of isothermal crystallization, Ozawa [61] derived the following equation:

$$\log[-\ln(1-X(T))] = \log K(T) - m \log \alpha \quad (19)$$

where  $m$  is the Ozawa exponent associated with the dimensions of crystal growth and  $K(T)$  is a crystallization rate related function. Based on this theory, Eq. 19 at a given temperature should lead to a series of straight lines. The temperature range used to conduct the Ozawa analysis of non-isothermal crystallization was 183-195 °C (Figure A.9). Curvature appears at higher cooling rates, indicating that this theory should be applied with caution. The variation of the slope,  $m$ , with temperature also suggests that Ozawa's approach cannot accurately describe the non-isothermal crystallization of the PET and PCNs.

Table A.6: Results of the Avrami analysis for non-isothermal crystallization of the PET and PCNs

sample	$\alpha$ (°C/min)	$n$ (-)	$Z_t \times 10^2$ (min <sup>-n</sup> )	$Z_c \times 10^2$ (-)	sample	$\alpha$ (°C/min)	$n$ (-)	$Z_t \times 10^2$ (min <sup>-n</sup> )	$Z_c \times 10^2$ (-)
PET	2	3.15	0.2	4.3	PCNs	2	3.69	0.2	4.2
	5	3.15	2.1	46.4		5	3.48	4.2	53.1
	10	3.11	11.4	80.4		10	3.36	31.4	89.1
	20	3.15	38.8	95.4		20	3.79	142.3	101.8
	30	3.09	90.6	99.7		30	3.83	425.9	104.9

A recent kinetic model combines the Ozawa and Avrami equations [62]. The following equation describes the relationship between cooling rate,  $\alpha$ , and time,  $t$ , at a given degree of crystallinity:

$$\ln \alpha = \ln F(T) - \gamma \ln t \quad (20)$$

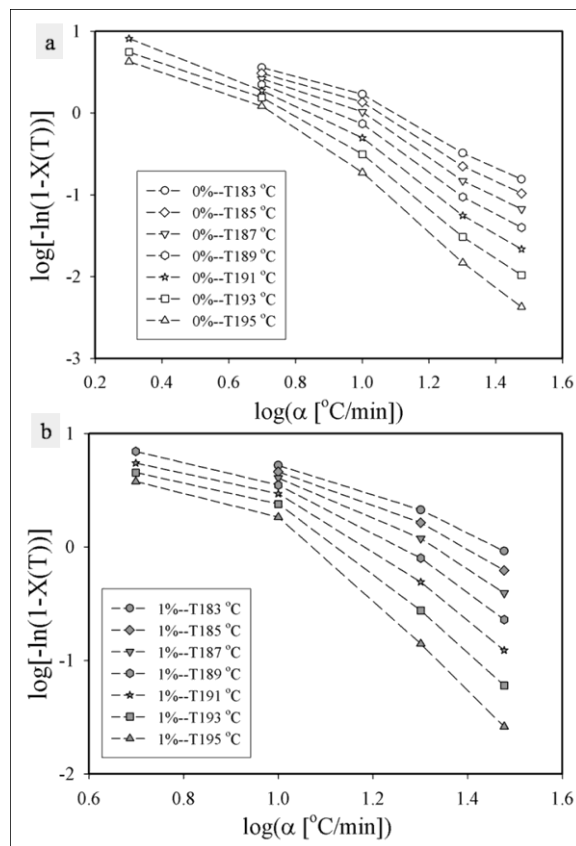


Figure A.9: Ozawa analysis for non-isothermal crystallization of the a) PET; and b) PCNs

Table A.7: Results of the combined Avrami and Ozawa kinetic models for non-isothermal crystallization of the PET and PCNs

sample	$X$ (%)	$\ln F(T)$ (-)	$\gamma$ (-)	sample	$X$ (%)	$\ln F(T)$ (-)	$\gamma$ (-)
PET	20	2.72	1.38	PCNs	20	2.33	1.32
	40	3.07	1.39		40	2.60	1.30
	60	3.32	1.39		60	2.80	1.29
	80	3.60	1.38		80	3.02	1.27

where  $F(T)$  refers to the value of the cooling rate chosen at a unit crystallization time when the system has a certain degree of crystallinity, and  $\gamma$  is the ratio of Avrami to Ozawa exponents. According to Eq. 20, at a given degree of crystallinity, the plot of  $\ln \alpha$  versus  $\ln t$  yields a straight line ( $R^2 \approx 0.99$ ). Table A.7 shows that the values of  $F(T)$  increase with the relative degree of crystallinity,  $X$ , and they are lower in the presence of clay layers, indicating that the PCNs crystallize at a faster rate than PET.

Several methods have been proposed to evaluate the effective activation energy for non-isothermal crystallization, by considering the variation of the peak temperature,  $T_p$ , with the cooling rate,  $\alpha$  [63-67]. According to Flynn's equation [67]:

$$\frac{d \ln(\alpha_i)}{d(1/T_{X,i})} = -\frac{\Delta E}{R} \quad (21)$$

the corresponding isothermal crystallization temperature,  $T_X$ , is recorded for every individual cooling rate,  $\alpha_i$ , at an arbitrary degree of crystallinity,  $X$ . Based on this method, a set of effective activation energies is obtained as a function of relative crystallinity (Figure A.10). The dependence of the activation energy on the magnitude of relative crystallinity indicates that more energy is required to transport polymer chains to the crystalline surface during the primary stage of non-isothermal crystallization. This means that the major energy barrier occurs at the start of crystal formation. Subsequently, crystal growth takes place more easily. At a chosen conversion level,  $X$ , Flynn's model predicts higher activation energy for the PCNs than for PET, thus indicating the influence of clay on hindering diffusion. However, the presence of clay enhances nucleation and accelerates the overall rate of crystallization. Another factor which needs to be considered is the role of impingement in the later stages of crystallization.

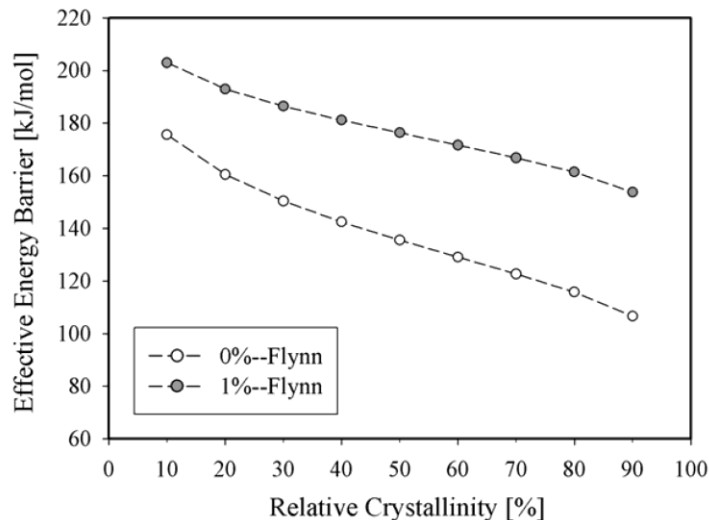


Figure A.10: Dependence of the effective energy barrier on the degree of crystallinity for the PET and PCNs. Open and close symbols are related to the PET and PCNs, respectively.

Table A.8: Crystallization rate coefficient, crystallization rate parameter and crystallization rate index for the PET and PCNs

sample	$CRC = \frac{d\alpha}{dT_p}$ ( $\text{min}^{-1}$ )	$R^2$ (-)	$CRP = \frac{d(1/t_{1/2})}{d\alpha}$ ( $\text{K}^{-1}$ )	$R^2$ (-)	$CRI = \frac{d[(dH/dt)_{T_p}/\Delta H]}{d(1/t_{1/2})}$	$R^2$ (-)
PET	0.79	0.919	0.03	0.976	1.08	0.994
PCNs	1.02	0.949	0.05	0.981	1.36	0.999

A crystallization rate coefficient (CRC) [68], a crystallization rate parameter (CRP) [69] and a crystallization rate index (CRI) [70] were used to evaluate the overall rate of non-isothermal crystallization. The results of these different approaches are presented in Table 8. The higher values of these parameters indicate a faster crystallization rate for PCN samples compared to the neat PET. Straight-line fits are better with the CRI data than with CRP and CRC, as indicated by

correlation coefficients ( $R^2$ ). In fact, CRC and CRP are directly related to cooling rate, while CRI takes into account crystallization rate ( $1/t_{1/2}$ ) and instantaneous crystallization rate at the peak temperature, for each cooling rate.

#### **A.4 Conclusion**

Various techniques were used to understand and compare the crystallization and melting characteristics and the isothermal and non-isothermal crystallization kinetics of the PET and PET/clay nanocomposites (PCNs). DSC and DTA devices were used to carry out the investigation. The PCNs were obtained by melt compounding of the PET resin with 1 wt% Cloisite 30B. The multiple melting behavior of isothermally crystallized samples was evaluated by employing temperature modulated DSC (MDSC). It was shown that the first and second endotherms could be attributed to the melting of secondary and primary crystals, respectively. A significant amount of nuclei left during the first two endotherms undergoes reorganization and recrystallization in both the PET and PCNs, contributing to the presence of the third melting peak.

The Avrami analysis showed that, overall, isothermal crystallization of PET was faster in the PCNs than in the neat PET. However, the analysis based on the Lauritzen-Hoffman secondary nucleation theory suggests that the presence of clay leads to less perfect crystalline structures. Thus, the equilibrium melting point of the PCNs appears at higher temperature and the required work for chain folding in the presence of clay is somewhat higher than in the neat PET. POM micrographs also showed that smaller crystallites appear in the isothermally crystallized PCNs, in comparison with the neat PET.

The modified Avrami equation and the combined Avrami-Ozawa method were used to investigate the non-isothermal crystallization kinetics. The calculated effective activation energy

for the PCNs was higher than for the PET, which suggests smaller crystalline structure for the PCNs during non-isothermal crystallization, as confirmed qualitatively by POM results.

Both isothermal and non-isothermal kinetic studies show that nanoclay acts as a nucleating agent and yields a faster overall rate of crystallization. However, in the presence of clay, more work is required for chain folding and the activation energy for crystalline growth is higher. This suggests that smaller size and imperfect crystals are more prevalent in nanocomposites.

## A.5 Acknowledgments

The authors appreciate the generosity of DuPont Canada for supplying one of the PET resins. This project was jointly funded by NRC-NSERC-BDC.

## A.6 References

1. W. Perkins, *Polym. Bull.*, **19**, 397 (1988)
2. D.J. Sekelik, E.V. Stepanov, S. Nazarenko, D. Schiraldi, A. Hiltner, and E. Baer, *J. Polym. Sci. Pol. Phys.*, **37**, 847 (1999)
3. N. Qureshi, E.V. Stepanov, D. Schiraldi, A. Hiltner, E. Baer, *J. Polym. Sci. Pol. Phys.*, **38**, 1679 (2000)
4. E.L.V. Lewis, R.A. Duckett, I.M. Ward, J.P.A. Fairclough, and A.J. Ryan, *Polymer*, **44**, 1631 (2003)
5. Z. Ke, and B. Yongping, *Mater. Lett.*, **59**, 3348 (2005)
6. M. Frounchi, and A. Dourbash, *Macromol. Mater. Eng.*, **294**, 68 (2009)
7. R.B. Dupaix, and D. Krishnan, *J. Eng. Mater.-T. ASME*, **128**, 28 (2006)
8. Z.G. Wang, B.S. Hsiao, B.X. Fu, L. Liu, F. Yeh, B.B. Sauer., H. Chang, and J.M. Schultz,

Polymer, **41**, 1791 (2000)

9. S. Piccarolo, V. Brucato, and Z. Kiflie, *Polym. Eng. Sci.*, **40**, 1263 (2000)
10. S. Tan, A. Su, W. Li, and E. Zhou, *J. Polym. Sci. Pol. Phys.*, **38**, 53 (2000)
11. X.F. Lu., and J.N. Hay, *Polymer*, **42**, 9423 (2001)
12. R. Androsch, and B. Wunderlich, *Polymer*, **46**, 12556 (2005)
13. L. Li, R. Huang, L. Zhang, and S. Hong, *Polymer*, **42**, 2085 (2001)
14. T.L. Hanley, J.S. Forsythe, D. Sutton, G. Moad, R.P. Burford, and R.B. Knott, *Polym. Int.*, **55**, 1435 (2006)
15. J. Bian , S.R. Ye, and L.X. Feng, *J. Polym. Sci. Pol. Phys.*, **41**, 2135 (2003)
16. S.M. Hee, J.Y. Won, S.Y. Eui, C.K. Byoung, and S.I. Seung, *J. Appl. Polym. Sci.*, **80**, 2640 (2001)
17. F. Chaari, M. Chaouche, and J. Doucet, *Polymer*, **44**, 473 (2002)
18. D.W. Chae, and B.C. Kim, *J. Mater. Sci.*, **42**, 1238 (2007)
19. Y. Ke, C. Long, and Z. Qi, *J. Appl. Polym. Sci.*, **71**, 1139 (1999)
20. C. Saujanya, Y. Imai, and H. Tateyama, *Polym. Bull.*, **51**, 85 (2003)
21. Y. Wang, J. Gao, Y. Ma, and U.S. Agarwal, *Compos. Part B-Eng.*, **37**, 399 (2006)
22. H. Zheng, and J. Wu, *J. Appl. Polym. Sci.*, **103**, 2564 (2007)
23. T. Wu, and Y. Ke, *Thin Solid Films*, **515**, 5220 (2007)
24. T. Wan, L. Chen, Y.C. Chua, and X. Lu, *J. Appl. Polym. Sci.*, **94**, 1381 (2004)
25. C.F. Ou, M.T. Ho, and J.R Lin., *J. Polym. Res.*, **10**, 127 (2003)
26. G. Guan, C. Li, X. Yuan, Y. Xiao, X. Liu, and D. Zhang, *J. Polym. Sci. Pol. Phys.*, **46**, 2380 (2008)
27. J.W. Chung, S.B. Son, S.W. Chun, T.J. Kang, and S.Y. Kwak, *J. Polym. Sci. Pol. Phys.*, **46**, 989 (2008)

28. H. Ghasemi, P.J. Carreau, M.R. Kamal, and S.H. Tabatabaei, "Properties of PET nanocomposite films", Submitted to Polym. Eng. Sci. (2010)
29. X.Y. Tian, C.J. Ruan, P. Cui, W.T. Liu, J. Zheng, X. Zhang, X.Y. Yao, K. Zheng, and Y. Li, Chem. Eng. Commun., **194**, 205 (2007)
30. C. Ge, P. Ding, L. Shi, and J. Fu, J. Polym. Sci. Pol. Phys., **47**, 655 (2009)
31. Y. Wang, C. Shen, H. Li, and Q. Li, J. Appl. Polym. Sci., **91**, 308 (2004)
32. D. Cai, Y. Zhang, and Y. Chen, Iran. Polym. J., **16**, 851 (2007)
33. X. Zhu, B. Wang, S. Chen, C. Wang, Y. Zhang, and H. Wang, J. Macromol. Sci. B, **47**, 1117 (2008)
34. X. Chen, C. Li, W. Shao, Eur. Polym. J., **43**, 3177 (2007)
35. Y.P. Khanna, and W.P. Kuhn, J. Polym. Sci. Pol. Phys., **35**, 2219 (1997)
36. M. Reading, D. Elliott, V. L. Hill, J. Therm. Anal., **40**, 949 (1993)
37. Schawe J.E.K., Bergmann E., Winter W.; J. Therm. Anal.; (1998); **54**; 565-576
38. K.J. Jones, I. Kinshott, M. Reading, A.A. Lacey, C. Nikolopoulos, and H.M. Pollock, Thermochim. Acta, **304/305**, 187 (1997)
39. R.F.J. Medellin, P.J. Phillips, J.S. Lin, and R. Campos, J. Polym. Sci. Pol. Phys., **35**, 1757 (1997)
40. Z.G. Wang, B.S. Hsiao, B.B. Sauer, W.G. Kampert, Polymer, **40**, 4615 (1999)
41. Y. Kong, and J.N. Hay, Polymer, **44**, 623 (2003)
42. J. D. Hoffman, and J. J. Weeks, J. Chem. Phys., **37**, 1723 (1962)
43. P. Juhász, J. Varga, K. Belina, and H. Marand, J. Therm. Anal. Calorim., **69**, 561 (2002)
44. L. H. Sperling, Introduction to physical polymer science, John Wiley & Sons, (2006)
45. A. Mehta, U. Gaur, and B. Wunderlich, J. Polym. Sci. Pol. Phys., **16**, 289 (1978)
46. M. Avrami, J. Chem. Phys., **7**, 1103 (1939)
47. P. Supaphol, Thermochim. Acta, **370**, 37 (2001)

48. O. Verhoyen, F. Dupret, and R. Legras, *Polym. Eng. Sci.*, **38**, 1594 (1998)
49. T.M. Wu, S.F. Hsu, C.F. Chien, and J.Y. Wu, *Polym. Eng. Sci.*, **44**, 2288 (2004)
50. Z. Qingxin, Z. Zhihao, Z. Hongfang, and M. Zhishen, *J. Polym. Sci. Pol. Phys.*, **40**, 1784 (2002)
51. T. Jiang, M. Liu, P. Fu, Y. Wang, Y. Fang, Q. Zhao, *Polym. Eng. Sci.*, **49**, 1366 (2009)
52. A.Y. Malkin, V.P. Beghishev, I.A. Keapin, S.A. Bolgov, *Polym. Eng. Sci.*, **24**, 1396 (1984)
53. P. Supaphol, and J. E. Spruiell, *J. Macromol. Sci. B.*, **39**; 257 (2000)
54. J.W. Huang, C.C. Kang, and T.H. Chen, *J. Appl. Polym. Sci.*, **97**, 1051 (2005)
55. A. Asadinezhad, S. H. Jafari, H.A. Khonakdar, F. Bohme, R. Hassler, and L. Haussler, *J. Appl. Polym. Sci.*, **106**, 1964 (2007)
56. J.I. Lauritzen, and J.D. Hoffman, *J. Appl. Phys.*, **44**, 4340 (1973)
57. Hannay N.B. (Editor); "Treatise on solid state chemistry, Vol.3, Crystalline and Non-crystalline solids"; Plenum Press; Chap.7, (1976)
58. J.I. Lauritzen, *J. Appl. Phys.*, **44**, 4353 (1973)
59. L. Mandelkern, "Crystallization of Polymers", Cambridge University Press; Chap.9, (2004)
60. A. Jeziorny, *Polymer*, **19**, 1142 (1978)
61. T. Ozawa, *Polymer*, **12**, 150 (1971)
62. T. Liu, Z. Mo, S. Wang, and H. Zhang, *Polym. Eng. Sci.*, **37**, 568 (1997)
63. J.A. Augis, and J.E. Bennett, *Therm. Anal.*, **13**, 283 (1978)
64. H.E. Kissinger, *J. Res. Nat. Bur. Stand.*, **57**, 217 (1956)
65. R.L. Takhor, "Advances in Nucleation and Crystallization of Glasses"; American Chemical Society: Columbus (1971)
66. H.J. Friedman, *Polymer Science: Part C: Polymer Symposia*, **6**, 183 (1964-1965)
67. J.H. Flynn, and L.A. Wall, *J. Res. Nat. Bur. Stand.*, **70**, 487 (1966)
68. Y.P. Khanna, *Polym. Eng. Sci.*, **30**, 1615 (1990)

69. Z. Ruiyun, Z. Haifeng, L. Xiaolie, and M. Dezhu, *J. Appl. Polym. Sci.*, **51**; 51 (1994)
70. D.S. Achilias, G.Z. Papageorgiou, G.P. Karayannidis, *J. Polym. Sci. Pol. Phys.*, **42**, 3775 (2004)